Spectroscopy of displacements in a two-dimensional colloidal glass former

DISSERTATION

zu Erlangung des akademischen Grades des
Doktors der Naturwissenschaften an der

UNIVERSITÄT KONSTANZ
Mathematisch-Naturwissenschaftliche Sektion
Fachbereich Physik

vorgelegt von

CHRISTIAN LUDWIG KLIX

Tag der mündlichen Prüfung: 17.12.2014
1. Referent: Dr. Peter Keim
2. Referent: Prof. Dr. Matthias Fuchs

Konstanzer Online-Publikations-System (KOPS)
URL: http://nbn-resolving.de/urn:nbn:de:bsz:352-0-274460

Contents

Und ’ne gute Grundlage für Besserung ist Erkenntnis.
Ihr wisst ja, bisher war Gemecker oft nur Missverständnis!
- Daniel Ebel aka. Dendemann

1. Introduction

The introduction to this thesis is divided into three parts. First, the experimental background is illuminated. Second, the physical phenomena studied in the scope of this work are addressed. The third part combines both aspects to explain the structure of this thesis and give a short overview.

1.1. Colloidal (model) systems

'Colloidal' is a term derived from the ancient Greek words $\kappa\acute{o}\lambda\lambda\alpha$ (*kólla*) and $\epsilon\iota\delta o\varsigma$ (*eidos*), translating loosely as *glue* and *appearance*, respectively. It was introduced by the British physicist Thomas Graham in 1861 within the framework of his diffusion experiments to describe the turbidity of the samples he used [Gra61]. Besides the fact that 'colloidal' nowadays does not address macroscopic appearance any more, he was also not the first to experiment with what is called 'colloidal systems'. Well known, for example, are Michael Faradays efforts to understand the coagulation of gold particles in suspension after addition of the salt sodium chloride from 1857 [Far57]. It took almost 150 years, however, to develop a closed theory capable of explaining this phenomenon [Der41, Ver48], after Debye and Hückel proposed a theory on polyelectrolytes in 1923 [Deb23]. Research on these kind of systems is still done today [Hen89, Xia00, Cos10]. In a modern understanding, 'colloidal' describes small objects of any material or shape [Dho96]. These are usually suspended in a medium, such that a colloidal system consists of two components: the dispersed material and a continuous carrier. This definition is pretty loose such that a multitude of systems as emulsions (droplets in a fluid medium), aerosols (droplets or particles in a gaseous medium) or foams (gas in a fluid or solid medium) are considered as colloidal.

Common to all these systems is their stability. The constituents do not mix, but also do not phase separate on a macroscopic scale. The typical colloidal length scale is limited on the lower end by macromolecules at $\approx 10\,\mathrm{nm}$[1] and on the upper end by granular materials at $\approx 10\,\mu\mathrm{m}$. This lengthscale is termed 'mesoscopic', as it separates the microscopic from the macroscopic/granular world. Colloids are still small enough to be described with statistical methods, but often large enough to be resolved optically. An outstanding feature of systems in this realm is that their activation energies are of the order of a few k_BT, where $k_B = 1.34 \cdot 10^{-23}\,\mathrm{J/K}$ is the Boltzmann constant

---

[1] Per definition, colloids are no quantum objects, i.e. they must be large (and heavy) enough to exhibit a vanishing De Broglie wavelength.

and T the temperature. In other words, mesoscopic systems exhibit a rich variety of degrees of freedom at moderate temperatures. In this, they are comparable to atomic and molecular systems where activation energies can also be of the order of several electron volt. The significantly larger length scale, however, leads to a very weak response to external stress, making colloidal materials very soft [Gom03]. For that, they are often referred to as *soft matter*, which is a class of materials also embracing polymers or complex bio-materials.

Coming back to the temperature susceptibility of mesoscopic systems, it is the origin of one of the most intriguing phenomena of colloidal suspensions: Brownian motion. The botanist Robert Brown observed the random motion of pollen in water [Bro28], which was later attributed to the thermal motion of solvent molecules and their momentum transfer to mesoscopic particles upon collision [Ein05]. This behavior is unique to colloids. Larger particles experience an increased amount of collisions and therefore suffer less from statistical fluctuations in the distribution of the momentum transfer. Combined with the huge inertial mass this kind of activation is completely suppressed in granular materials.

Intriguingly, the inherited motion allows colloids to probe the full phase space and therefore explore many different configurations. They even might self-assemble into large structures. In particular, they can assume the same states as atomic or molecular systems, only on a larger lengthscale [Pus89, Pha02, Roy06]. Thus, these are often called 'macrofluids' or 'macrocrystals'. But in contrast to the atomic case, colloids can be easily accessed by relatively simple probing techniques as light scattering [Hul82] or even conventional light microscopy [Ell01], allowing the direct observation of a multitude of phenomena in real space. Because of their size, colloids are also slow enough to be tracked over time, enabling the acquisition of full phase space information. Thus, colloidal systems offer themselves as models to study phenomena usually found on a lengthscale of nanometers, which can hardly be addressed directly.

While the properties stated above are interesting from a physical point of view, mesoscopic systems are investigated for even more reasons. Although inconspicuous and not realized by many people, colloidal systems are very much part of everyday life. It starts with life itself, for the cardiovascular system contains billions of red and white blood cells, floating around in a mixture of mainly water and some proteins and minerals. It continues from other biological systems as mud (dirt particles suspended in water) or milk (fat droplets and protein clusters suspended in water) and other food to man-made substances like dispersion paint (e.g. acrylic resin in water), toothpaste (silicates in foaming agent) or cosmetic products (e.g. oil in water). Therefore, insight in phenomena of colloidal systems is not only sought by fundamental but also by industrial researchers. Tailoring materials with specific characteristics obviously offers huge economical potential, but is also of humanitarian value for it may provide new methods of medication and health care. Finally, tackling the manifold mechanisms governing this class of (soft) materials might benefit biology and chemistry as well.

1.2. Glass transition

Glasses have a long history. Not realized by many, glassy materials have accompanied mankind for more than 10^6 years! In the stone age, *obsidian*, a naturally occurring volcanic glass was commonly used as a cutting tool and because of its rarity extensively traded [Tho84]. The first man-made silicate glasses were found among other archeological artifacts in northern Africa and date back to the late bronze age around 1600 BC [Reh05]. The term *glass*, however, originated only later from the Germanic word *glesum*, meaning transparent, during the time of the late Roman empire [Dou72]. In the last century, the production processes for glassware have developed rapidly, nowadays allowing the casting of highly specialized glasses with specific tailored properties. Different material compositions and processing methods provide applications in optics (reaching from wavelength-tailored laboratory lenses over temperature-stable mirror carriers for astronomical telescopes to aberration-minimizing photography objectives), in electronics (providing insulation in microscopic solid state devices, circuits or semiconductors), and even in sports, where the incorporation of 'liquid metal' (i.e. a metallic glass) is supposed to improve the performance (elasticity) of tennis rackets, skis or baseball bats. Yet, although glasses see such broad use and may be exploited in many different ways, the basic *physics* behind the glassy state are not yet fully understood.

The types of glass described in the last paragraph are solid materials which exhibit the disordered structure of a liquid, commonly called *structural glasses*[2]. With words from C. A. Angell [Ang95]: "*Glass, in the popular and basically correct conception, is a liquid that has lost its ability to flow.*"[3] Glasses originate from supercooled liquids which relax sufficiently slow to equilibrium such that they get trapped in their amorphous state before crystallization can generate an ordered assembly [Ang00b, Tan12b]. 'Sufficiently' here means *slow regarding the cooling rate.* Indeed, almost *every* material may freeze in an amorphous state, although absurdly high cooling rates might be necessary[4]. For the archetypical glass, vitreous silica, cooling rates of 0.1 K/s are sufficient. For metallic alloys, already 10^6 K/s are required, while for pure metals, even rates of the order of 10^{12} K/s may not be enough [Joh96, Joh99]. Because this phenomenon highlights the connection between (amorphous) structure and dynamics, vitrification is often called a *kinetic* mechanism, expressing that the constituents are

---

[2] Besides structural glasses, there also exist other types like spin glasses or orientational glasses. In those, the persistent disorder is present in spin orientation and director field, respectively.

[3] A more universal definition would be that one or more generalized coordinates have become *non-ergodic*, i.e. can not explore the whole parameter space any more [Ang00a]. This extends the very brief overview on glassy systems and their application given in the last paragraph towards (synthetic) polymeric materials, which also are at least partially amorphous, yet solid.

[4] One exception are two-dimensional colloidal monolayers with vanishing polydispersity. As discussed in section 2.1.1, there it is possible to realize cooling rates much larger than in atomic systems (relative to internal dynamics), but still only a polycrystalline state is found [Dil08, Dil11, Dil12].

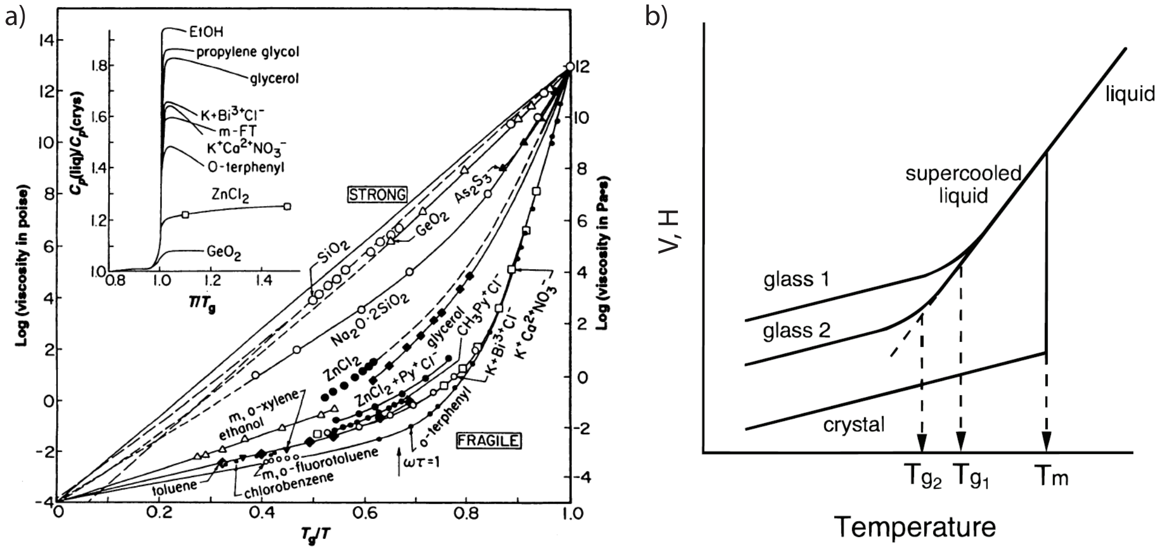

Figure 1.1.: **The glass transition.**
a) Plotted in Arrhenius form, the viscosity shows a dramatic increase over some orders of magnitude in the vicinity of the glass transition temperature T_G. It becomes evident that there exist two types of glass former: strong and fragile, depending on the temperature-dependence of the activation energy. The inset shows the corresponding heat capacities, which jump at T_G more or less significantly.
b) In the supercooled state, volume V and enthalpy H may be linearly extrapolated from the liquid. Upon the glass transition, an abrupt but continuous deviation occurs.
Taken from [Ang95] and [Edi96], with slight modifications.

kinetically not able to relax to the systems crystalline ground state [Tam33].

Usually, glasses are distinguished from the liquid state only by their extraordinary high viscosity [Deb01], resulting from a severe slow down of (microscopic) dynamics. The most well-known way to visualize this phenomenon is to plot the logarithmic viscosity versus the glass transition temperature T_G over temperature T, as done in figure 1.1. Already in this depiction it becomes apparent that glasses do not form universally. Here, they may be sorted roughly in the two categories of *strong* or *fragile* glass formers, depending on whether they show linearity or even stronger behavior in a logarithmic plot versus inverse temperature (called Arrhenius or super-Arrhenius like behavior, respectively). As a rule of thumb, inorganic systems tend to behave as the former, while organic ones follow the latter form. This is attributed to the corresponding energy landscape of (chemical) bond forming. For strong glass formers with constant 'activation energy' this is rather homogeneous, whereas for fragile glass

formers with a strong increase in 'activation energy', it is rather heterogeneous, i.e. a large number of molecules has to rearrange to allow the system to fall in a lower energy state [Deb01].
A major drawback of this representation, however, is the arbitrary definition of the 'glass transition viscosity' $\nu_G = 10^{12}\,\mathrm{Pa\,s}$, already indicating that the glass transition does not occur at a well defined temperature. Other quantities often studied are of thermodynamic nature [Gib58, Ada65], as heat capacity (compare inset of figure 1.1), enthalpy or entropy. In figure 1.1.b) it is sketched how volume V and enthalpy H behave discontinuously at the melting temperature T_m upon crystallization in a first order phase transition. Without seeds, a very pure liquid may be supercooled into a metastable state, for which V and H are extrapolations from the liquid. They level continuously upon reaching the glass transition temperature T_G, giving again evidence that the glass transition is no real thermodynamic transition [Edi96]. Here, T_G is defined as the intersection between the extrapolation from the glassy and supercooled state, which might be cooling-rate dependent.

As outlined, the phenomenon *glass transition* is well studied. It is the origin for this behavior, however, which is still subject to debate even after many years of intensive investigations. Accordingly, theories on that matter are manifold. Mode coupling theory (MCT) [Göt09] or free-volume theory [Coh59] study density-density correlations and transport properties, attributing the dynamical arrest to slow relaxation. Adam-Gibbs theory [Ada65] deals with cooperative motion, resulting in increasing dynamical correlation, whereas kinetically constrained models [Hed09] disengage from purely configurational space but rather search for spatio-temporal mechanisms responsible for the glass transition, trying to tie critical phenomena into the picture. Geometrical frustration and energy landscape problems are studied within random first order transition theory (RFOT) [Kob97], which is in close connection to bond-order approaches [Tan12b] which understand the glass transition as a modified form of crystallization.

In this work, colloidal systems and glassy behavior are linked. This was pioneered by Pusey and van Megen, who demonstrated that colloidal hard spheres could freeze in a disordered fashion [Pus87]. The easily accessible nature of colloidal systems allows to study phenomena accompanying the glass transition in great detail (a small selection of the nearly infinite number of publications is [Bar94, Che02, Ram05, Ebe08b, Che10]). In the past, it has been shown that glassy systems in two dimensions exhibit the same phenomena as bulk systems [Per99, Kön05, Bay07]. This is remarkable, because the crystallization scenario shows some significant discrepancies like a hexatic phase in 2D [Hal78] or an absence of long range translational order [Mer66, Mer68]. The universality of the glass transition in this sense offers some major opportunities for experiments and simulation. By excluding the third dimension, data handling and evaluation becomes more simple, and sometimes results are easier to interpret. Against this background, complicated problems are more likely to be solved.

1.3. Structure of this thesis

In this thesis, a special case of colloidal glass formers is realized. By dispersing two different sized species of superparamagnetic polystyrene beads in a suspended water droplet and letting them sediment down to the water-air interface, a nearly ideal two-dimensional system without any lateral substrate interaction is realized. With a typical video microscopy approach, real time/space data is recorded such that the full phase space information is available. The interesting feature of this experiment is the instantaneously tunable interaction between colloids via an external magnetic field, effectively providing a precise temperature control. This allows to cool the system from a liquid into the glassy state. Additionally, the pair potential between all particles is known precisely, providing the possibility of computing thermodynamic properties. With a sophisticated experimental setup, the system may be stabilized for extended amounts of time, allowing to probe the necessary long time behavior in glassy systems.

In the second chapter, the experiment is introduced and detailed information is given about the setup. The interaction of all control mechanisms used to stabilize the sample, allowing an eventual equilibration, is discussed. Because the main features of the experiment are well known and also can be found in [Ebe09a], emphasis is put on modifications and novel approaches developed in this thesis.

In the third chapter, the elastic properties of the provided colloidal glass are investigated. By studying the displacement field relative to equilibrium particle positions, the dispersion relations of acoustic-like phonons may be extracted. Because those excitations probe the elastic response of their propagation medium, the latter may be readily derived from the dispersion bands, illuminating the behavior of the shear modulus at the glass transition. A finite time and size analysis complete the physical image obtained in this chapter.

The fourth chapter further engages in the vibrational behavior of the glassy state. By choosing a different, more abstract approach (principal component analysis), not only some density of states, but also real space images of the corresponding modes may be obtained. These results are used to classify the physical assumptions made in chapter two. Likewise, the dispersion results are used to cross check the density of states.

In the fifth chapter, the glass transition is studied from the viewpoint of critical phenomena. For some initial information on the system, established techniques are utilized. In search of a growing correlation length, a novel technique to investigate the phenomena of dynamical heterogeneity is introduced.

The sixth chapter illuminates the influence of solid substrates on vibrational properties found in this work, before this thesis is finally concluded by a recapitulation of the results.

2. Methods

This chapter covers all experimental details. Information is given on the colloidal system and the underlying physics and the efforts to control and shape this system to access the desired properties.

2.1. Colloidal system

All colloidal particles used in this work were polystyrene beads. To provide a system which exhibits slow dynamics yet structural disorder under certain circumstances, two different species of particles had to be deployed. They differ in size; type B ('big') particles have a diameter of $4.5\,\mu$m while type S ('small') particles only extend to $2.8\,\mu$m. Their most noticeable feature is the magnetic trait. Transmission electron microscope micrographs (TEM) reveal pores in the cross-linked polystyrene, large enough to allow the diffusive injection of small iron oxide nanoparticles. Extending only as far as a couple of nanometers, the maghemite nanoparticles (Fe_2O_3) contain a single domain with a magnetic moment. This is susceptible to thermal (rotational) diffusion because of its small size. Thus, the resulting net magnetization of a bead is zero because of the random (isotropic) distribution of moments. In an external magnetic field, however, these moments can be aligned and therefore add up to a macroscopic moment oriented along the field axis. Because the particles show no remanence but their susceptibility is comparable to that of ferromagnetic materials, they are called 'superparamagnetic'.
Although the volume of type B particles is only four times larger than that of the small particles, their susceptibility ($\chi_B \approx 6.22 \cdot 10^{-11}\,\mathrm{Am^2/T}$ per bead) is an order of magnitude larger than that of type S particles ($\chi_S \approx 6.6 \cdot 10^{-12}\,\mathrm{Am^2/T}$ per bead).
The size polydispersity of type B particles is negligible since of the order of $1\,\%$. Although the polydispersity of type S particles is much higher (no manufacturer information available, but estimated by scanning electron (SEM) micrographs), it does not play a role in the physical behaviour of the system as the particle interactions are governed by the magnetic properties of the beads. This is further ensured by placing surfactants onto the bead surface, stabilizing them sterically, i.e. preventing possible agglomeration caused by Van der Waals forces.
The particles mass densities are $1.5\,\mathrm{g/cm^3}$ and $1.3\,\mathrm{g/cm^3}$ for B and S type, respectively. They differ because of the uneven iron oxide doping. Yet, both are a little heavier than pure water, causing them to sediment once put in solution.

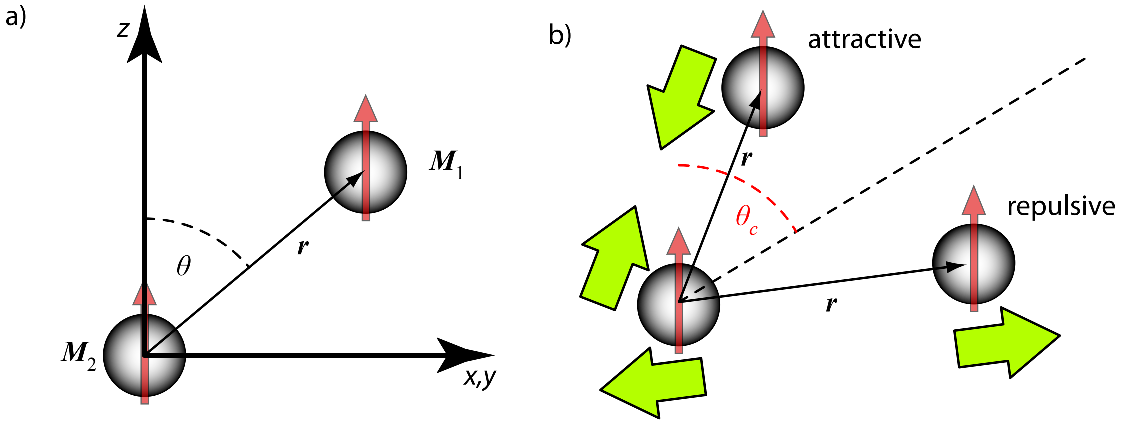

Figure 2.1.: **Dipole interaction.**
a) Schematics of two point dipoles with magnetic moments $\mathbf{M}$ (red arrows), both oriented along the z-axis. They are connected by the vector $\mathbf{r}$.
b) Depending on the angle θ, the interaction becomes attractive or repulsive (green arrows). The critical angle is $\theta_c \approx 54.7°$.

2.1.1. Magnetic interaction

To describe the state of the system, it is instructive to declare a control parameter. Depending on the mechanism driving a system through its possible states, the usual thermodynamic variables temperature, pressure or volume/density come to mind. At first sight, it seems obvious to choose temperature - from an everyday perspective, this is what controls the melting of solids or the evaporation of fluids, after all. However, the dawn of colloidal experiments has established the density as the main control parameter, as it drives an entropic phase transition in hard sphere systems from fluid to crystal if the volume fraction is pushed beyond $\approx 49\,\%$ [Han06][1].

Choosing the right control parameter depends, however, very much on the conception of the experiment, as well on its purpose, i.e. which questions it asks and how these can be addressed. For this reason, in the experiments of this work, a control parameter Γ is introduced, which is universal in a sense that it couples all variables which affect the state of the system (such as temperature, magnetic field and density).

The starting point for a system containing magnetic components is the magnetic energy. In this case, the interaction energy between two single particles represented by magnetic point dipoles $\mathbf{M}_1$ and $\mathbf{M}_2$ reads

$$E_{\text{magn}} = -\frac{\mu_0}{4\pi}\frac{3(\mathbf{r}\cdot\mathbf{M}_1)(\mathbf{r}\cdot\mathbf{M}_2) - r^2(\mathbf{M}_1\cdot\mathbf{M}_2)}{r^5}\,,$$

---

[1] The original paper by Pusey and van Megen reports a critical volume fraction of $\approx 40\,\%$, probably due to residual long-range interactions [Pus86].

where $\mathbf{r}$ is the distance between the dipoles and μ_0 the vacuum permeability. For parallel dipoles, this simplifies to

$$E_{\mathrm{magn}} = \frac{\mu_0 M_1 M_2}{4\pi} \frac{(1 - 3\cos^2\theta)}{r^3}\,, \tag{2.1}$$

where θ denotes the angle between the dipole axis and the connection vector $\mathbf{r}$ (see figure 2.1). It is important to note that here energy is only expended to align the beads' inherent magnetic moments. Former works included a factor 1/2 attributed to simulations, in which the induction of magnetic moments costs additional energy [Kei05, Ebe08a].

Depending on θ, the interaction might be attractive as well as repulsive. The two regimes are separated by the critical angle $\theta_c \approx 57.4°$, where E_{magn} vanishes. For the 2D case, where all particles are confined to a plane perpendicular to the dipole axis, the cosine becomes zero. Thus, the magnetic energy is only dependent on the magnetic moments and the distance between particles. The former is induced by an external magnetic field to $\mathbf{M}_i = \chi_i \mathbf{H}$, where χ_i is the susceptibility of particle i. Assuming that all particles within one species have identical properties, equation (2.1) can be rewritten with an effective susceptibility $M = \xi \cdot \chi_S + (1 - \xi) \cdot \xi_B$, where the species' susceptibilities are weighted with the relative concentration of small particles $\xi = N_S/(N_B + N_S)$.

The second variable in equation (2.1), the dipole distance r, is determined by the density n of the beads in the plane. As all particles try to maximise the distances to their adjacent counterparts, this will give rise to a well defined mean interparticle distance a_0 which is typical for the respective (area) density. But since in a disordered state there is no underlying symmetry (lattice), it is unclear how a_0 scales with n. Thus, the easiest way to derive a characteristic length from an area density is to take a square root of its inverse, $a_0 = \sqrt{1/n}$[2].

With these prerequisites, the control parameter may be defined by comparing magnetic energy with thermal energy E_{therm},

$$\begin{aligned} \Gamma &:= \gamma \frac{E_{\mathrm{magn}}}{k_B T} = \frac{\mu_0}{4\pi} \cdot \frac{H^2 \cdot (\pi \cdot n)^{3/2}}{k_B T} \cdot (\xi \cdot \chi_S + (1 - \xi) \cdot \chi_B)^2 \\ &\propto \frac{1}{T_{\mathrm{sys}}}\,, \end{aligned} \tag{2.2}$$

where γ is a constant factor aligning Γ with the definition in older works [Ebe08a].

For large magnetic fields H, the interaction strength between particles becomes large enough to influence the dynamical as well as the structural behaviour of the system. H may be changed instantaneously (compared to the particles' inherent Brownian time) and homogeneously by external means with high precision across the whole sample, while density and temperature are kept fixed during the experiment. In this sense,

---

[2] This is also in accordance with the predicted square lattice of a 50 : 50 binary mixture [For08].

Γ can be interpreted as an inverse temperature. A large control parameter achieved by a strong magnetic field corresponds to low temperatures where the system usually solidifies.

2.2. Experimental setup

2.2.1. Concept of a two dimensional colloidal experiment

To tackle the physics of two dimensional colloidal systems, certain experimental prerequisites need to be met. First of all, a flat surface to confine particles on is required. Second, this surface should not interact with the particles in any other way than a hard wall. Also, a certain chemical stability is needed. As most probing methods are optical, transparency in the visible spectrum is also necessary.

For that, most experimentalists fall back on simple solid substrates like plain glass cover slides [Mur90], polymer films [Bub98] or cleaved materials like mica [Nag93], where gravity pins particles down. However, since the diffusion coefficient of spheres is reduced in the vicinity of a solid wall [Bre61, Gol67], measurements on solid substrates always alter the dynamics of the system to some extend. Pinning of particles can also be an issue, especially for the study of phase transitions [Deu13b]. To avoid these issues, attempts have been undertaken to create colloidal monolayers on top of a fluid interface in the pioneering work of Pieranski [Pie80]. By confining the particles with surface tension, there is virtually no in-plane interaction with any solid substrate. Taking this a step further, it is also possible to trap the particles *inside* the water at the water-air interface by creating a droplet in some kind of orifice [Ono85]. This method has the advantage to prevent electrostatic dipolar interactions between particles which develop if symmetry breaking leads to an inhomogeneous charge distribution, mediated by the contact of the spheres to two different media, air and water [Hur85, Arm89]. If immersed in the fluid, the surface tension will prevent any contact to the air.

Coming close to *ideal* two dimensions, the pending water droplet geometry provides stability only on the expense of intense experimental invest. Inherently metastable, the system requires active regulation. Because of their mesoscopic length scale the particles are extremely susceptible to downhill-slope forces generated by the slightest interface deformations which inevitably kick in after some minutes due to unavoidable evaporation of the liquid. Further, heavy vibrations, concussions and inclinations due to thermal deformations can bring about a droplets doom. Therefore, much effort has been put into the design of a well-suited experimental setup for more than a decade. Evolving from the simple idea of using the water-air interface of a pending water droplet to confine superparamagnetic particles with tunable interactions to two dimensions [Zah97], the experiment has become more and more complex. Not only by adding (mechanical) auxiliary components like optical tweezers, motorized sample

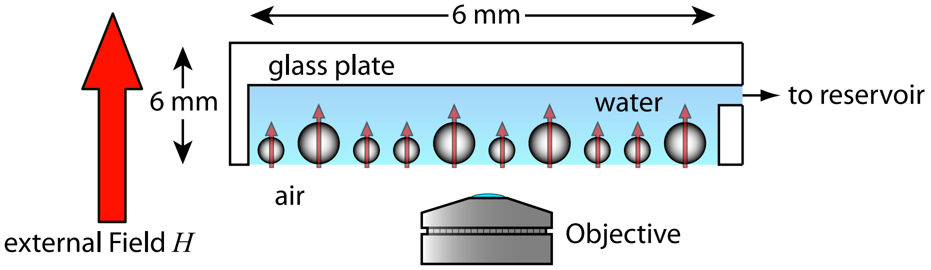

Figure 2.2.: **Sketch of the sample cell (not to scale).**
Superparamagnetic particles sediment down to a flat water-air interface. An external magnetic field H induces magnetic moments (small red arrows), therefore controlling the (dipolar) particle interaction.

stages or high field or in-plane coils to address new physics but also by integrating enhanced software support. A fairly recent description of the setup is given in [Ebe09a], although the evolution has continued up to today.

2.2.2. Realization of a two dimensional colloidal experiment

The setup's basic geometry is sketched in figure 2.2. A small amount of diluted colloidal suspension is inserted into the orifice of a notch on the bottom of a glass plate. The suspension forms a droplet, its volume accessible by a tiny channel connected to a water reservoir. The diameter of the notch is 6 mm, its height 1 mm. Sedimenting particles are confined to the water-air interface by surface tension and gravity, but do not penetrate the surface. Residual charges on the particles play no role as the ion concentration in the water is high enough to screen any electrostatic interaction on the relevant length scales. Using polystyrene spheres with iron oxide doping, magnetic moments can be induced by the application of an external magnetic field H perpendicular to the water-air interface. This provides the means to control the dipolar particle interaction *in situ*. The strength of interactions is expressed by a dimensionless control parameter Γ, effectively acting as an inverse temperature (see section 2.1.1). By using two particle species crystallization is suppressed. Instead, an amorphous solid state is induced upon cooling. Particle positions are recorded by a 8-bit gray scale CCD video camera coupled to a microscope objective, providing full phase space information on all relevant time- and length scales.
In figure 2.3, the external components of the setup are sketched. In the following, detail is given to each part separately.

1. **Sample cell.** The sample cell, measuring $20 \times 20\,\mathrm{mm}^2$, is a high-precision custom fabrication by *Hellma Analytics*. To provide a well defined droplet edge, the cell surface is chemically treated prior to mounting. After a washing procedure in

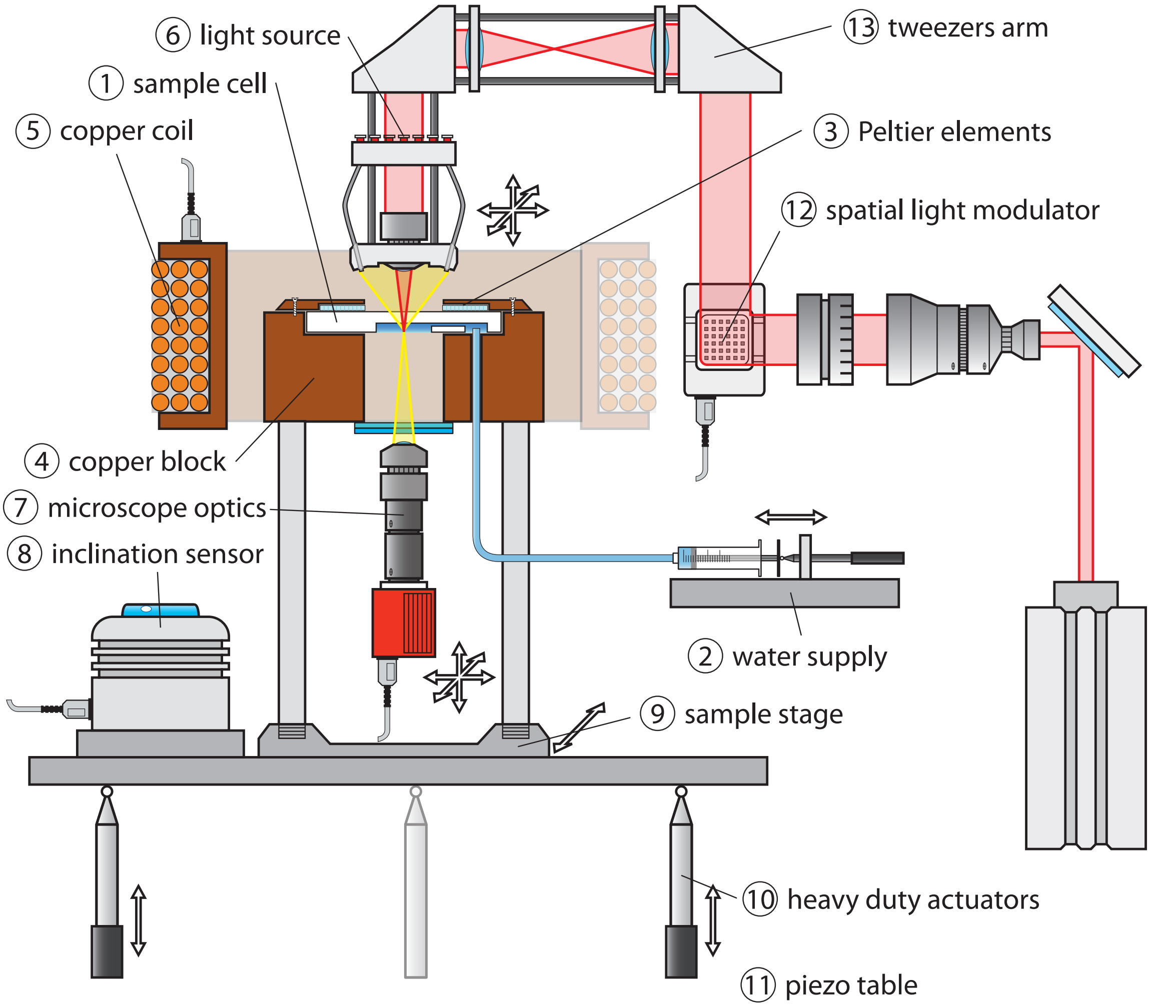

Figure 2.3.: **Sketch of the setup (not to scale).**
This sketch shows all external pieces of the experimental setup. Computer controlled components are indicated by the schematic USB plug. Computer controlled micromotors are indicated by arrows, also denoting the respective degree of freedom.

acetone and ethanol under ultrasonic conditions for 5 minutes each, the cell is immersed in a piranha bath (a 50 : 50 mixture of hydrogen peroxide and sulfuric acid) for 10 minutes, rendering all of the surface hydrophilic. Subsequently, a thin layer of silane (*Amersham* PlusOne Repel-Silane ES) is deposited on the flat glass surface surrounding the orifices of sample volume and reservoir, causing a strong wetting contrast and therefore preventing the droplet to escape the notch. Excess silane is washed away afterwards by flushing the cell with toluene for another 5 minutes.

2. **Water supply.** To achieve a completely flat water-air interface, the droplets volume needs to be accurately controlled. This kind of sensitive control is exerted by sticking the nozzle of a Teflon hose into the water reservoir, coupling the droplet effectively to a micro actuator (*Physik Instrumente*, DC Mike 230.25, step increment 50 nm, travel range 25 mm)[3] driven glass syringe (*Hamilton* GASTIGHT 1001, 1 ml volume, sub-minor graduations of 0.01 ml, Teflon piston).

3. **Peltier elements.** In order to control flow fields inside the droplet, four peltier elements (*QuickCool* QC-32-0.6-1.2, heat power 1.2 W at 1.2 A, maximum temperature difference 71 K) are embedded diagonally in the upper cell mount. With direct heat contact to the cell, temperature gradients along the water-air interface can be introduced. The resulting convection currents can be used to stir the sample gently in order to facilitate homogenous density distribution and mixing ratios, as well as to counteract occurring drift in the range of a few $\mu m/s$.

4. **Copper block.** The sample cell is mounted on an approx. $65 \times 65 \times 15\,\text{mm}^3$ (length x depth x height) copper block with a centered hole to allow optical access. Copper is used due to its large thermal conductance, suppressing undesired temperature gradients around the sample as the droplet is very susceptible to convective flows. The centered hole (diameter 10 mm) is sealed to create a laboratory-independent atmosphere. Once saturated with water vapor, the evaporation rate of the droplet decreases significantly. To seal the top hole, heat-conductive paste is squished between cell and copper. This also provides thermal connection of glass and copper. The bottom hole is sealed with an anti fogging sheet (*Pinlock*) glued to a microscope cover slip (diameter 12 mm) with transparent *Norland* optical adhesive 81. The anti fogging sheet is cut out from a motorcycle helmet visor, preventing condensation of water vapor on the optical access.

5. **Copper coil.** The copper block is enclosed by a custom made copper coil, with its symmetrical axis perpendicular to the water-air interface. The custom built power supply is controlled by a computer. Construction planning of the

---

[3] All other actuators used in the setup are of this type if not stated otherwise.

power supply emphasized a constant, high precision current mode because the interaction parameter Γ (see chapter 2.1.1) depends critically on the magnetic field strength (up to a precision of 0.001 mT). Constant voltage mode is not an option because inherent electric heating alters the electric resistance of the coil, leading in turn to a non-linear current increase. The coil was gauged to deliver a field of strength $H = 3.36\,\mathrm{mT}$ per Ampere. The actual current during an experimental run is recorded by a computer connected to an ampere meter (*Keithley Instruments* Integra 2700 Multimeter).

6. **Light source.** Attached to a laterally adjustable arm-like construction, a copper block houses 24 red LEDs (*Thorlabs* epoxy encased LED, 635 nm @ 4 mW), coupled to light guides pointing at the water-air interface at an angle of approx. 40°. The microscope objective below collects no direct light. The imaging is rather done in a kind of dark field microscopy, where the advantage of the light guides geometric alignment lies in the homogeneous intensity distribution all over the sample[4]. The intensity can again be controlled via a computer. The LED array is installed above the sample to avoid the ascending heat flow especially at high powers. Nevertheless, the light guides ensure sufficient intensity for microscopy applications.

7. **Microscope optics.** The colloidal system is observed with a CCD camera (*Allied Vision Technologies*, Marlin 145B, 10 fps @ 8 bit, FireWire) coupled to a microscope objective (*Zeiss* A-Plan, 5×magnification @ NA 0.12, working distance 9.9 mm). For image projection onto the CCD chip, objective and camera are connected by a lens tube (*Stemmer Imaging*, 1×magnification C-mount microscope tube). A small slit in the tube allows the insertion of an IR filter (*Optics Balzers* Calflex X, transmission T @ 1064 nm: $\leq 1\,\%$). The camera is fixed on a mechanical mount attached to three micro actuators, allowing for computer controlled positioning. The camera constantly records images which are analyzed on the fly, providing information on the number of particles in the field of view and their respective size in real time. Due to this computational effort, the actual frame rate is reduced to approx. 2.5 frames per second. For measurements, where these information are written to a hard drive, the frame rate drops down further to approx. 1.5 frames per second.

8. **Inclination sensor.** Mounted on the setups baseplate, a sensor (*Leica Geosystems AG* Nivel20) measures changes in inclination with a precision of up to $1\,\mu$rad. Because the colloidal system reacts very sensitive to tilting of the water-air interface, the sensor data is utilized in a feedback loop to actively counter

---

[4] As the vertical walls of the sample cell's notch also scatter some of the incident light, a faint dark ring is observed in the vicinity of the sample's edges. This makes it difficult to reliably distinguish between big and small particles in this region. Measurements however, always conducted in the middle of the notch, are not affected.

slow inclination changes/low frequency oscillations, as occurring due to thermal expansion or weight distribution changes of the setups components (motor displacement).

9. **Sample stage.** The copper block is mounted onto a computer-controlled translation stage (*Physik Instrumente* M-511.DG, maximum load 1000 N). It allows the movement of the sample relative to the field of view and, more importantly, relative to the optical tweezers. Computer control permits various movement patterns, most prominently continuous sine amplitudes.

10. **Heavy duty actuators.** The setup's base plate rests on a tripod, consisting of a rigid pin and two heavy duty actuators (*Physik Instrumente* DC Mike 235.5DG, step increment 100 nm, travel range 50 mm, maximum load 120 N). This construction allows subtle inclination changes of the whole setup in both lateral directions, keeping the water-air interface absolutely even.

11. **Piezo table.** Not shown in figure 2.3, the heavy duty actuators rest on the surface of a piezo table (*HWL Scientific* TS150). It damps out high-frequency vibrations in the range of 0.7 Hz to 1 kHz. Above 10 Hz, the transmissibility drops below −40 dB. Excitations like foot patter, building vibrations or impact shocks of falling objects are almost completely damped out. The piezo table itself is set up on a heavy optical table (*Newport* PL-2000) with deactivated air damping. This provides a massive, solid stand, yet does not interfere with the active damping system.

12. **Spatial light modulator.** By manipulating the phase of an incident homogeneous wave front in a spatially resolved manner, it is possible to shape a light beam into virtually any pattern. This is usually realized by adding diffractive optics into the path of light [Duf98]. A versatile approach are spatial light modulators (SLM), basically nothing more than small LCD displays, where each pixel is able to delay the phase of reflected light [Cur02]. In the setup, an 8-bit device is used (*Holoeye* Pluto, 1920×1080 pixels on $15.3 \times 8.6\,\mathrm{mm}^2$ optimized for near infrared (NIR) reflection). It is accessible via an *HDMI* interface.
    To exploit the full resolution and minimize image defects, the incident laser beam (*Spectra Physics* Millenia IR, max. 6 W @ 1064 nm) is guided through a beam expander and the polarisation subsequently rotated by a $\lambda/2$ wave plate to fall parallel onto the long axis of the SLM display.

13. **Tweezers arm.** The construction houses an objective (*Leica* HC PL Fluotar, 100×magnification @ NA 0.75, working distance 4.7 mm) to project the Fourier transformed image of the SLM onto the focal plane. Therefore, two lenses convey the manipulated wave front from the SLM to the back focal plane of the objective. It is adjustable in all three lateral dimensions by micrometer stages to allow precise positioning of the image in the field of view of the camera.

Solid substrate

Because of the droplets metastability, some experiments have also been conducted in closed, custom build sample cells on a solid substrate, promising enhanced and faster equilibration and less experimental effort. These were mounted in a setup featuring the same basic geometry as described above. However, it was not equipped with a motorized sample stage and no optical tweezer. Also, the Peltier elements for thermoelectric temperature control were not featured. The sample was illuminated by a single point light source (blue LED), enabling direct bright field microscopy. The coil to generate the magnetic field had a significantly higher amount of windings accompanied by a much smaller inner diameter, pushing the possible magnetic field up to approx. 100 mT. Such a high field strength is necessary to induce glassy dynamics in very asymmetric binary mixtures, featuring a large number of small particles ($\xi \geq 0.7$). To allow operation at high currents yet prevent any heat flow to the sample cell, the coil is constructed for water cooling.

As known from total internal reflection microscopy (TIRM) studies [Pri87, Pri90b, Pri90a], polystyrene spheres in aqueous solutions levitate above any glass surface. In this case, the colloidal particles are confined by gravity and electrostatic repulsion. However, as the elevation height only extends to some tenth of nanometers, particles are occasionally bound (pinned) due to Van der Waals forces. This effect might be reduced by chemical treatment of the surface. For details, see section 2.3.2.

2.2.3. Digital image analysis

Since the seminal work of Crocker and Grier [Cro96] in 1996, digital image analysis has become an essential part of experiments on colloidal suspensions. The images not only directly visualize phenomena in these systems, but their analysis also provides the full phase space information of all its constituents. This allows for the computation of any desired quantity.

While in common experiments images are usually written to the hard drive during the experimental run and analyzed afterwards, the setup described in section 2.2.2 makes it necessary to process images *in situ*. The reason is that the setup control mechanisms (section 2.2.4) require parameters like particle number, particle size and particle density as input. Unfortunately, common image processing proves to be computationally too intensive, significantly reducing the achievable frame rate. To provide a satisfactory frame rate nevertheless, a simplification of the analysis routine as deployed in [Cro96] is implemented. In a first step, the 8 bit gray scale image is converted into a monochrome image with a certain threshold, which excludes low-intensity noise, i.e. image elements with an intensity value above the threshold are set to one, while all other elements are set to zero. The threshold is chosen low enough such that pixels belonging to particles lie well above.

For further noise reduction, the image is *eroded*. By setting image elements to zero if

one of their direct four neighboring elements is zero, the surface of any bright object is reduced. In other words, a structure mask corresponding to a five pixel cross is applied. Single elements or lines vanish that way. All nonzero elements now are part of ‘real’ features of the image.
Particle size is restored in the next step by *dilating* the image. This procedure is setting all neighboring elements of pixels with value one to one as well. Application of these morphological base operations reliably yields low noise images. Connected valid elements are then merged to consecutively labeled ‘blobs’ (Binary Large OBjects). Each blob represents one particle and usually contains between 40 to 110 elements, depending on the particle size, magnification and CCD sensor resolution. By calculating the center of mass for every blob, particle coordinates can be extracted with a precision better than the optical resolution given by the illumination wavelength.
With this method, up to ≈ 4000 particles in the field of view can be reliably identified with a frame rate of approximately two frames per second in the binary system. Higher particle densities may yield inaccurate results as the overall brightness increases by mutual particle illumination. As a consequence, large and small particles can no longer (reliably) be distinguished. The frame rate lies well below intrinsic dynamical time scales of the studied system and is therefore sufficient.

Because the original tracking code from Crocker was written for rather short measurements of a couple of thousand frames, some work had to be done in order to adapt the algorithms to larger amounts of data. In 1996, the approach was to load all data into the memory and construct a network of spatial-temporal bonds, establishing possible connections between particles in time in order to assign them to a single trajectory (track). With skyrocketing computer power (multicore CPUs, several GB of memory), this method is still feasible for data sets consisting of $50 \cdot 10^3$ frames, where each contains positional information of ≈ 2000 particles. Processing this affords approx. 10 GB of memory, and the computation becomes somewhat slow. For the measurements done in this thesis, in which the raw data of each run alone takes up 16 GB of disk space ($380 \cdot 10^3$ frames), a different solution was necessary. Here, the data was split into equal chunks of 1000 frames. As a consequence, tracking was done not longer simultaneously but rather in a step-by-step fashion. Data from the preceding and successive chunks would be added to create some ‘overlap’ and secure continuous trajectories, thus allowing extrapolation of temporarily lost particles beyond the chunk boundaries.

Size discrimination in binary mixtures

While this method offered reliable tracks on short to intermediate timescales, certain factors could corrupt data for extremely long measurement runs as performed in this thesis. Long term intensity fluctuations as well as fluctuating densities would shroud the real particle size. The latter is due to the influence of mutual illumination which is enhanced by high density. While the intensity cutoff in the tracking algorithm can be chosen low enough to ensure continuous particle detection, every calculation of quantities relying on size information suffers severely. For that reason, a solution of this problem is offered by recording this information along with positional data, allowing a post-measure correction. This is illustrated in figure 2.4. Graph a) shows roughly 10 % of the field of view and depicts particle coordinates from the first frame of a measurement run. Size is encoded in red and orange shells for big and small particles, respectively. The particle size determined by averaging the respective information for the whole run is depicted as a light and dark green core for big and small particles, respectively. Especially on the edge, a couple of cases of an initial 'false' assignment can be found - in both directions, i.e. a particle initially perceived as big is later identified as small and vice versa.

Figure 2.4.b) shows the size fluctuations of representative big and small particles over time, where the top data is taken from a droplet measurement and the bottom data from a substrate measurement. Right of the graph, σ indicates the respective variance. It is smaller in the substrate case because of a smaller magnification and the resulting loss of optical resolution. For those particular examples, size fluctuations are small enough to easily distinguish between big and small. This becomes also apparent in the particle size distribution shown in figure 2.4.c), which was averaged over a measurement run ($50 \cdot 10^3$ frames, $120 \cdot 10^3$ seconds). The large number of statistics smooths the histogram and enables a clean distinction between both species, as indicated by the solid red vertical line. The variance of size fluctuations of a representative single big/small particle (the same data from top of figure 2.4.b) is indicated by red shading, and their respective mean is marked by a dashed line.

Positional and size information together allow for a time resolved computation of the interaction parameter, which is shown fluctuating as a black line in graph d) of figure 2.4. The left axis denotes Γ, where averaging yields $\Gamma = 423 \pm 5$. The uncertainty results mainly from the fluctuations of particle size, which in some cases leads to a confusion of big and small particles[5]. The extend of this effect is illustrated by the relative concentration ξ on the right axis. The corresponding gray line shows a similar percentage of fluctuations as Γ (both about 1 %). The interaction parameter is strongly affected by this, because the difference in susceptibilities is of a factor 10. This seems to make the temperature resolution inferior to monodisperse systems, where $\delta\Gamma < 1$ is possible. However, since particles *not really* change their respective sizes/susceptibilities, this large standard deviation is a worst case scenario, and effective fluctuations are much less. This can be seen later in measurements where the

---

[5] Because the calculation of Γ depends on the density n which is accessed by the averaged Voronoi area, it is of major importance to consider *all* particles. This poses a problem with tracked data, because even in the best dataset single particles are lost, yielding a corruption of n. Thus, untracked data without size correction is used here.

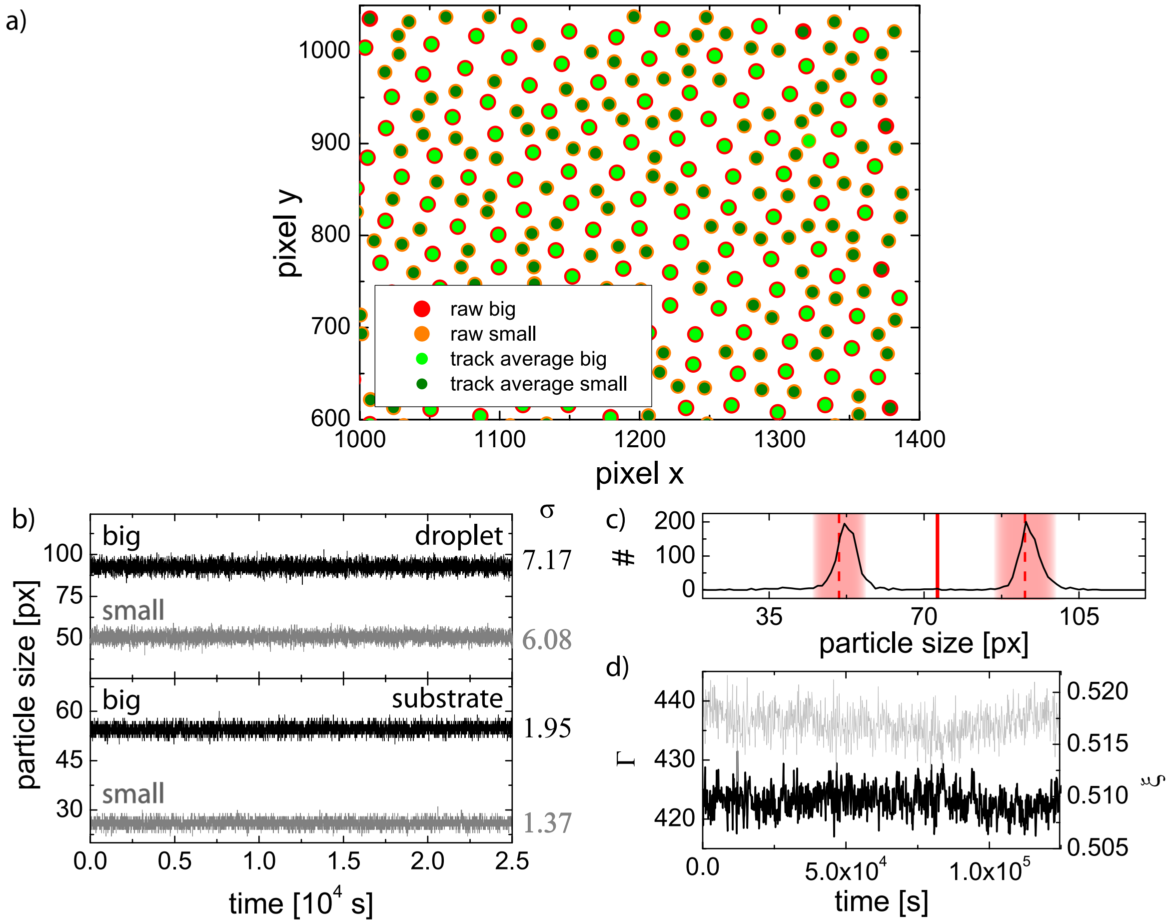

Figure 2.4.: **Particle size separation.**

a) Particle tracking with initial (red/orange) and averaged (light/dark green) size information.

b) Size fluctuation of single big and small particles over time. Top shows data from the droplet, bottom from the substrate. σ to the right gives the respective variance.

c) Particle size distribution averaged over $5 \cdot 10^4$ frames. The red vertical line discriminates between big and small particles. Dashed red lines and shading indicate the average size of a single big/small particle and it's variance, respectively.

d) Time resolved interaction parameter for $120 \cdot 10^3$ seconds (black line). The fluctuation of the mixing ratio ξ (gray line) illustrates the uncertainty in particle size for a single frame.

magnetic field is increased by just a tad, leading reliably to an increase in average Γ significantly smaller than the uncertainty found here.

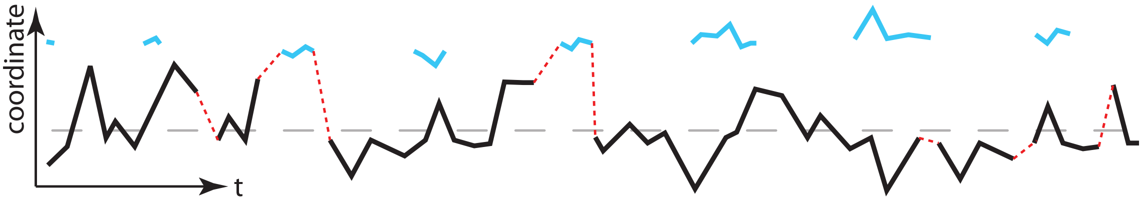

Figure 2.5.: **Schematic of the modified tracking procedure.**
Supposing some artifact generating ‘false’ positional data (light blue) in the vicinity of a real trajectory (black), the original tracking code would unambiguously incorporate those false points into the track (red dotted lines). By averaging over the end parts of existing trajectories and mending based on the corresponding centers of mass (gray dashed line for the ‘real’ track), the correct tracks are reproduced instead.

Particle tracking on substrates

While the original tracking code written by Crocker nearly 20 years ago yields convincing results for all measurements on a system at the water-air interface (even for measurement times up to 12 days), reduced image quality and lower spatial resolution in substrate cells cause a ‘particle loss’ from frame to frame. These ‘optical defects’ are mainly due to impurities in the PMMA coating. As a consequence, the established bonding network of the tracking code now contains invalid connections between particles and artifacts. For this reason, the classical algorithm was significantly extended. In a first run, only extremely obvious spatial-temporal connections were allowed (short spatial displacement and no time gaps), resulting in an extremely high number of very short tracks. The main idea was then to mend these short tracks and thus making it more likely to connect chunks of ‘real’ trajectories. By the introduction of certain mending criteria, the incorporating of ‘phantom’ positions into longer trajectories is prevented. This is illustrated by an example in figure 2.5. By averaging over the end parts of already existing trajectories, two centres of mass were determined for every track. With a recently developed tracking method based on the linear description of all tracking possibilities [Wöl13], these centres of mass are effectively treated as particles and tracked once again. This procedure is repeated multiple times with increased tolerance towards larger spatial displacements and longer temporal gaps, yielding minimal losses even in noisy data. While the original Crocker and Grier routine loses 75 % of the initial particles in a test run of $50 \cdot 10^3$ frames, this novel approach developed by Herbert Kaiser for three-dimensional confocal data managed to keep the loss below 10 %.

2.2.4. Setup control mechanisms

To provide a completely flat two-dimensional interface for unperturbed measurements, several aspects of the experiment have to be regarded with great care. Of capital importance is the droplet volume regulation. Inaccurate volume control leads to a curved surface, either convex or concave, resulting in an inhomogeneous density distribution of the colloids. The same is also true for the inclination control, which comes second. Since there are no friction forces between particles and interface, any tilt also influences density. Further, the user requires accurate control over interaction strength and camera positioning. In the following subsections, details are given on each control parameter.

Droplet volume regulation

The big challenge of the experiment described in section 2.2.2 is to reach an equilibrated state, where no other forces besides the direct particle-particle interactions influence the systems behaviour (excluding gravity and counterforce from the surface tension). This state is first and foremost realized by providing a completely flat water-air interface, which acts as an ideal hard wall.

The amount of water in the droplet was controlled by a micro actuator driven syringe. A continuous regulation in the nanoliter range was necessary to compensate evaporation even in a sealed cell, which would vary with time. Reasons are, for example, a change in water vapor saturation of the air in the sealed volume below the droplet interface and adsorption properties of the copper block due to slight temperature changes. Also, an aging of the anti fogging sheet was observed, altering the amount of absorbed liquid.

This calls for a somewhat flexible solution. Hence, the regulation mechanism was based on the number of particles in the field of view. In a perfect spherical geometry, a decrease of particles indicates flow to the cell edges due to a concave interface, while an increase of particles corresponds to an inflow and thus a convex interface.

A modified *proportional-integral-differential* (PID) feedback loop determined the necessary syringe displacement to keep the system in its current state. This worked as following: First, the desired number of particles would be set (*set point value* N_0) by the user. From this, the difference ΔN_t to the actual value was determined in every frame and stored for the time T (approximately two minutes) in an array $\Delta N(t)$. The proportional term grows linearly with ΔN_t: $I_P = g_P \cdot \Delta N_t$. The differential term $I_D = g_I \cdot \partial \Delta N(t)/\partial t$ supports I_P if $\Delta N(t)$ is growing (i.e. if the system evolves in the wrong direction away from the set point); else it becomes negative and effectively damps the evolution towards the set point, thereby preventing overshoots. Finally, the integral term $I_I = g_I \cdot \int \Delta N(t) \mathrm{d}t$ provides the means to eventually reach the set point, since a pure proportional and differential loop would always miss it by a small margin in a non-conservative system (a system with loss) [Opp72]. The constants g_P,

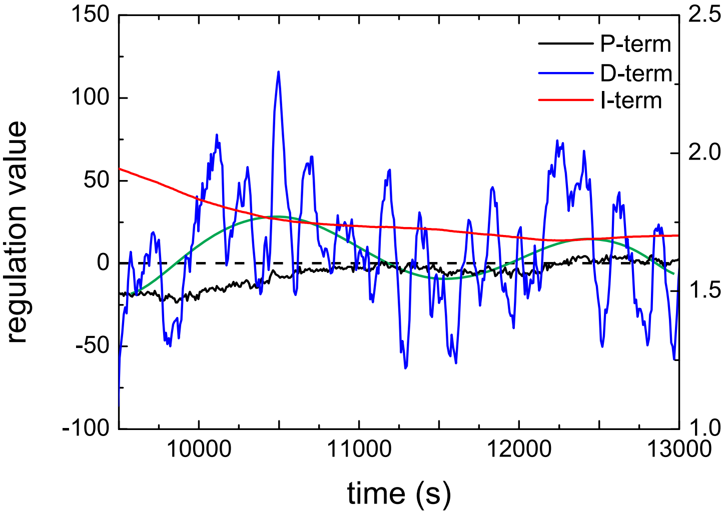

Figure 2.6.: **PID data.**
The graph shows the fluctuations of P, I and D-terms and how they react with respect to one another. The left axis displays the regulation values for P and D-terms, the right axis those for the I-term, which is much smaller. The green line is a guide to the eye. For details, see text.

g_D and g_I are gain factors and have to be determined heuristically. Thus, the syringe displacement factor adds up to $I = I_P + I_D + I_I$.
In figure 2.6, the proportional, integral and differential terms are plotted over 3500 seconds. The left axis corresponds to data of the P and D-terms, while the right axis corresponds to the I-term. The P-term (black) starts with a negative value, i.e. the set point for the particle number is exceeded and the syringe hence needs to be retracted. Because the slope of the P-term is positive towards the set point, i.e. ΔN_t becomes smaller, the D-term (blue) 'brakes' by attaining a positive value. As the slope of the black curve becomes smaller again around $11 \cdot 10^3$ seconds, the D-term falls towards zero. It even becomes negative once the P-term reverses its trend and starts growing into the negative numbers again at around $11.5 \cdot 10^3$ seconds. For clarity, a guide to the eye has been introduced (green), averaging out the fluctuations of the D-term.
In the beginning, the I-term (red) drops from an arbitrary starting value of about 2 towards 1.75, because the syringe is retracting. The decay slows, however, once the set point is reached by the P-term and reverses even in the end, when the P-term eventually overshoots into positive values, indicating a drop in particle number below the set point.

Another regulation method focuses on the apparent size of particles. With the interface leaving the focal plane, the particles appear blurred and therefore 'larger'. Setting the experiment up with the focal plane slightly below the interface, an increase in particle size translates into the loss of water, as the interface further retracts. A decrease, on the other hand, indicates an increased droplet volume, because the interface now draws near the focal plane. This method has been applied in earlier works [Ebe08a, Kei05, Dil11]. It has turned out, however, that the application of a direct number control is much easier. This has several reasons. For example, while it is possible with the size control to keep the interface at a fixed height, its correct position is not known a priori, i.e. one might accidentally stabilize a curved interface. This can only be avoided if the approximate density (determined in the preparation steps as described in section 2.3.1) is known and the water supply directly regulated onto that. Another issue is the change of apparent size with fluctuating density. In an indirect illumination as sketched in figure 2.3, where only scattered light is imaged onto the CCD camera, particles will also mutually shed light onto each other, increasing the registered brightness. Increased density implies also a rise in scattering, and thus overall increased intensity, resulting in a virtual growth of particle size. Further, adequate illumination is another prerequisite to establish this technique. Poor brightness distorts the typical height-size profile, which should exhibit a pronounced minimum at the focal plane. Dark and noisy images produce rather flat profiles. While in general proper illumination is easy to realize, the large tweezers objective mounted in the setup obstructed the direct optical path, such that the light guides had to be mounted under a steep angle (see chapter 2.2.2), leaving the images relatively dark. Thus, the direct number control mechanism worked much more reliable.

Inclination control

When colloids move across the interface, they experience almost no friction. The only small contribution may be attributed to the deformation of the interface by a particle's gravitational force, very much like a marble on an elastic rubber membrane. A force pushing a particle continuously forward also has to deform the interface constantly, thus trapping the particle in a slight potential well. However, there is another mechanism modifying dynamics. In contrast to solid substrates, where the presence of a wall with stick boundary conditions hinders particle motion [Gol67], the water-air interface enhances diffusion. This behaviour originates from the reduced flow field around a single particle. The amount of surrounding liquid, which has to be moved in order to allow particle motion, is basically reduced by a factor of two compared to the bulk due to the broken symmetry. Without friction between liquid molecules and a solid surface, it becomes easier for particles to move. The effect somewhat counters the deformation of the interface.

Since there is virtually no equivalent to adhesion, the system exhibits a very pronounced sensitivity towards inclination. As it turns out, the colloids on the interface are susceptible to tilting in the microrad regime[6].

---

[6] Note that 1 μrad corresponds to an elevation of 6 nm over the diameter of the cell (6 mm).

A tilt of the system has various origins. From an experimental point of view, it is impossible to mount a sample cell with the required precision of horizontal alignment. Its edges are pressed into thermal conductive paste for airtight sealing, so with each mounting attempt the tilt will be different. This initial inclination is of the order of several hundred microrads. It is crucial for the success of the experiment to flatten this out immediately. Otherwise, extreme accumulation of particles on the lower parts of the cell might deform the interface strongly enough to generate a massive bucket. Once trapped in there, it becomes impossible to separate the colloids again. Furthermore, in a binary system, the different mobilities lead to fast demixing, which is impossible to revoke.
After mounting and eventual alignment, it turns out that the inclination is not stable over time. Although an air conditioning system[7] keeps the laboratory temperature constant with a precision of approximately ±1 °C, thermal deformations of the whole building accumulate easily up to a few hundred microrads. Thus, a constant inclination control has to be provided.

This control is realized by mounting the experiment on a base plate supported by a tripod. Two of its three distantly attached legs are heavy duty actuators, offering a precision in the micrometer range. An inclination sensor with microrad resolution was mounted on the base plate as well (see section 2.2.2 for gear details). A software-based coupling (proportional feedback loop) allows to preserve any given inclination. In figure 2.7, the sensor data is plotted over a time range of 250 hours along with actuator displacement. The variance in the angle amounts up to $0.5\,\mu$rad, whereas the actuators position changes rather irregularly up to 10 microns to compensate for the measured changes in tilt. Figure 2.7.a) exhibits three sets of spikes, which are attributed to the movement of the camera during automated scans (every two hours, see below). During measurements, the scans are deactivated, i.e. figure 2.7.a) comprises of three measurements and the successive equilibration times. Figure 2.7.b) reveals the influence of the day and night cycle on thermal material expansion, as the spikes show a periodicity of 24 hours.
By taking subsequent images along the x- and y axis of the sample cell and evaluating the respective particle numbers, density profiles can be extracted, very much like an extremely precise mason level. This procedure was automated and repeated every two hours. The evolution of these profiles hints towards the inclination of the interface. From this, the experimentalist is able to balance out the interface over the course of some weeks up to a few month by adjusting the actuators accordingly.

---

[7] The air condition of the University of Konstanz is actually no real thermostat, but rather a conventional ventilation system offering a certain amount of temperature modification. The air flow temperature is moderated by water of the Lake Constance which is retrieved at a depth of 16 metres. There, the water temperature is supposedly constant throughout the year.

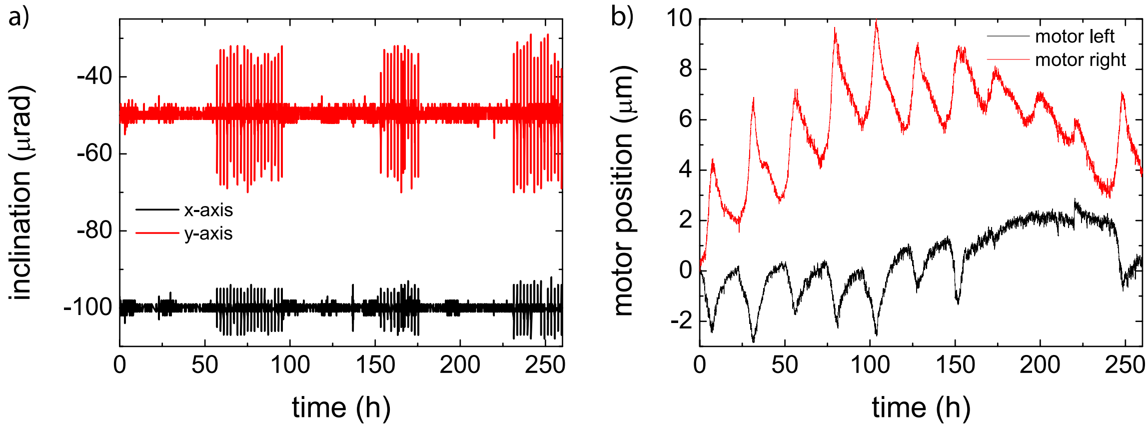

Figure 2.7.: **Inclination data.**
a) Data from the inclination sensor. A feedback loop controlling the base plate motors aims for a user-defined tilt, in this case -100 and $-50\,\mu$rad.
b) Motor positions resulting from the regulation onto the inclination data presented to the left. To compensate material expansion due to the day and night rhythm, the motors move as much as $2\,\mu$m.

Software control

Once a sample is mounted, the experiment is almost fully controllable via computer. This is only natural as the experiment has to be regulated actively, as described in prior sections. The software used is written in IDL (*Interactive Data Language*, ITT VIS), a script-like programming language specialized in array operations. Up to this day, the setup control program contains approximately 26000 lines of code.
Besides direct control of the micro actuators driving syringe, camera and inclination, the user may also alter the current of illumination and magnetic field digitally by addressing a custom build power supply (Martin Clausen, *http://www.rotgradpsi.de/mc /iconst/index.html*) equipped with a serial port. A server instance of a remote access software (*ultraVNC*, freeware under the GNU General Public License, *www.uvnc.com*) running nonstop allows log in from virtually any computer with Internet connection. This is necessary for either timing measurement runs remotely or active intervention on the automated regulation mechanisms in case of a resonant build up. To inform the experimentalist of an imminent crash of the droplet, the software calls an external Windows command line utility (*Blat*, public domain software, *www.blat.net*) which sends an email to the user. By addressing this email to a commercial web service which provides a short message service (SMS) notification service, the experimentalist may be alerted by his cellphone. The employment of this cycle is triggered if the set value of the particle number in the field of view deviates from the actual parameter by a given amount. Because this mechanism might fail in case of a computer crash/freeze,

a second computer was used to check on the hard drive activity. Because log files containing inclination data, particle number etc. were written constantly, any break could be recognized with a delay of some seconds, triggering the second computer to send the notification message.

2.3. Sample preparation

2.3.1. Colloidal suspension

Prior to the first experiments, a base solution of dispersed solution was prepared. From this, a small amount was taken and inserted into the setups sample cell with a high precision laboratory pipette (*Eppendorf* Research 100). Usually, a volume of approx. $15\,\mu$l filled the cell to a sufficient extend where mounting into the setup would be possible.

To achieve the desired absolute concentration of particles in the field of view as well as the mixing ratio of big and small particles aimed for, pre-base solutions for each individual species were prepared seperately. Given that each of these suspensions had the doubled absolute concentration aimed for this particular species, mixing equal amounts of both solutions resulted in a sample with the desired properties. This procedure proved to yield much more accurate results than the attempt of directly matching concentrations in a single sample.

To prepare the pre-base solutions, the preserving agent Thimerosal (salt of a mercury compound) was added to deionized water[8]. Highly poisonous, it prevents bacteria growth as the suspensions are needed to stay unperturbed for quite some time[9], even if used in low concentrations (from a $2\,\%$ Thimerosal base solution, $1\,\mu$l/ml was added to the samples). Both particle species are commercially available (big particles: *Dynabeads* M-450 Epoxy, small particles: *Dynabeads* M-270 Epoxy, see figure 2.8 for SEM micrographs). While the big particles came suspended in a dense aqueous solution, the small particles were delivered as dried powder and had to be dissolved in the water-Thimerosal mixture prior to any tuning of the concentration. To prevent aggregation of particles due to Van der Waals forces, the sterically stabilising agent sodium dodecyle sulfate (SDS, *Sigma Aldrich*, structure formula $C_{12}H_{25}NaO_4S$) was added. This anionic surfactant binds with its non-polar end to the epoxy-coated spheres, preventing the approach of two coated spheres entropically. Because SDS is known to dissolve with time, care was taken to only use freshly synthesized agent (not older than one year). To provide full coverage of all spheres, the amount of added SDS was

---

[8] Taken from a *Millipore* Sympack 2 water purification apparatus.

[9] In principle, the sample needs to be mounted only once to perform all desired measurements. Usually, however, a few attempts until a droplet is stable are necessary. Furthermore, since once stable, a droplet might stay mounted for a couple of month (ideally more than a year), biologically and chemically stable suspensions are essential.

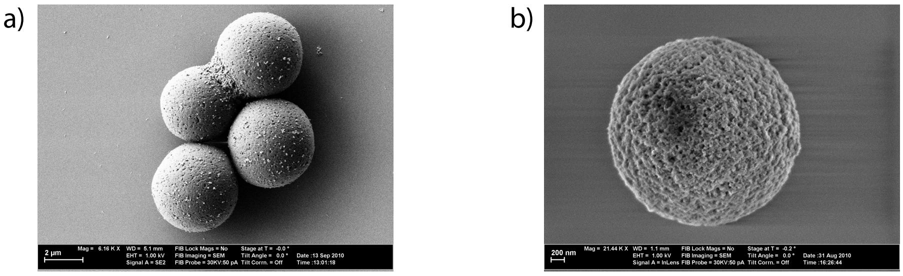

Figure 2.8.: **SEM micrographs of the colloids used in this work.**
a) Type B particles: *Dynabeads* M-450 Epoxy.
b) Type S particles: *Dynabeads* M-270 Epoxy.

chosen to be 95 % of the critical micelle concentration (CMC, approx. 2.3 g/l). The constituents were filled into a teflon vial (*Thermo Scientific* Nalgene Centrifuge Ware, Teflon FEP fluorinated ethylene propylene, 8 ml), allowing mixing on a vortex shaker before attaching to a caroussel, constantly turning the samples and dipping them into an ultrasonic bath. Keeping this procedure running for two days ensured the sufficient stabilization of the suspension.

To achieve the desired concentration of particles, a defined volume of the suspension was taken and put into the sample cell, with the notch facing upward. That allowed particles to sediment homogeneously to the water-glass interface, where they could be counted with a microscope. Careful addition of pure water-Thimerosal mixture and the repetition of the measurement allowed for a rather precise adjustment of the concentration and eventual mixing ratio.

2.3.2. Substrate cells

Cells were made from two kinds of commercially available cover slips (*Menzel*, 20 × 20 mm, thickness 0.5 mm for the base and *Plano GmbH*, diameter 16 mm, thickness 0.5 mm for the lid), and thin rings custom made from glass tubes (*Universität Konstanz*, Wissenschaftliche Werkstätten). A larger ring (outer diameter 13 mm, inner diameter 10 mm) was glued to the lid with UV glue (*Norland*, optical adhesive 81) while a smaller ring (outer diameter 9 mm, inner diameter 6 mm) was glued to the base substrate. The height of the inner ring was chosen slightly larger (1.1 mm vs. 0.7 mm) so that there would be a slit between outer ring and base if the cell was closed. With the right volume of water (approx. 60 μl) in the cell, a meniscus formed and the lid could be closed without the inclusion of air bubbles. Excess water simply flowed out. The assembly procedure is sketched in figure 2.9. The lid was irreversibly fixed to the base with a two component silicone rubber glue (*Roth* Rhodorsil RTV 3250 LV and Rhodorsil Cata K11). This glue was preferred over the commonly used UV glue because of its inherently chemical stability. As it turned out in numerous tests,

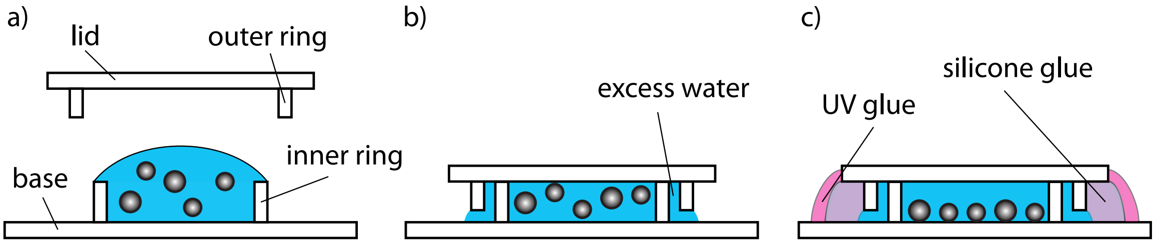

Figure 2.9.: **Cell assembly (not to scale).**
a) An amount of suspension, larger than the cell volume, is put into the cells base, forming a meniscus.
b) Closing the lid with the attached outer ring pushes the excess water out, preventing air bubbles from entering the cell.
c) The lid is glued to the base. While it hardens, particles are sedimenting down and equilibration can begin already.

the not-yet-hardened UV glue dissolved partly in water and influenced the chemical stability of the particles (details can be found in the next paragraph). However, as the silicone rubber glue did not provide the necessary long time stability regarding air tightness, multiple outer layers of UV glue were applied over a timescale of 12 hours. Prior to assembly, the cover slips had to be chemically treated. First, any dirt had to be removed as scattered light would interfere with optical perception and distort the particle tracking algorithms. Second, an untreated glass surface was found to increase the pinning chance of particles (easily larger than 20 %). This was especially true for small particles.
Both lid and substrate base were treated following the protocol

- 5 min exposure to acetone in an ultrasonic bath
- 5 min exposure to ethanol in an ultrasonic bath
- 10 min exposure to a piranha bath (50 : 50 hydrogen peroxide and sulfuric acid mixture)
- 5 min exposure to ethanol in an ultrasonic bath

Between all steps, the cover slips were flushed with either ethanol or deionized water. While this procedure held optical clean surfaces, a thin film of the polymer poly(methyl methacrylate) (PMMA, *MicroChem* 950 PMMA A4, $C_5H_8O_2$) was deposited onto the base substrate to improve the particle dynamics above the surface by prohibiting sticking to it. Prior to this procedure, a dehydration bake was performed on a hotplate at 110 °C for 10 min, as the adhesion of the polymer to the glass surface suffers significantly from traces of water. Approximately 25 μl PMMA were spin-coated for 60 s at

5000 rpm. The substrate was baked afterward for 30 minutes at 170 °C. This approach held a PMMA film thickness of approximately 200 nm, yielding a pinning strength of $\approx 1\,\%$. The film thickness was tested by AFM measurements, where a coated substrate was sliced with a scalpel. The remaining cut would give a good estimation for the film thickness. A 3D reconstruction of an AFM measurement is shown in figure 2.10.a).

The cells assembled following this method exhibited a lifetime of several month before air bubbles could penetrate the inner ring and make particle tracking impossible. This proved to be enough time for equilibration and some measurement cycles.

Suspension stability in substrate cells

The construction of closed substrate cells caused some (chemical) problems with the stability of the colloidal suspensions, as mentioned in the preceding paragraph. First, the chemical treatment of the substrate had a substantial impact on pinning strength. Untreated SiO_x-surfaces might capture the terminal Na-ion of the dissolved SDS [Koh00] and hence develop a positive partial charge, attracting the polar end of the SDS shell on particles and thus effectively pinning those. Pure glass substrates indeed exhibited a pinning strength $> 20\,\%$.

Treatment with chlorodimethylsilane $(CH_3)_2SiCl_2$ or propyltrimethoxysilane $C_3H_7Si(OCH_3)_3$ would partially prevent that, although an increased fraction of small particles would still bind to the surface. The amount of those pinning particles varied, but was generally of the order of $\approx 10\,\%$. This mechanism, addressing primarily small particles, is not yet understood. It might be connected with observations made in earlier works, where the addition of SDS to suspensions of small particles led to aggregation [Kön03]. Although this issue was resolved later [Ebe08a] by attributing it to old (degenerated) stabilizing agent, it is possible that it does not bind thoroughly to small particles[10] such that those might suffer from occasional Van der Waals binding to the surface. Additional evidence for this speculation is found in the fact that in the case of silanized substrates, the fraction of pinning (small) particles increased over time. A solution was found, as mentioned already, by coating the substrate with PMMA.

However, the usage of UV glue proved to be much more problematic. While the suspensions seemed stable at first, a recessive repulsion could be observed after several days. Snapshots from such a sample are shown in figure 2.10.b). The micrographs to the left and right were taken directly after mounting and two weeks after, respectively. While in the first graph, the system was fluid ($\Gamma = 10$), the second graph should show a frozen glass ($\Gamma = 314$). Instead, the particles in the latter do not exhibit any kind

---

[10] Note that in [Ebe08a], no sterically stabilizing agent was added to the suspension of small particles. Yet, they did not aggregate. In this thesis, SDS was added in the same concentration as to the big particle suspension, causing no problems at all.

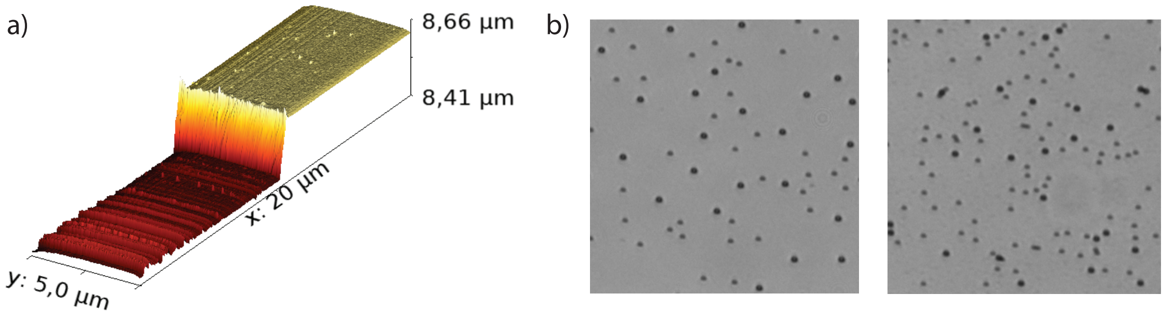

Figure 2.10.: **Properties of solid substrates.**
a) AFM profile of a cut in the PMMA film, revealing a thickness of $\approx 200\,\mu$m.
b) Micrographs of a UV glued sample cell directly after mounting at $\Gamma = 10$ (left) and after two weeks at $\Gamma = 314$ (right).

of interaction, leading to the conclusion that the susceptibility must have decreased dramatically. An explanation for that peculiar (reproducible) phenomenon may be given by dissolving terminal groups of the UV glue's polymer chains upon contact with water. With free radicals, these microscopic molecules might diffuse into the polystyrene matrix of the colloidal beads and react with the iron oxide doping. If the maghemite Fe_2O_3 is oxidized into magnetite $Fe^{2+}(Fe^{3+})_2O_4$, the magnetic response decreases dramatically. The effect is stronger for the small particle species due to the more inhomogeneous doping with increased concentration at the bead edges [Ebe08a] and maybe less epoxy coating. Therefore, systems with only big particles suffer much less from this phenomenon [Pol14]. To circumvent this problem, different glues have been tried. As it turned out, all of them had some drawbacks as low viscosity or an inadequate air tightness for longer time periods. Therefore, this matter was finally settled by using a combination of a silicon rubber glue and the UV glue, where the former shields the suspension from the latter, which in turn provides the necessary long time stability.

3. Elasticity of glasses

Traditionally, the diverging relaxation times in non-ergodic systems are associated with a severe increase in viscosity [Ang95, Deb01]. Coming from the liquid side, a disordered system has been called a 'glass' if its viscosity η exceeds 10^{13} poise, and thus defining the glass transition temperature T_G. This rather loose definition is difficult to apply to soft matter systems. On the one hand, this is attributed to their 'soft' interaction energy which is lower up to a factor of 10^{10} in two dimensional systems (and even 10^{15} times smaller in three dimensions), which contradicts the idea of universality. On the other hand, as a macroscopic property, the viscosity is very hard to determine in mesoscopic soft matter systems. Hence, other quantities might prove more useful in discerning a liquid from its glassy state. In colloidal systems, a direct (microscopic) measure of dynamics and relaxation times are mean squared displacement (MSD) or intermediate scattering functions (ISF) [Cha95, Han06]. From those alone, however, it is difficult to judge on the system's state because the effects of a transition in these functions can be subtle. This is problematic especially in experimental data where external perturbations may distort the results. For ideal glasses, an infinitely long plateau is expected which reflects the divergence of viscosity. Real glasses, however, will eventually show alpha-relaxation, where the plateau of the MSD crosses over into a subdiffusive part. This relaxation may have various origins (e.g. cooperative motion/drift, Mermin-Wagner fluctuations), and may be even affected by aging phenomena [Gre06, Wol08].

The measure of viscosity inherently considers the medium from the fluid side. Here it is suggested to change the point of view and start in the solid state. Thinking of glass as a 'solid', it is intuitive to study the elasticity in the transition region. Obviously, the two states have very distinct and characteristic elastic response functions. While the bulk modulus, governing the behavior of a system under compression, might not change significantly, the shear modulus is the quantity which *defines* the solid. It is expected to change from zero in the fluid phase (exhibits no resistance to shear) to a finite value in the amorphous solid phase (has a finite response to shear) [Bar88]. As it turns out, this finite growth is far more easy to measure than the divergence of any function, be it macroscopic as the viscosity or microscopic as a relaxation time.

The elasticity of glasses naturally has evoked some interest in the community. In numerous papers, the behavior of the shear modulus μ at the glass transition was discussed. This subject was tackled for example in [Bar88], where statistical uncertainties prevented the authors from drawing a definite conclusion. Recent replica theory approaches predicted a continuous increase from zero upon cooling [Yos10, Yos12]. These results coincide with predictions of theory of granular matter. In those athermal systems, critical fluctuations close to the jamming transition are reported to cause a growth of shear rigidity which follows an algebraic law [O'H03]. On the other hand, more recent replica calculations come to the conclusion that μ performs a discontinuous jump at the glass transition [Sza11]. The same scenario is also predicted by mode coupling calculations [Leu84, Göt85]. This was further backed up by recent hard disc simulations [Kli12].

The following section gives a short introduction to basic solid state theory [Ash09a] and introduces the method which is used later to obtain basic results. After a short introduction to elasticity theory [Lan95], the final results including a discussion are presented.

3.1. Dispersion curves of phonon modes

3.1.1. The dynamical matrix

The total potential energy of the system is given by the sum over all pair potentials between all particles:

$$U(|\mathbf{r}-\mathbf{r}'|) = \frac{1}{2}\sum_{\mathbf{r},\mathbf{r}'} \phi(\mathbf{r}-\mathbf{r}')\,.$$

The particle positions are separated into a static and a dynamic part. The static part $\mathbf{R}$ references the equilibrium position, while the dynamic part expresses the particles displacement $\mathbf{u}(\mathbf{R},t)$:

$$\mathbf{r}(\mathbf{R}) = \mathbf{R} + \mathbf{u}(\mathbf{R},t)\,.$$

With this, the systems potential energy at e.g. $t=0$ (or any other given time) can be written as

$$U(|\mathbf{r}-\mathbf{r}'|) = \frac{1}{2}\sum_{\mathbf{R},\mathbf{R}'} \phi(\mathbf{R}-\mathbf{R}'+\mathbf{u}(\mathbf{R})-\mathbf{u}(\mathbf{R}'))\,.$$

Expansion of the energy holds

$$\begin{aligned} U(|\mathbf{r}-\mathbf{r}'|) &= U_0 + U_{\text{lin}} + \frac{1}{4}\sum_{\mathbf{R},\mathbf{R}'}[(\mathbf{u}(\mathbf{R})-\mathbf{u}(\mathbf{R}'))\nabla]^2\phi(\mathbf{R}-\mathbf{R}') \\ &= \frac{1}{4}\sum_{\mathbf{R},\mathbf{R}'}\sum_{\mu,\nu=x,y}(u_\mu(\mathbf{R})-u_\mu(\mathbf{R}'))\Phi_{\mu\nu}(\mathbf{R}-\mathbf{R}')(u_\nu(\mathbf{R})-u_\nu(\mathbf{R}')) \end{aligned}$$

with $\Phi_{\mu\nu}$ being the second derivative of the interaction potential, where $\mu, \nu \in x, y$ are the vectorial components in two dimensions:

$$\Phi_{\mu\nu}(\mathbf{r}) = \frac{\partial^2 \phi(\mathbf{r})}{\partial r_\mu \partial r_\nu} .$$

U_0 has an arbitrary value and can therefore be set to zero. The linear term U_{lin} contains the sum $\sum_{\mathbf{R}'} \nabla\phi(\mathbf{R} - \mathbf{R}')$. This corresponds to the negative force exerted on a particle at an equilibrium position $\mathbf{R}$ by all other particles at their respective equilibrium positions. Since in equilibrium there must be no net force, U_{lin} is also zero. By introducing the tensor $\underline{\mathbf{D}}$ with components

$$D_{\mu\nu}(\mathbf{R} - \mathbf{R}') = \left(\delta_{\mathbf{R},\mathbf{R}'} \sum_{\mathbf{R}''} \Phi_{\mu\nu}(\mathbf{R} - \mathbf{R}'') \right) - \Phi_{\mu\nu}(\mathbf{R} - \mathbf{R}') , \tag{3.1}$$

the expression for the harmonic part of the potential energy simplifies to

$$U^{\text{harm}} = \frac{1}{2} \sum_{\mathbf{R},\mathbf{R}'} \sum_{\mu,\nu} u_\mu(\mathbf{R}) D_{\mu\nu}(\mathbf{R} - \mathbf{R}') u_\nu(\mathbf{R}') . \tag{3.2}$$

$\underline{\mathbf{D}}$ is called the stiffness matrix. Introduction of two identities $\delta_{\mathbf{R},\mathbf{R}'}$ and $\delta_{\mathbf{R}'',\mathbf{R}'''}$ leads to a notation in which the potential energy is given by the sum over the so-called ‘dynamical matrix’:

$$\begin{aligned}
U^{\text{harm}} &= \frac{1}{2} \sum_{\mu,\nu} \sum_{\mathbf{R},\mathbf{R}',\mathbf{R}'',\mathbf{R}'''} u_\mu(\mathbf{R}) \delta_{\mathbf{R},\mathbf{R}'} D_{\mu\nu}(\mathbf{R}' - \mathbf{R}'') \delta_{\mathbf{R}'',\mathbf{R}'''} u_\nu(\mathbf{R}''') \\
&= \frac{1}{2} \sum_{\mu,\nu} \sum_{\mathbf{R},\mathbf{R}',\mathbf{R}'',\mathbf{R}'''} u_\mu(\mathbf{R}) \frac{1}{N} \sum_{\mathbf{q}} e^{i\mathbf{q}(\mathbf{R}-\mathbf{R}')} D_{\mu\nu}(\mathbf{R}' - \mathbf{R}'') \\
&\quad \times \frac{1}{N} \sum_{\mathbf{q}'} e^{i\mathbf{q}'(\mathbf{R}''-\mathbf{R}''')} u_\nu(\mathbf{R}''') \\
&= \frac{1}{2N^2 v_0^2} \sum_{\mu,\nu} \sum_{\mathbf{q},\mathbf{q}'} \underbrace{v_0 \sum_{\mathbf{R}} e^{i\mathbf{q}\mathbf{R}} u_\mu(\mathbf{R})}_{u_\mu^*(\mathbf{q})} \sum_{\mathbf{R}',\mathbf{R}''} e^{-i\mathbf{q}\mathbf{R}'} D_{\mu\nu}(\mathbf{R}' - \mathbf{R}'') e^{i\mathbf{q}'\mathbf{R}''} \\
&\quad \times \underbrace{v_0 \sum_{\mathbf{R}'''} e^{-i\mathbf{q}'\mathbf{R}'''} u_\nu(\mathbf{R}''')}_{u_\nu(\mathbf{q}')} .
\end{aligned}$$

$\delta_{\mathbf{R},\mathbf{R}'} = \frac{1}{N} \sum_{\mathbf{q}} \exp\{i\mathbf{q}(\mathbf{R} - \mathbf{R}')\}$ is the Fourier transformation of the delta function (the definition of Fourier transformation equations and the resulting identities used here can be found in the appendix, chapter A). $v_0 = \frac{V}{N}$ is the volume of a unit cell. In two dimensions, the value for v_0 (where volume becomes area) varies depending on the underlying structure of the studied system: For a hexagonal crystal with its six-fold symmetry, it equals an area of $\sqrt{3}a_0^2/2$, where a_0 denotes the interparticle distance. For a disordered system, on the other hand, v_0 is not well defined. However, it may be approximated by simply ignoring any geometrical prefactors such that $v_0 = a_0^2$ (compare section 2.1.1).

Carrying on with the simplification of U^{harm}, using the relation $\mathbf{R}^* = \mathbf{R}'' - \mathbf{R}'$, one sum over $\mathbf{q}$ can be eliminated:

$$\begin{aligned} U^{\mathrm{harm}} &= \frac{1}{2V^2}\sum_{\mu,\nu}\sum_{\mathbf{q},\mathbf{q}'} u_\mu^*(\mathbf{q}) \sum_{\mathbf{R}',\mathbf{R}^*} D_{\mu\nu}(\mathbf{R}' - (\mathbf{R}' + \mathbf{R}^*)) e^{-i\mathbf{q}\mathbf{R}'} e^{i\mathbf{q}'(\mathbf{R}'+\mathbf{R}^*)} u_\nu(\mathbf{q}') \\ &= \frac{N}{2V^2}\sum_{\mu,\nu}\sum_{\mathbf{q},\mathbf{q}'} u_\mu^*(\mathbf{q}) \sum_{\mathbf{R}^*} D_{\mu\nu}(\mathbf{R}^*) e^{i\mathbf{q}\mathbf{R}^*} \underbrace{\frac{1}{N}\sum_{\mathbf{R}'} e^{i\mathbf{R}'(\mathbf{q}'-\mathbf{q})}}_{\delta_{\mathbf{q}',\mathbf{q}}} u_\nu(\mathbf{q}') \\ &= \frac{1}{2V}\sum_{\mathbf{q}}\sum_{\mu,\nu} u_\nu^*(\mathbf{q}) \underbrace{\frac{1}{v_0}\sum_{\mathbf{R}''-\mathbf{R}'} D_{\mu\nu}(\mathbf{R}'' - \mathbf{R}') e^{i\mathbf{q}(\mathbf{R}''-\mathbf{R}')}}_{D_{\mu\nu}(\mathbf{q})} u_\nu(\mathbf{q})\,. \end{aligned}$$

Renaming $\mathbf{R}''$ to $\mathbf{R}$, the Fourier transformed stiffness matrix

$$\underline{\mathbf{D}}(\mathbf{q}) = \frac{1}{v_0}\sum_{\mathbf{R}-\mathbf{R}'} \underline{\mathbf{D}}(\mathbf{R} - \mathbf{R}') e^{-i\mathbf{q}(\mathbf{R}-\mathbf{R}')} \tag{3.3}$$

is called ‘dynamical matrix’. Making use of equation (3.1), $\underline{\mathbf{D}}(\mathbf{q})$ can be calculated for a given interparticle potential ϕ and particle positions $\mathbf{R}$.

As $\underline{\mathbf{D}}(\mathbf{R} - \mathbf{R}')$ consists of the second derivatives of the interparticle potential, i.e. the derivative of the interparticle force (which equals the spring constant in one dimension), it can be understood as the coupling matrix for the equation of motion. It can be written as

$$M\frac{\partial^2}{\partial t^2}\mathbf{u}(\mathbf{R}) = -\sum_{\mathbf{R}'} \underline{\mathbf{D}}(\mathbf{R} - \mathbf{R}')\mathbf{u}(\mathbf{R}')$$

with M being the mass of a single particle. This differential equation can easily be solved if the time-dependent displacements $\mathbf{u}(\mathbf{R}, t)$ take the form of plane waves $\mathbf{u}(\mathbf{R}, t) = \boldsymbol{\epsilon}\exp\{-i(\omega t - \mathbf{q}\mathbf{R})\}$ with wave vectors $\mathbf{q}$. In this case, the resulting eigenequation

$$M\omega^2\boldsymbol{\epsilon} = \lambda(\mathbf{q})\boldsymbol{\epsilon} = \underline{\mathbf{D}}(\mathbf{q})\boldsymbol{\epsilon} \tag{3.4}$$

contains the dispersion relation $\omega_s(\mathbf{q}) = \sqrt{\lambda_s(\mathbf{q})/M}$. Here, s indicates polarization (longitudinal or transverse). One way to obtain the eigenvalues λ *a priori* is to compute them directly via the characteristic polynomial $\chi = \det(\underline{\mathbf{D}}(\mathbf{q}) - (\underline{\mathbf{I}} \cdot \lambda)) = 0$, where $\underline{\mathbf{I}}$ is the identity matrix. Another way to measure λ is to make use of the equipartition theorem. It assigns the energy of $\frac{1}{2}k_BT$ to every degree of freedom (k_B being the Boltzmann constant and T the temperature). With equation (3.2) one obtains

$$\frac{1}{2}k_BT = \left\langle \frac{1}{2}u^*_\mu(\mathbf{q})D_{\mu\nu}(\mathbf{q})u_\nu(\mathbf{q}) \right\rangle ,$$

since the right side of the equation describes exactly the energy stored in the mode with wave vector $\mathbf{q}$. Following from that, the eigenvalues of $\underline{\mathbf{D}}(\mathbf{q})$ can be computed by

$$\lambda_s(\mathbf{q}) = \frac{k_BT}{\langle u^*_\mu(\mathbf{q})u_\nu(\mathbf{q})\rangle} , \tag{3.5}$$

where the subscript s (polarization) depends on the choice of components $\mu, \nu = x, y$ of $\mathbf{u}(\mathbf{q})$.

In colloidal experiments, the displacement $u_\nu(\mathbf{R})$ of particles is caused by collision with thermally activated solvent molecules and can easily be extracted. $\mathbf{R}$ is determined by averaging the position of a given particle over a defined time window. The choice of size of this window Δt depends on the strength of collective motions such as rotational drift or long range fluctuations [Mer66]. It must be short enough to exclude these influences, but sufficiently long to allow particles the access to their adjacent environment, i.e. Δt must be large enough to prevent an amplitude cutoff. This issue is discussed in detail later (see section 3.2.3).

To evaluate equation (3.5), the definition of a fixed coordinate system becomes necessary to pay respect to the vectorial character of $\mathbf{q}$. In a crystal, this would happen under consideration of the symmetry axes. In an amorphous system, however, the orientation of the axes is arbitrary due to the isotropy. For convenience, the wave vector $\mathbf{q}$ is always chosen to be parallel to the x-axis, i.e. because of the plane wave character, the corresponding eigenvectors $\boldsymbol{\epsilon}$ in equation (3.4) point into $(1, 0)$ (longitudinal) or $(0, 1)$ (transverse) direction.

To obtain a dimensionless master curve, the measured quantity $\langle u^*_\mu(\mathbf{q})u_\nu(\mathbf{q})\rangle^{-1}$ may be plotted in units of $a_0^2/(k_BT\,\Gamma)$ (a_0^2 enters the equations via the Fourier transform in equation (3.3), and equation (3.1) implies that $\underline{\mathbf{D}}(\mathbf{q})$ is linear in Γ).

3.1.2. Results

Review of application on crystalline data

This method was successfully applied to crystalline systems in the past [Kei04]. In the following, the reliability of this approach is proven and compared to a second, more direct method. Furthermore, an estimation for the underlying errors and the resulting uncertainty bands is introduced.

In figure 3.1.a), the band structure of a two dimensional colloidal crystal at $\Gamma = 250$

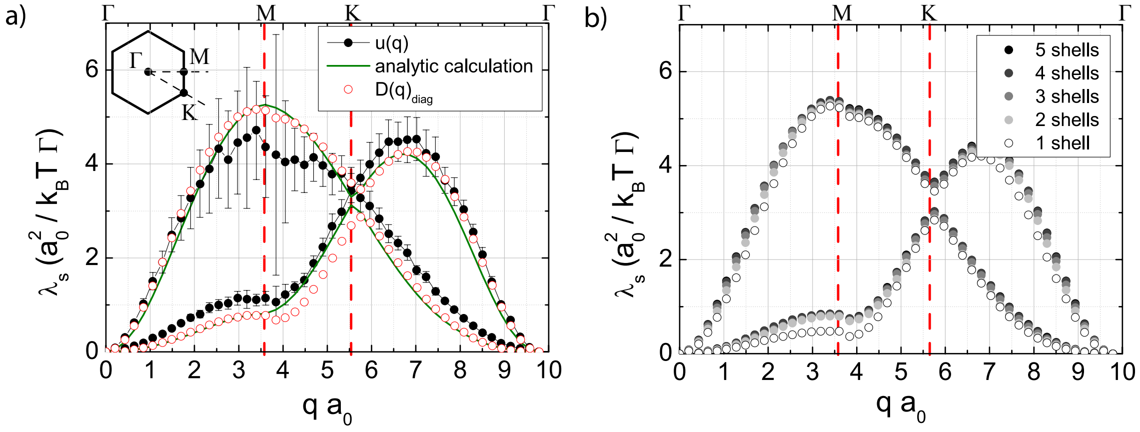

Figure 3.1.: **Crystalline band structure.**

a) Comparison of an analytic $T = 0$ calculation (green line) with experimental data at $\Gamma = 250$ obtained by equation (3.5) (connected black dots). Upper and lower branch correspond to longitudinal and transverse polarisation, respectively. The red open symbols were computed by direct diagonalisation of the dynamical matrix according to equation (3.4). The inset in the upper left corner shows the Brillouin zone with its symmetry points, which are also indicated by the red dashed lines in the main figure.

b) Statistics influence on the direct calculation of the dynamical matrix $\underline{\mathbf{D}}(\mathbf{q})$. After taking into account 4 shells of neighboring particles, the curves have converged already.

with its hexagonal lattice is reproduced (connected black circles) from 2400 particle trajectories covering 7200 s (corresponding to 3600 frames or 'configurations'). To explore the different symmetry axes, the field of view was downsized and rotated. It contained the positions of approximately 900 particles after this processing. The equilibrium lattice positions $\mathbf{R}$ were determined by separating every trajectory into time windows of length $\Delta t = 150$ s and subsequent averaging. This 'chopping' is necessary to exclude drift or long-range positional fluctuations (Mermin-Wagner) which make the system appear softer.

Because of the finite optical resolution, the measured amplitudes of vibrational motion are subject to uncertainty. The accuracy for particle positioning is roughly 0.25 pixels ($\approx$ 150 nm, depending on the used magnification). Error propagation handling and the respective equations are described in the appendix (chapter B). The result shows growing error bars at the edges of the Brillouin zone (for the definition of the Brillouin zone and its symmetry points see inset), where the phonon wavelength becomes comparable to the mean interparticle distance a_0. Naturally, short wavelength detection is more prone to errors due to the finite resolution. Consequently, the curve starts to deviate from an analytic $T = 0$ calculation (solid green line) only in the vicinity of

the M-Point at the Brillouin zone edge (symmetry points are indicated by red dashed lines and corresponding letters above) for $qa_0 \geq 2.5$. All in all, processing of the displacement field yields very convincing results. The agreement with the analytical calculation is quite good, especially since no fit parameter was used for adjustment. The theoretical curve always lies inside the error bars.
Another method to obtain the dispersion bands is to directly calculate the dynamical matrix. In contrast to the analysis of the (dynamic) displacement field, this method relies on a static snapshot of the system. From this, the stiffness matrix $\underline{\mathbf{D}}(\mathbf{R})$ can be computed for every particle, as the interaction potential between the particles is precisely known. Averaging over all particles yields information about the overall elastic responses. Diagonalisation of the Fourier transformed matrix results in the eigenvalues of the dynamical matrix, which are plotted in figure 3.1 as red empty circles. Here, yet better agreement with the theoretical curve is found, especially at the Brillouin zone edge. For the computation, 4 shells of next neighbors were taken into account. As shown in figure 3.1.b), the dispersion bands converge rather fast to a curve independent of the number of shells considered. The smoothness of the curves is achieved by averaging over a finite amount of snapshots, resulting in the equilibrium lattice positions of the hexagonal crystal. The time window for the averaging was chosen also to be $\Delta t = 150\,\mathrm{s}$, as in the preceding analysis.

Dispersion relation of an amorphous system

As shown in [Ebe08b], the structure of a binary colloidal mixture is governed mainly by the spatial distribution of big particles. Since their magnetic susceptibility is an order of magnitude larger compared to the small species, they contribute to the magnetic energy roughly a hundred times more. This is directly coupled to the interaction potential, the ‘spring constant’ between the particles. It was shown, for example, that members of the small fraction are always positioned on the node points of the Voronoi cells constructed of only big particles even for moderate system parameters Γ. The uneven energy contribution of the distinct species will as well have its impact on propagation of vibrational excitations. The amplitude of small particles in a phonon will mainly follow the motion of neighboring big particles. Vice versa, due to the low ‘coupling’, the small species influences the propagation of excitations only marginally. In other words, the elastic behavior of the system is governed by the big particles. Hence, only the displacement field of big particles was taken into account for the following analysis.

Figure 3.2.a) shows the computed dispersion relations of the system for different interaction parameters (different temperatures). The data was acquired over at least $36 \cdot 10^3$ seconds each, considering $\approx 13 \cdot 10^3$ statistically independent configurations (frames) of ≈ 2000 particles. The time window Δt to determine the equilibrium positions $\mathbf{R}$ was chosen to $18 \cdot 10^3$ seconds. Graphs to the left and right discriminate

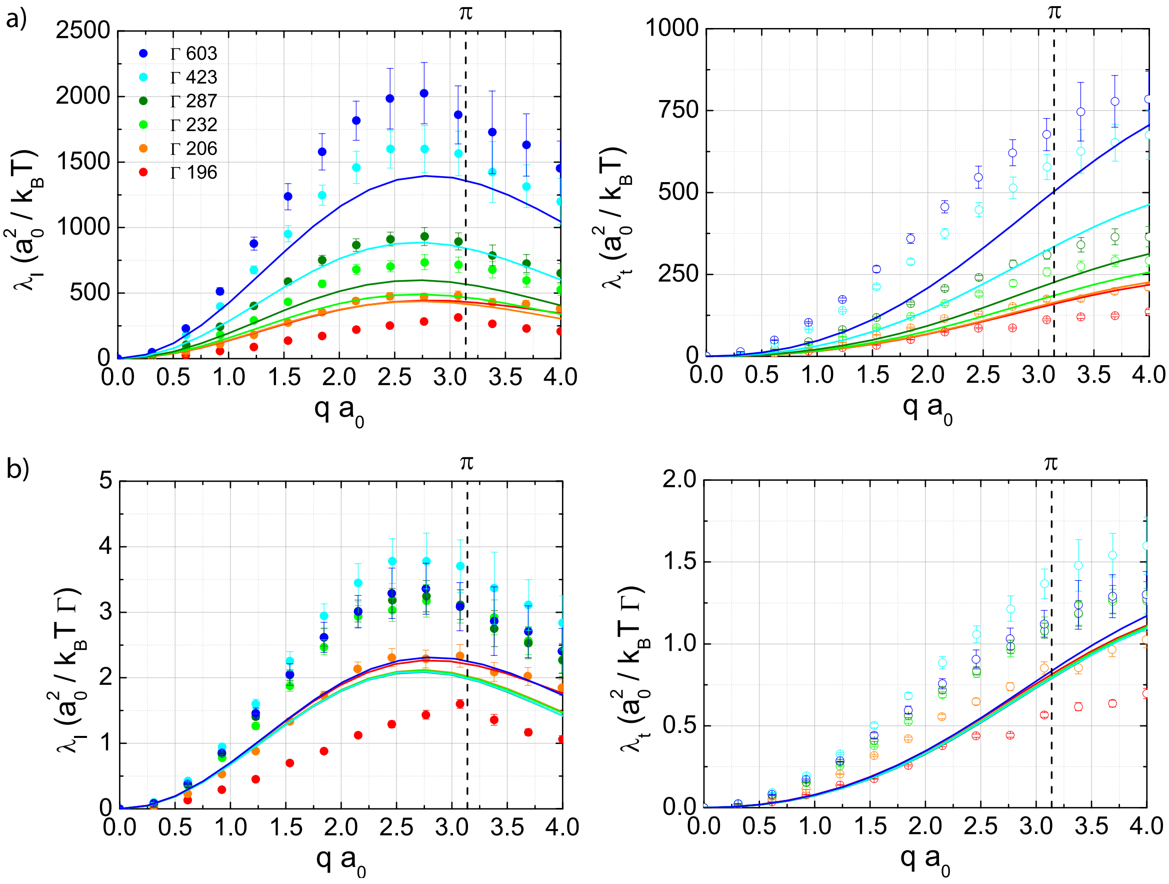

Figure 3.2.: **Dispersion relation of an amorphous system.**
a) Longitudinal (filled circles, left graph) and transverse (empty circles, right graph) dispersion bands in an amorphous system, obtained by a Fourier transformation of the displacement field. Solid lines are the results of the direct computation of the dynamical matrix and a subsequent numerical diagonalisation.
b) Normalized versions of the graphs above.
The vertical dashed lines mark the 'quasi Brillouin zone' edge at $qa_0 = \pi$. For details, see text.

between longitudinal λ_l and transverse λ_t phonons, respectively, by regarding only contributions to the vibrational amplitudes parallel or perpendicular to the x-axis. In contrast to the crystalline case, where the symmetry restricts data acquisition to three directions of $\mathbf{q}$ (in two dimensions), the isotropy of the amorphous state allows for an averaging over evenly distributed directions, increasing the statistics significantly. For that reason, the curves appear much smoother than for lattice data (compare figure 3.1). In agreement with the Debye model[1], the dispersion relations initial growth is

quadratic. This is a manifestation of the perfect plane wave nature for those long wavelengths. Details can be found in section 4.1. For larger wave vectors, the curves deviate from this model towards smaller λ_s, until they reach a maximum in the vicinity of $qa_0 = \pi$. In contrast to crystals, disordered solids exhibit no symmetry points in reciprocal space. The only fixture of a lengthscale may be provided by the mean interparticle distance a_0. It can be approximated from a Voronoi construction, where v_0 is the unit volume determined by the mean Voronoi cell size. The unit volume in two dimensions then becomes $v_0 = a_0^2$ (compare section 2.1.1). The length a_0 manifests itself as a circle with diameter $2\pi/a_0$ in reciprocal space. Thus, this region is defined as a 'quasi Brillouin zone' in the system. It is indicated in figure 3.2 as a dashed black vertical line. Accordingly, it is this particular wave vector where the measured excitations become localized. The growing maximum represents increasing spring constants λ_s and mirrors the increasing rigidity upon the decrease in temperature.
Because of the lacking periodicity, there exist no higher Brillouin zones which could be folded onto the range $-\pi < qa_0 < \pi$. Rather, beyond the quasi Brillouin zone edge at π, the curves exhibit a damped periodic behavior (not shown here). This is a direct consequence of spatial disorder and yields information about the lengthscale of short range order, similar to a structure factor.

Since the method described in section 3.1.1 relies on the assumption of plane waves, the interpretation of data in the vicinity of the Brillouin zone edge should be regarded with caution. At this point in reciprocal space, excitations exhibit a short wavelength which is more likely to be perturbed and scattered by the spatial disorder of the system. Several works dealt with the question of how acoustic phonon waves propagate in disordered materials [Cou03, Léo11a, Ruf03, Ruf06]. The influence of non-isotropy on short lengthscales destroys any well-defined polarisation, thus hampering the technique applied here. For instance, in atomic and molecular glasses, recent work showed that long wavelength modes undergo a crossover from propagation to localisation due to diffraction upon decreasing the wavelength [All99, Haf83]. Also, in colloidal systems, a disordered 'swirling' type of motion for vibrational excitations was claimed to be found [Gho10, Kay10, Che10]. This topic is discussed in section 4.2, where this kind of behavior of low frequency/low wavelength modes is proven to be different in the system studied here. Accordingly, in agreement with classical continuum elasticity theory [Lan95], for small $\mathbf{q}$ the plane wave approximation holds, as the system is considered a homogeneous structureless solid. This is also suggested in other works which claim that continuum elasticity theory can be applied up to a certain characteristic length [Léo06, Léo11a].

---

[1] In the Debye model, a constant sound velocity is assumed, resulting in a linear dispersion $\omega \propto |\mathbf{q}|$. Translated into the spring constants λ_s calculated in this chapter, this corresponds to a quadratic growth.

Having addressed the issue of short wavelength in disordered materials, the focus is now turned back onto the discussion of figure 3.2.a). The solid lines mark the results for the dispersion relations of the direct static approach via the dynamical matrix[2]. The stiffness matrix $\underline{\mathbf{D}}(\mathbf{R})$ as given by equation (3.1) was calculated for the vicinity of ≈ 1800 particles in 100 statistically independent frames, where each frame consisted of averaged positions acquired over a time window of again $18 \cdot 10^3$ seconds. Due to computational limitations, a time coarse graining was applied such that only positional data every 400 seconds was used. Because of the fast decaying $1/r^3$ potential of the magnetic interaction, it was sufficient to incorporate only the next 80 neighbors of each particle (which corresponds to an area with a diameter of $4a_0$). After the Fourier transformation, the data was averaged over all frames and particles, yielding a generalized $\underline{\mathbf{D}}(\mathbf{q})$. The subsequent diagonalisation, however, yields results (solid lines in figure 3.2) which are not in agreement with the data from the 'dynamical' approach of equation (3.5) (symbols in figure 3.2). While there is some consistence in the low q regime, especially for low Γ in the transverse case, the scaling with higher interaction parameters appears very uniform from the static viewpoint in contrast to a more erratic behavior from the displacement field data. This discrepancy is discussed in the next paragraph.

Upon scaling the dispersion bands with the coupling parameter Γ, the curves do not collapse onto a single master curve within the error bounds, as shown in figure 3.2.b) (left and right graph with filled and empty symbols for longitudinal and transverse polarisation, respectively). This feature is surprising at first glance, because the spring constants should directly scale with H^2 and thus go linearly with Γ, as it was shown for crystals [Kei04]. Besides the magnetic field, Γ only depends on intrinsically fixed parameters, determined by the experiment's geometry[3]. However, since the the strength of particle-particle interaction (the spring constant) depends crucially on their respective distance, a subtle change in structure might explain the peculiar (non) scaling behavior. While in the crystalline lattice all positions for each and every particle are ultimately defined for all temperatures, the equilibrium positions of particles in a disordered solid are not fixed and may be changing slightly with an increasing interaction potential, mirroring the tendency of the system to minimize the total potential energy. This adaptation of the structure to altered conditions, leading to an adjustment of the average interparticle stiffness, occurs without affecting the fixed area density n but merely by rearrangements. However, it is stressed that this effect

---

[2] The connotations 'static' and 'dynamic' concerning the possible approaches towards dispersion data correspond to the fact that in the former case, only averaged particle positions are required (which coincide with the equilibrium lattice positions in the crystalline case), while the latter case relies upon information encoded in the displacement field generated by vibrational dynamics of the system.

[3] In fact, it is mostly chemistry involved in either sample preparation or material properties which determines fixed values for mixing ratio ξ, sample area density n or susceptibility χ.

is very subtle, such that curves once moderately deep in the glass ($\Gamma \geq 232$) show overlapping error bars. The phenomenon is much more pronounced in the vicinity of the glass transition, where particles are still more mobile to explore their vicinity (for details on how the interaction parameter is related to the different states, see section 3.2.2). In this, a similarity to the structure factor can be found. This quantity is also known to change very slightly with temperature in disordered states [Ben84].

This effect caused by a subtle structural feature also sheds some light on the discrepancy between the curves obtained by displacement field analysis (symbols) and dynamical matrix diagonalisation (solid lines). In the latter case, the data collapses for the most part even in the vicinity of the glass transition temperature around $\Gamma = 185$. In the fluid, transverse modes can no longer propagate because of the lacking shear response. Hence, at least transverse excitations ('shear waves') should show precursors of the immanent breakdown. Thus, it can be inferred that the amplitude of these curves is solely governed by the strength of the applied magnetic field (compare also graph a). Because this method relies on averaged structural information (the computation in the glassy state is identical with that in the crystalline state, as described in section 3.1.2, last paragraph), the subtle structural rearrangements apparent from the displacement field analysis are not picked up here. Instead, only the overall static structure is considered, which does not differ in the fluid and arrested state.
These results suggest that the dynamical matrix may not be generalized in amorphous solids. Because the local structure is disordered, there is no way to predict the propagation of excitations over larger lengthscales from (averaged) information obtained at short range. This is in contrast to crystalline systems, where the regular local arrangement of particles governs even the long range vibrational properties. For that reason, the green curve from the static approach in figure 3.1.a) fits the data so well while it does not for structural disorder.

3.2. Elastic constants

3.2.1. Elasticity theory

The strain tensor describes the impact of deformation of an isotropic macroscopic body on a microscopic scale [Lan95]. The lateral transformation of the unit length in the system and can be written as

$$u_{\mu\nu} \approx \frac{1}{2}\left(\frac{\partial u_\mu}{\partial x_\nu} + \frac{\partial u_\nu}{\partial x_\mu}\right) .$$

With this, the free energy of a deformed system may be described by

$$\begin{aligned} F &= \frac{1}{2} \sum_{\mathbf{q},\mu,\nu,\sigma,\tau} u^*_{\mu\nu}(\mathbf{q}) C_{\mu\nu\sigma\tau} u_{\sigma\tau}(\mathbf{q}) \\ &= \frac{1}{2} \sum_{\mathbf{q},\nu,\tau} u^*_{\nu}(\mathbf{q}) K_{\nu\tau} u_{\tau}(\mathbf{q}) \,, \end{aligned}$$

where $K_{\nu\tau} = C_{\mu\nu\sigma\tau} q_\mu q_\sigma$ and $C_{\mu\nu\sigma\tau} = \lambda \delta_{\mu\nu}\delta_{\sigma\tau} + \mu(\delta_{\mu\sigma}\delta_{\nu\tau} + \delta_{\mu\tau}\delta_{\nu\sigma})$ is the elasticity tensor. The quantities λ and μ are called Lamé-coefficients. They represent the only non-vanishing components of the elasticity tensor in highly symmetric crystals[4]. It is now possible to use the Fourier transformed displacement field $\mathbf{u}(\mathbf{q})$ to compute the elastic properties of the system. Using the equipartition theorem, one obtains the formula

$$\langle u_\nu(\mathbf{q}) u_\tau(-\mathbf{q}) \rangle = k_B T K^{-1}_{\nu\tau}(\mathbf{q}) \,. \tag{3.6}$$

With this, a formula is derived which works qualitatively like formula (3.5). The dynamical matrix $\underline{\mathbf{D}}(\mathbf{q})$, which describes local bonding properties, is replaced by a modified elasticity tensor $\underline{\mathbf{K}}(\mathbf{q})$, which describes macroscopic properties under deformation. Since both quantities are governed by the microscopic interactions between the building blocks of the studied solid, it is not surprising that both can be connected to the displacement field which mirrors these interactions.

In two dimensions, $\lambda + \mu$ gives the bulk modulus whereas μ gives the shear modulus. By choosing the subscripts ν, τ in equation (3.6) adequately, one obtains two equations which connect the elastic constants directly to the displacement field [vG04]:

$$\frac{a_0^2(2\mu + \lambda)}{k_B T} = \lim_{\mathbf{q}\to 0} \frac{1}{q^2 \langle |u_\parallel(\mathbf{q})|^2 \rangle} \,, \tag{3.7}$$

$$\frac{a_0^2 \mu}{k_B T} = \lim_{\mathbf{q}\to 0} \frac{1}{q^2 \langle |u_\perp(\mathbf{q})|^2 \rangle} \,. \tag{3.8}$$

Since elasticity theory is a continuum theory, both equations are only valid in the limit $\mathbf{q} \to 0$. The meaning behind the above formulas is illustrated well by interpreting $\mathbf{q} = 0$ as a plane wave with infinite wavelength. Hence, the corresponding excitation becomes a macroscopic translation because all oscillators are displaced simultaneously. Thus, such large wave vectors obviously will probe the full macroscopic response. According to their respective geometry, longitudinal modes address the bulk modulus, whereas transverse modes probe the shear modulus.

As the normalized $\langle |u_\parallel(\mathbf{q})|^2 \rangle$ and $\langle |u_\perp(\mathbf{q})|^2 \rangle$ in equation (3.7) and (3.8) offer exactly the eigenvalues $\lambda_l(\mathbf{q})$ and $\lambda_t(\mathbf{q})$ of the dynamical matrix as evaluated in figure 3.2,

---

[4] The only structure more symmetric than a crystal is in fact a disordered system, which may be perceived as a continuum and therefore is perfectly isotropic at sufficiently large lengthscales.

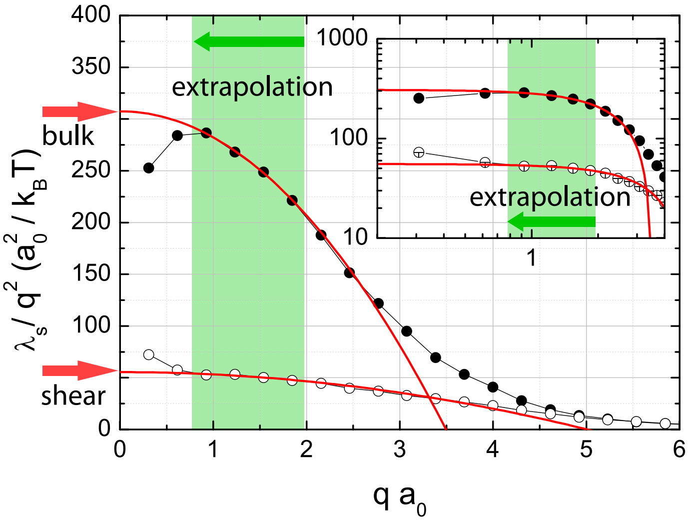

Figure 3.3.: **Extrapolation of dispersion bands at $\Gamma = 423$.**
Elastic moduli are given by the intercept of an extrapolation (indicated by red arrows). The bulk and shear modulus are derived from the longitudinal and transverse dispersion bands (filled and empty black circles), respectively. Green shading marks the region used for linear regression. The inset shows the same plot with logarithmic scaling to highlight the goodness-of-fit in the extrapolation region.

the elastic moduli are obtained by a simple division of these curves with q^2. Because $\lambda \propto |\sin(qa_0)|^2$ [Ash09a] and the expansion

$$\frac{|\sin(x)|^2}{x^2} = 1 - \frac{x^2}{3} + \frac{2x^4}{45} + O(x^6)$$

is quadratic in second order, the intercept of an according regression calculation provides the macroscopic moduli at $\mathbf{q} = 0$. The extrapolation was performed in an intermediate $\mathbf{q}$ regime $(0.8 \leq qa_0 \leq 2.0)$ where the reduced dispersion relations reliably showed a quadratic behavior. Besides higher order terms, deviations from this model may be attributed to finite size effects for very low $\mathbf{q}$, while for high $\mathbf{q}$ around the Brillouin zone edge, the plane wave approximation might not hold. Additionally, due to the discrete nature of particle positions and the finite optical resolution, the dispersion relations are generally subject to increased uncertainty in this region, as already discussed in section 3.1.2.

The extrapolation procedure is demonstrated in figure 3.3. Empty and filled symbols represent transverse and longitudinal data, respectively. The extrapolation is indicated by red solid lines, for which only data in the green shaded region was used. The intercept determining the macroscopic moduli is marked by red arrows. The inset

shows a logarithmic reproduction of the plot, demonstrating the goodness-of-fit in the extrapolation region.
The error of the obtained moduli is composed of the systematic uncertainty in the dispersion relation and the statistical error of the extrapolated intercept. While the latter is directly delivered by the fitting (and is almost negligibly small, see figure 3.3), the former has its origin in the limited resolution of particle positions and can be estimated by an error progression calculation. Some thought has to be put into the handling of systematic uncertainties in the measurements. A derivation of an equation estimating the systematic error in the extrapolation region of the dispersion bands can be found in the appendix (chapter B). Here it is only noted that by measuring a bilinear quantity the error is always positive. Accordingly, the extracted moduli can only be overestimated.

3.2.2. Results

In the following, the system is analyzed with the technique described in the last few paragraphs at different interaction parameters Γ, effectively probing the elastic behavior at different temperatures. Old data acquired by F. Ebert [Ebe08a] indicated a transition temperature of $180 \lesssim \Gamma_G \lesssim 240$. For that reason it was focused on a particularly good temperature resolution in this region. In the end, 30 measurement runs at different temperatures each covering at least $18 \cdot 10^3$ seconds in the ergodic and $36 \cdot 10^3$ seconds in the nonergodic state were performed.

In figure 3.4.a) the evaluated moduli are plotted versus the system parameter Γ. At high temperatures, where the system is still a fluid, the shear modulus (red circles) is zero within the error bounds, regardless of the applied external magnetic field. At $\Gamma \approx 190$, however, it rises from zero to a finite value. From this point on, the system shows a resistance against shear forces - it has become solid. As a guide to the eye, the transition is indicated by the shading in the background, where red implies the ergodic state (high temperatures), while blue indicates the frozen, non-ergodic state (low temperatures). The linear increase in the shear modulus for low temperatures $\Gamma > 200$ illustrates the stiffening of the system upon further cooling. The bulk modulus exhibits the same low temperature behavior. Below $\Gamma \approx 190$, however, it does not drop to zero but remains finite with a constant value because fluids are incompressible.
To investigate the behavior of the shear modulus in more detail, figure 3.4.b) presents a magnified version of graph a). Here, the discontinuous nature of μ at the transition becomes apparent. This is highlighted by the dashed white line.
The width of the 'jump region' is most likely due to the existence of heterogeneous dynamics (compare chapter 5), which are shown to fluctuate in time. For this reason, the interaction parameter is averaged for all contributions to $40 < \mu + \lambda < 150$ and $10 < \mu < 35$, resulting in $\Gamma_G = 197 \pm 5$.

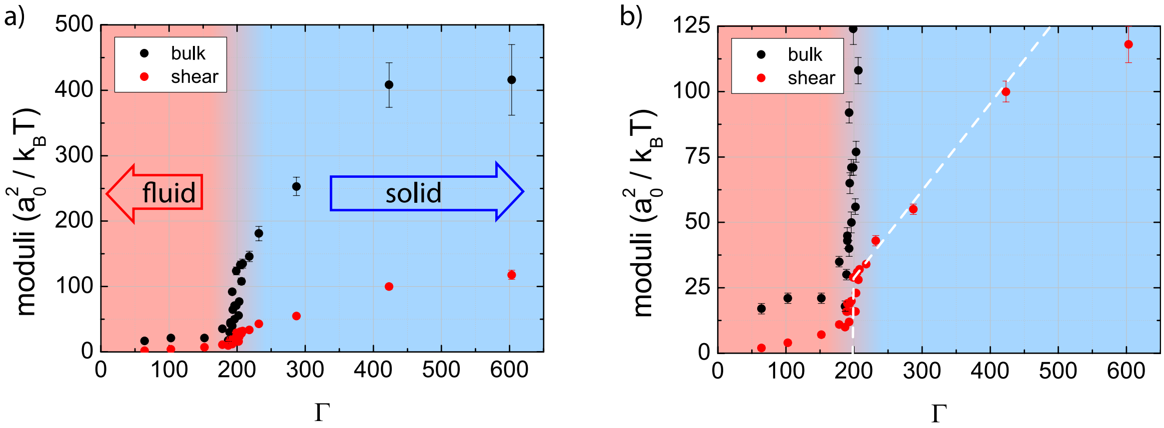

Figure 3.4.: **Temperature dependence of the elastic moduli.**
a) By cooling the system below a temperature corresponding to $\Gamma \approx 190$, a finite shear response is evoked as μ rises from zero to a finite value. The bulk modulus jumps from a constant value in the ergodic and then increases linearly, mirroring the growing rigidity.
b) A zoom on the shear modulus exhibits a discontinuous behavior as well. For decreasing temperature, μ also grows linearly. This is indicated by the white dashed line, which is a guide to the eye.
In both graphs, the background shading indicates the systems state.

With this, the predicted discontinuity of shear elasticity of the glass transition has been backed up by experimental evidence. As stated in the introduction to this chapter, simulation data supports this [Kli12]. In this paper it has also been confirmed that the time evolution of the stress-stress-correlation function,

$$\mathbf{G}(t) = \lim_{\mathbf{q}\to 0} \mathbf{G}_{\mathbf{q}}(t) = \frac{n}{k_B T} \langle \sigma_0(t)^* \sigma_0 \rangle \ ,$$

gives the same results for the shear modulus as the analysis of displacement fluctuations. By this cross-check the results of figure 3.4 are secured. From the cited work, it becomes also possible to comment on the slight rise of μ *before* the transition, which is apparent from graph b). The origin of this behavior is an artifact of the method, which involves measurement times. Depending on the probing time, even fluids exhibit a finite shear resistance[5] [Jeo87]. Thus, the lower the temperature, the longer this measurement time has to be chosen in order to pick up the final decay to zero. Because the instability (drift) of the experimental system in the fluid state, a sufficiently large time window can not be provided. This finite time effect is studied in more detail in the following section.

---

[5] This is impressively illustrated during summer in every open air pool by crying children after accidentally belly-flopping from the three-metre springboard.

3.2.3. Finite time effects

As sketched out in section 2.2.2, a lot of effort is put into the reduction of perturbations of the measurements. Yet, it is impossible to decouple the colloidal ensemble *completely* from the enviroment. These perturbations, like i.e. temperature gradient induced drifts, mechanical vibrations or destabilization due to thermal material expansion, however, will inevitably lead to structural relaxation processes not originally inherent to the system's current state. In two dimensions, there is even another mechanism that will cause increased long-time dynamics. The Mermin-Wagner theorem states that in systems with dimension $d \leq 2$, long-range fluctuations can be created with little energy cost [Mer66, Hoh67]. While these long wavelength perturbations will distort any kinetic measurement on long time scales, they will leave the system unaffected at short timescales. In the following, the influence of these effects on the measured elastic constants is studied by performing time resolved measurements.

By changing the time frame Δt used to determine the equilibrium positions of all particles, different frequency regimes are probed. In figure 3.5.a), the time-dependent behavior of the elastic moduli is shown for the ergodic state with an interaction parameter of $\Gamma = 102$. Short averaging times yield a significant increase in the elastic moduli, reflecting the expected stiffening at high frequencies even for fluids [Jeo87]. For low frequencies (large Δt), however, the shear modulus (red filled symbols) decays to zero within the error bounds. The bulk modulus also decays, although it remains finite. Figure 3.5.b) shows the same for the frozen state at $\Gamma = 287$. For high probing frequencies, elasticity responds similar to the fluid. Larger time windows, however, reveal the distinction between fluid and solid. μ no longer decays to zero but asymptotically saturates into a plateau indicated by a dashed blue line. This marks the macroscopic shear resistance even for times up to 10^5 seconds. The bulk modulus, on the other hand, exhibits only a lesser pronounced, very short plateau and starts to decay again at larger time windows $\Delta t > 2 \cdot 10^4$ s.

The insets of both graphs show the respective high frequency behavior in a logarithmic scaling. The data exhibits some power law signature and may be fitted with exponents $-\frac{1}{3}$ and $-\frac{3}{4}$ for bulk and shear modulus, respectively. The power laws are indicated by the solid blue lines. As of yet, there is no theoretical description for this scaling.

Coming back to perturbations, all of those are likely to reduce the measured moduli, because they decrease the relaxation times. This is commonly observed in mean squared displacements or intermediate scattering functions, where experiments almost always show a slow alpha relaxation process even for the most frustrated systems. With this background, the stability of the measured shear modulus over some orders of magnitude in time apparent from figure 3.5.b) is quite remarkable. The bulk modulus apparently is more sensitive to increased dynamics as it decays again for very long averaging times. This might be a consequence of the small amplitude of longitudinal compression waves. Here, even tiny perturbations tamper with the displacement field,

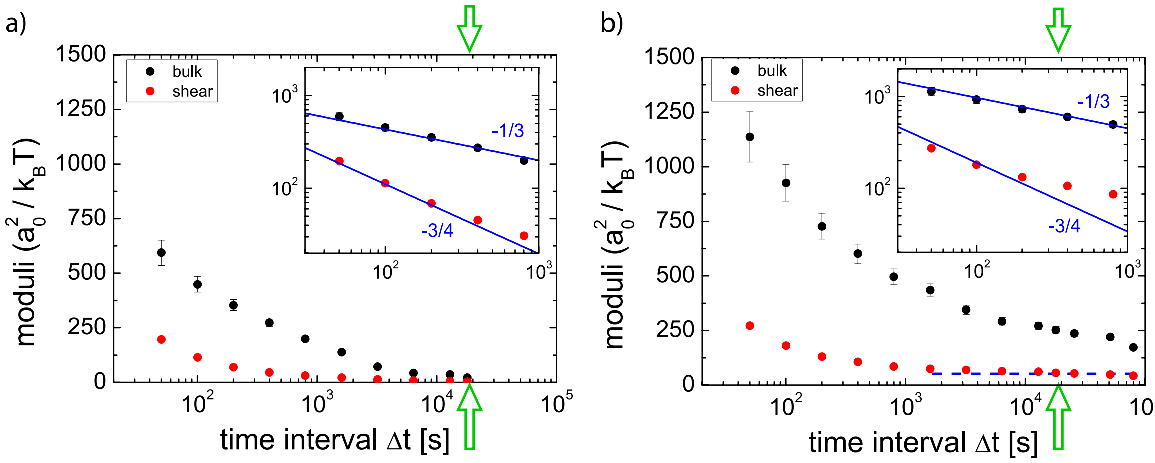

Figure 3.5.: **Finite time effects.**
a) For reduced sampling times in the fluid ($\Gamma = 102$), the expected growth of bulk and shear modulus (black and red symbols, respectively) is observed. For longer time windows, μ decays to zero.
b) The glassy state ($\Gamma = 287$) also exhibits growing moduli for short Δt. For low probing times, however, the shear modulus asymptotically saturates into a plateau, indicated by a blue dashed line.
The green arrows indicate the time window used in section 3.2.2. The insets show the high frequency region with a logarithmic scaling, exhibiting a power law behavior with exponents $-\frac{1}{3}$ and $-\frac{3}{4}$ for bulk and shear modulus, respectively.

leading to distorted wavefronts and hence to the corruption of any derived quantity. In contrast, transverse modes have amplitudes ten times larger, which filters out small dynamical anomalies. This also explains why the error bars for the bulk modulus are larger.

In this context, the discussion of the already mentioned mean squared displacement may offer valuable insight into the dynamics of the system. It is defined as

$$\left\langle \Delta r^2(\tau) \right\rangle = \frac{1}{T} \cdot \sum_{t=1}^{T} \left(\mathbf{r}(t) - \mathbf{r}(t+\tau) \right)^2 ,$$

and its root gives the average distance traveled by a particle after the lag time τ. For very short times, when a particle is supposed to perform ballistic motion, $\langle \Delta r^2(\tau) \rangle$ grows quadratic[6]. This changes to a linear behavior for free diffusion. If the dynamics are obstructed, this decreases further. For the extreme case of full frustration, the

---

[6] This time regime is out of the temporal resolution of the experiment.

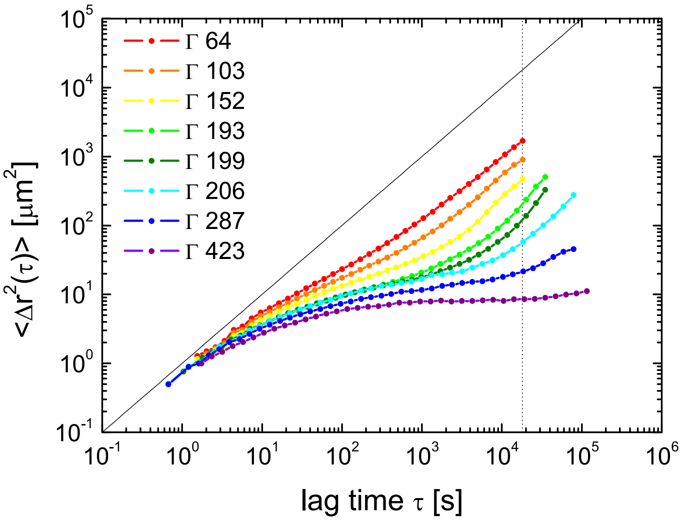

Figure 3.6.: **Mean squared displacement.**
$\langle \Delta r^2(\tau) \rangle$ develops a shoulder upon increasing frustration which slowly crosses over to a plateau. By means of this data, however, it is impossible to distinguish between solid and fluid. The solid black line allows comparison to free diffusion (it has a slope of one). The faint dotted vertical line indicates the size of the time window Δt used to calculate the results of figure 3.4.

mean squared displacement crosses over towards a constant (plateau) value.
Figure 3.6 shows the mean squared displacement for a wide temperature range, starting in the fluid at $\Gamma = 64$ and going up deep into the frozen state to $\Gamma = 423$. In the ergodic state, where particles are free to diffuse, $\langle \Delta r^2(\tau) \rangle$ is almost linear. It exhibits a slight shoulder at $\tau \approx 10^2$ seconds due to the subtle influence of neighboring particles. Upon increasing interactions, the diffusivity is reduced and the shoulder becomes more pronounced. In the glassy state, where the particles are confined to cages consisting of their next neighbors, the shoulder crosses over into a plateau, which opens up again if the cage is broken at very long times. The corresponding timescale is called the alpha relaxation time. It becomes larger and larger the deeper the system is frozen, until for the $\Gamma = 423$ case, it reaches the order of the measurement duration. Comparing those long-time dynamics of the deeply cooled system with the shear modulus in figure 3.5.b) ($\Gamma = 287$), it stands out that the plateau of the latter extends far into the α-regime, where particle rearrangements already induce a significant divergence in the MSD by almost one order of magnitude measured in units of a_0. The bulk modulus, on the other hand, reacts in a similar fashion to the MSD as can be seen by its slight decay for low frequencies. Apparently, the shear modulus is much more insensitive to structural rearrangements which makes it well-suited for studying the glass transition. To ensure that the measured shear modulus in section 3.2.2 is not affected by long-time

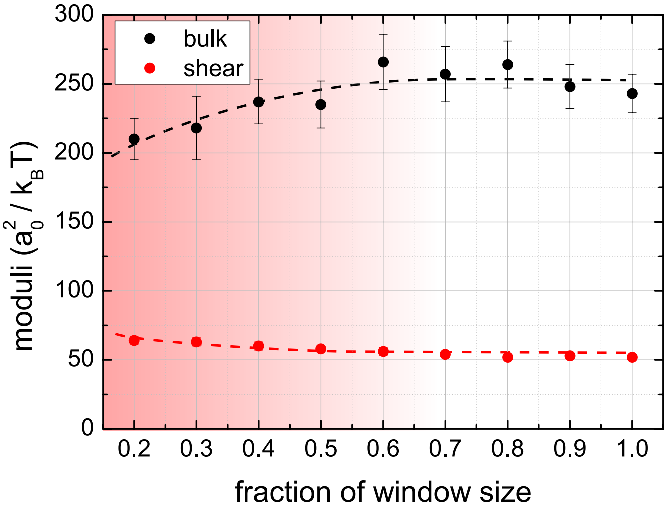

Figure 3.7.: **Finite size effects.**
The abscissa shows the fraction of the original field of view of the system at $\Gamma = 287$ used to compute both bulk- and shear modulus (black and red symbols, respectively). For the original window size, the results have converged towards a constant value. Dashed lines are guides to the eye. The red shading indicates the region with insufficient statistics for reliable error calculation.

dynamics, the length of the time interval is always chosen to be $\Delta t = 18000$ seconds. This is indicated in both figures 3.5 and 3.6 by green arrows on top and bottom and a vertical dotted black line, respectively. This line also separates the plateau of the mean squared displacement from the α-regime for $\Gamma > 230$.

3.2.4. Finite size effects

A restricting element of the method is due to experimental limitations. The finite lateral dimension of the field of view imposes a limit to the resolvable size of excitations. Studying the influence of this constraint is of significant importance, particularly in the case of disordered solids. In this case the underlying medium is not continuous, and elasticity theory is only valid in the long wavelength limit. This directly affects the propagation of plane waves, which remain unperturbed only if the disorder can not be resolved by the wave, i.e. if it has a far smaller lateral dimension than the wave itself. The results presented so far all rely on the validity of elasticity theory, because the Fourier transformation of the displacement field projects plane waves onto the medium. Therefore, the dependence of the acquired elastic constants on the size of the field of view is studied in figure 3.7 for the system at $\Gamma = 287$. Apparently, the bulk modulus (black symbols) is stable within the error band down to half the original

size of the field of view. For even smaller sizes, it starts to decay. The shear modulus (red symbols) extends its continuum value also down to roughly 0.5 before it starts to inflate. The convergence towards constant values for the original size of the field of view is indicated by dashed lines.
For small lateral dimensions, the resolution in reciprocal space starts to become very low, such that only three or two data points fall into the interval $0.8 \leq qa_0 \leq 2.0$. Thus, the extrapolation statistics become extremely sparse. Accordingly, for a window size of 0.3 and below, it is not possible to compute a meaningful error. Also, the extrapolation window had to be enlarged up to $qa_0 = 3$.
From this analysis, the length scale below which vibrational excitations are influenced by the disorder of the propagation medium can be estimated. If the limit is assumed to be 50 % of the original window size (which is 735×735 pixel, $507 \times 507\,\mu\text{m}^2$ or $20.5 \times 20.5\,a_0^2$), this translates into a value of $qa_0 \approx 0.5$ in reciprocal space. Excitations with a wavelength smaller than $\lambda_0 \approx 300\,\mu\text{m}$ are already perturbed by the disorder. The extend of this perturbation, however, remains unclear. The amplitude and smoothness of the dispersion curves in figure 3.2 suggest a weak influence, which only grows in the vicinity to the Brillouin zone edge. This is backed up by the error bars which are still small at $qa_0 \approx 0.5$ but grow into significance above $qa_0 \approx 2.0$, when the perturbations cross over from weak to strong. These findings back up the claim of a ‘continuous colloidal medium’ at length scales of the original field of view.
It is also noted that the inflation of the shear modulus is much less pronounced than the decay of the bulk modulus, i.e. the former is less affected by a finite sized field of view. This can be attributed again to the larger amplitudes of transverse waves, which are in return more insensitive to the microscopic local (dis)order of the medium.

3.2.5. Long time stability

Further, time resolved results of the displacement field analysis of one and the same measurement are studied. This gives a feeling for the reliability of the technique and is another way to access information about the actual accuracy.

For measuring the elastic properties of one state multiple times, very long data sets are necessary in order to preserve good statistics. In the following, the measurement run covered 10^6 seconds (11.5 days) at $\Gamma = 395$. The trajectories were split into ten chunks of equal length. To provide equal statistics in the $\Delta t = 18 \cdot 10^3\,\text{s}$ averaging time window, $90 \cdot 10^3$ seconds where evaluated respectively. In figure 3.8.a), the mean squared displacement is shown for each of those chunks. The plateau value shows almost no variation, indicating equal cage dynamics, i.e. frustration at all times. A slight deviation kicks in in the alpha regime at $\tau > 10^4$ seconds, but is statistically distributed among the measurement time. It is close to diffusive behavior, so this is no aging effect but merely a consequence of the low statistics for those long times where single particles with high dynamics thus might contribute more. Also, effects of the

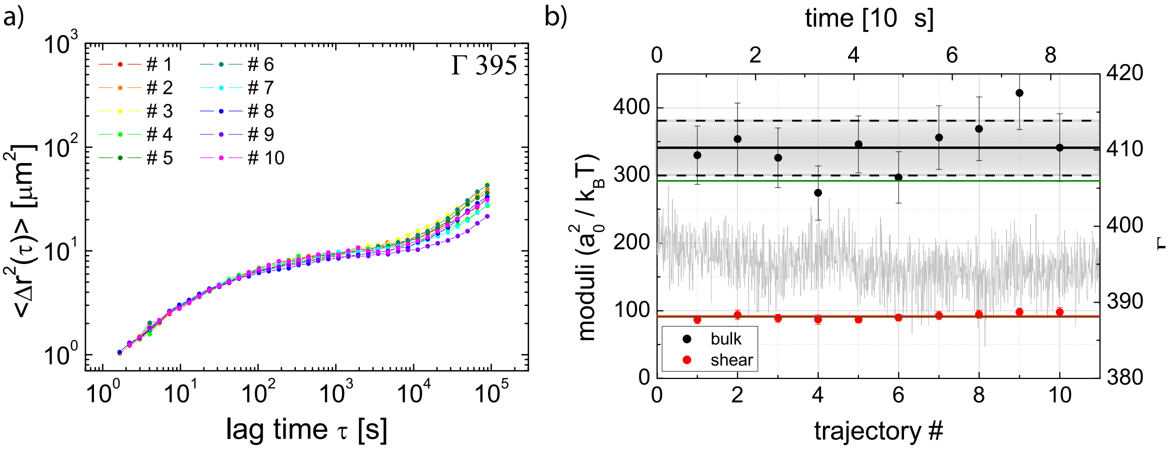

Figure 3.8.: **Temporal stability of the elastic constants.**
a) Mean squared displacement for ten trajectory chunks of a single measurement at $\Gamma = 395$.
b) Time-dependent Bulk and shear modulus (black and red symbols, respectively). The solid horizontal lines indicate the mean of all measurements. While the corresponding error of μ is too small for a reasonable depiction, the standard deviation for the bulk modulus is given as a shaded band around the mean. The green horizontal lines represents the values of the complete measurement. The right axis gives $\Gamma(t)$ which is indicated by the faint gray ‘noisy’ line.

Mermin-Wagner fluctuations might play a role here. It is also noteworthy that even at 10^5 seconds in the alpha regime, the value for $\langle r^2(\tau)\rangle$ has not exceeded $60\,\mu\mathrm{m}^2$, which corresponds to a length of only 0.4 interparticle distances.

In figure 3.8.b), the results of the elasticity of every trajectory chunk are shown. The bulk modulus (black circles) fluctuates around a mean value, indicated by the solid black horizontal line. This value is higher then the single result obtained by calculating $\mu + \lambda$ for the whole undivided trajectory, indicated by a solid green horizontal line, by roughly 14 %. This is comparable to the respective error. The mean lies within the error of each data point. Likewise, the standard deviation of the mean, indicated by the gray shaded band bordered by dashed black lines, covers each data point, with a two exceptions at $\approx 3.1 \cdot 10^5$ and $\approx 7.5 \cdot 10^5$ seconds.

The shear modulus (red symbols) also fluctuates slightly around a mean value, indicated by the red solid horizontal line. Here, the mean is also captured by the individual error bands and only marginally deviates from the single value of the full data analysis. The standard deviation for the mean is not indicated because it is too small at the given resolution.

To prove that the fluctuations of elasticity are inherent to the dynamical fluctuations of the system (compare also chapter 5 on dynamical heterogeneities), the time-dependent

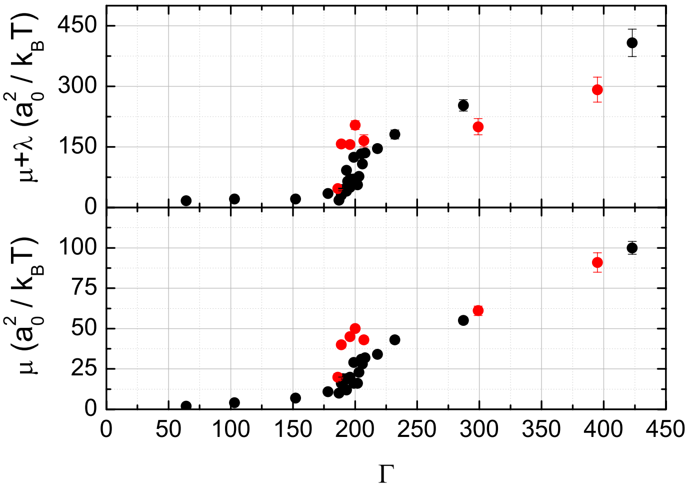

Figure 3.9.: **Hysteresis of the elastic moduli.**
Top and bottom graph show bulk and shear modulus, respectively. Black symbols denote comparatively short measurements ($18 \cdot 10^3\,\mathrm{s} - 126 \cdot 10^3\,\mathrm{s}$) upon cooling. Red symbols identify a heating cycle with long measurements (each $10^6\,\mathrm{s}$). Apparently, the shear modulus remains finite towards higher temperatures (lower Γ).

interaction parameter $\Gamma(t)$ is also given by the faint gray ‘noisy’ line. Its value at time t (top axis) can be read from the right axis. Fluctuating around $\Gamma = 395$ (mainly due to number fluctuations), it apparently shows no correlation in time with the measured elastic constants, therefore decoupling $\mu + \lambda$ and μ from any external quantity.

These results prove the long-time stability of the elastic constants within the calculated error bars. Neither the results for the mean squared displacements nor bulk and shear modulus hint towards any form of aging on the timescale studied here since the system was well equilibrated (typically 24 hours before data acquisition). Because all temperature (magnetic field) changes were performed in rather small steps, the system could always considered being an ‘aged’ glass.
The results also highlight the stability of the shear modulus, which exhibits significantly reduced fluctuations once more. Again, this is attributed to the disparate sensitivities of longitudinal and transverse plane waves to distortions of their wavefronts.

3.2.6. Hysteresis

As a final analysis, the behavior of the elastic moduli at the transition on the dependence of the crossover direction is studied. The results in figure 3.4 were acquired for increasing Γ, i.e. cooling. In figure 3.9, the same results are plotted again in black for bulk and shear modulus in top and bottom graph, respectively. Because of large dynamics in the ergodic state and initial low resistance against drift, measurements were limited to comparatively short times ($18 \cdot 10^3\,\mathrm{s} - 126 \cdot 10^3\,\mathrm{s}$). Once deep in the nonergodic state, the system could be stabilized further which enabled measurement times of 10^6 seconds ($\approx$ 12 days). Those are indicated for decreasing Γ (increasing temperature) as red symbols. Over a large temperature range down to $\Gamma = 300$, both directions result in similar values for the elastic moduli within the error bars. In the transition region around $\Gamma \approx 197$, however, the red symbols still unambiguously indicate a solid state, while the red symbols fluctuate rather strongly. Only at $\Gamma = 186$ the former eventually starts to drop. Although not rigorous poof, these results point towards a hysteresis in the glass transition temperature which stresses the history dependence of these systems. Additional temperature cycles would be necessary to back up these findings[7].

In the following chapters, where evaluation methods demand large statistics or extended time information, the data from the heating cycle is used unless stated otherwise. This implies a transition temperature of $\Gamma \approx 186$.

---

[7] The heating process and the respective long-time measurements repeatedly suffered from several interruptions due to external construction work on the university campus. Measurements below $\Gamma = 186$ could not be performed because the experiment crashed eventually and during the following month the system could not be stabilized again.

4. Density of states

The theoretical considerations of the preceding chapter have demonstrated that vibrational properties of periodic systems are well understood. Their excitations can be regarded as plane-wave phonon modes which propagate unperturbed along a crystal's symmetry axes. In the case of finite systems, the corresponding wave vectors are quantized. It is, however, a completely different matter with amorphous systems. At some point the wavelength becomes similar to the scale of disorder and excitations cannot propagate unperturbed any longer. The continuous scattering leads to a loss of defined polarization and makes these modes hard to describe.

For that reason, amorphous materials exhibit a set of peculiar features which distinguishes them from their crystalline counterparts [Phi81]. In atomic or molecular systems like oxide semiconductors, metallic glasses or organic polymers these phenomena are well documented. The most often stated of these universal anomalies is a peak in the temperature dependence of the reduced specific heat C_p/T^3 at low temperatures (around $10-30\,\mathrm{K}$). Also at those temperatures, disordered solids exhibit a plateau in the thermal conductivity. For even lower temperatures $T < 1\,\mathrm{K}$, a linear increase in specific heat is found in contrast to the expected T^3 prediction by the Debye model. There is consensus that many of these features are connected to the anomalous excess of low frequency excitations over the Debye prediction, measured by inelastic Raman or neutron scattering [Kri53, Mal86, Buc86, Sok95, Ruf06] in various materials as polymer glasses [Duv03], silica [Duv04] or metallic glasses [Ara99]. The vibrational density of states runs through a maximum if scaled by the angular frequency ω, which is called the 'boson peak'. This is one key feature of disordered solids and believed to explain their odd low temperature behavior. Much work has been put into clarifying the role and origin of the boson peak [Phi81, Ang95, Mal86, And95], but there still exists no unifying model. While some facts appear well backed up by simulations and experiments, others are still subject to debate. For example, it is well known that the boson beak comprises mainly of transverse excitations [Win75, Shi08]. However, attempts to associate the boson peak frequency with some other prominent features, for example the Ioffe-Regel[1] limit, have led to ambivalent results [Ruf06, Sco06, Shi08]. As well, it is not yet clear whether the boson peak is of an acoustic or non-acoustic nature [Dov97, Ruf08].

It has been only recently that vibrational properties of glasses have come into focus

---

[1] The Ioffe-Regel limit marks the wavelength of phonons which corresponds to their mean free path. I.e. excitations with shorter wavelength are constantly scattered and propagate only in a diffusion-like fashion.

of colloidal soft matter research. Taking advantage of well controlled and understood mechanics, the boson peak has been connected to structural features in these systems by both experiments [Tan12a] and simulation [Shi08]. Other work could identify excess vibrations with soft modes [Che10] and associate their localisation to particle rearrangements [Che11].
Much of this recent research is based on a method known as *principal component analysis* (PCA) [Dun89]. Although the principles are known since the dawn of the last century [Pea01], it has been put to use in colloidal physics only very recently [Gho10, Che10, Kay10]. It evolves around finding large eigenvalues and corresponding eigenvectors of the correlation matrix of the system's displacement field. Those covariance-like eigenvalues represent the principal components of the system and provide the number of excitations.

In the following section, a short revision of the vibrational properties of idealized solids is given. The next section introduces principal component analysis. A more detailed and very intuitive description of this technique can be found in [Shl09]. Further, the application to colloidal systems is studied, followed by the presentation of results. Then, an alternative approach for obtaining the spectrum of vibrational excitations is discussed, followed again by results. Finally, the emerging picture is discussed.

4.1. Debye model

Owned to the nature of the experiment (section 2.2.2), only the two-dimensional case is discussed. In this system, a number of N^2 oscillators are considered. They sit on a quadratic lattice inside a square box with length L and periodic boundary conditions. The wave vector $\mathbf{q}$ of excitations is then restricted to specific values:

$$q_x, q_y = 0, \pm 1 \cdot \frac{2\pi}{L}, \pm 2 \cdot \frac{2\pi}{L}, \ldots, \pm N \cdot \frac{2\pi}{L}\,.$$

In q-space, the smallest resolvable distance is $2\pi/L$. Therefore the unit area is $4\pi^2/L^2$, and there is exactly one permitted value of q in this unit area. Accordingly, a circle with radius q in q-space covers

$$n = \frac{\pi q^2}{\left(\frac{2\pi}{L}\right)^2} = \frac{L^2}{4\pi} q^2$$

$\mathbf{q}$ vectors. The density of states is defined as the number of modes n per frequency, that is with neglecting any directional dependence

$$D(\omega) = \frac{\mathrm{d}n}{\mathrm{d}\omega} = \frac{\mathrm{d}n}{\mathrm{d}q}\frac{\mathrm{d}q}{\mathrm{d}\omega} = \frac{\mathrm{d}n}{\mathrm{d}q}(\nabla_q \omega)^{-1} = \frac{L^2}{2\pi}\frac{q}{\nabla_q \omega}\,. \tag{4.1}$$

Here, q is of course a function of omega - the inverse function of the dispersion relation. $v_g(q) = \nabla_q \omega$ is the sound (group) velocity and can be calculated from the dispersion relation $\omega(q)$. In the Debye model, the sound velocity is assumed to be constant such that $\omega = v_D \cdot q$, which is a reasonable assumption in a homogenous, continuous medium. v_D is the Debye-velocity and determined by $1/v_D^2 = 1/v_\perp^2 + 1/v_\parallel^2$, the sound velocities perpendicular and parallel to the direction of propagation, respectively. Hence, in this model the density of states takes the form

$$D(\omega) = L^2\omega/2\pi v_D^2 \,. \tag{4.2}$$

Note that in two dimensions, $D(\omega)$ is linear in ω for low frequencies. This remarkable feature is called 'Debye behavior'.

4.2. Principal component analysis

Principal component analysis is used to structure, simplify and illustrate complicated sets of data. This is achieved by expressing multiple statistical variables through less, yet significant linear combinations (*principal components*). Application yields data free of noise and redundant information and reveals otherwise 'hidden' features.

The mathematical approach is based on finding a better basis for the original data:

$$\underline{\mathbf{P}\mathbf{X}} = \begin{pmatrix} \mathbf{p}_1 \\ \vdots \\ \mathbf{p}_m \end{pmatrix} \cdot \begin{pmatrix} \mathbf{x}_1 \cdots \mathbf{x}_n \end{pmatrix} = \begin{pmatrix} \mathbf{p}_1 \cdot \mathbf{x}_1 & \cdots & \mathbf{p}_1 \cdot \mathbf{x}_n \\ \vdots & \ddots & \vdots \\ \mathbf{p}_m \cdot \mathbf{x}_1 & \cdots & \mathbf{p}_m \cdot \mathbf{x}_n \end{pmatrix} = \underline{\mathbf{Y}} \,,$$

where $\underline{\mathbf{P}}$ is a transformation matrix, consisting of the set of m new basis vectors $\{\mathbf{p}_1, \ldots, \mathbf{p}_m\}$ for expressing the columns $\{\mathbf{x}_1, \ldots, \mathbf{x}_n\}$ of the original data set $\underline{\mathbf{X}}$[2]. In other words, the rows of $\underline{\mathbf{P}}$ will become the principal components of $\underline{\mathbf{X}}$. They are chosen with the intention of reducing redundancy and noise in $\underline{\mathbf{X}}$.
This is motivated by recognizing the dimension with the highest signal-to-noise ratio $SNR = \sigma^2_{\text{signal}}/\sigma^2_{\text{noise}}$, i.e. largest variance σ, as a natural basis for $\underline{\mathbf{X}}$ (supposing that the data quality is good, i.e. $\sigma^2_{\text{signal}} \gg \sigma^2_{\text{noise}}$). In other words, the direction in which the variance is large indicates a direction in which a variable in the data set is physically 'changing' (fluctuating). This can be checked for all dimensions of the data simultaneously by defining their covariance matrix:

$$\underline{\mathbf{C}}_X := \frac{1}{n}\underline{\mathbf{X}\mathbf{X}}^T \,.$$

---

[2] Each column vector $\mathbf{x}_i$ with $i = 1, \ldots, n$ represents one complete measurement of all m variables (it therefore consists of m components). The set $\underline{\mathbf{X}}$ contains *all* samples of these variables. That means each row of $\underline{\mathbf{X}}$ has n entries (for n samples) and represents the measurement of one variable, called a *measurement type*. Therefore, $\underline{\mathbf{X}}$ is the data set containing *every* information available.

It operates as the central quantity in PCA. It contains the variance $\sigma^2_{\mathbf{x}_i} = \frac{1}{n}\sum_k (x^i_k)^2$ of the ith row (the ith measurement type) of $\underline{\mathbf{X}}$ in its diagonal terms, and the covariance $\sigma^2_{\mathbf{x}_i\mathbf{x}_j} = \frac{1}{n}\sum_k (x^i_k)(x^j_k)$ between measurement types i and j in its off-diagonal terms. The absolute magnitude of the covariance is a measure of redundancy, because it is large when data is correlated (correlation of measurement types means redundancy, because they 'measure the same'), and likewise small if data is uncorrelated. Hence it is the goal to maximise the signal and eliminate redundancy by transforming $\underline{\mathbf{C}}_X$ into a form $\underline{\mathbf{C}}_Y$ where all off-diagonal elements become zero. It can be shown that the transformation matrix for this operation is the exact same matrix that converts $\underline{\mathbf{X}}$ into $\underline{\mathbf{Y}}$, i.e. it is obtained $\underline{\mathbf{C}}_Y = \underline{\mathbf{P}}\underline{\mathbf{C}}_X\underline{\mathbf{P}}^T$. Furthermore, a matrix is diagonal in the basis of its own eigenvectors, i.e. the eigenvectors of $\underline{\mathbf{C}}_X$ are the wanted principal components of the original data $\underline{\mathbf{X}}$.

Ghosh *et al.*, Chen *et al.* and Kaya *et al.* have shown that this can be applied to video microscopy data of colloidal systems [Gho10, Che10, Kay10]. The goal is to filter out correlated vibrations of particles hidden amidst their Brownian motion. To describe their amplitudes, the displacement field $\mathbf{u}$ is calculated from some intermediate 'equilibrium positions' $\mathbf{R}$ (see section 3.1.1). Now the covariance matrix $\underline{\mathbf{C}}$ is given by

$$C_{ij} = \langle u_i(t) u_j(t) \rangle \ , \tag{4.3}$$

where the average $\langle \ldots \rangle$ is taken over all sampled times. $u_i(t)$ is the displacement of particle i at time t, i.e. the matrix is of size $2N \times 2N$ (where N is the number of particles) and takes the form

$$C_{ij}(t) = \begin{pmatrix} u^x_1 u^x_1 & u^y_1 u^x_1 & u^x_1 u^x_2 & u^y_1 u^x_2 & \cdots \\ u^x_1 u^y_1 & u^y_1 u^y_1 & u^x_1 u^y_2 & u^y_1 u^y_2 & \cdots \\ u^x_2 u^x_1 & u^y_2 u^x_1 & u^x_2 u^x_2 & u^y_2 u^x_2 & \cdots \\ u^x_2 u^y_1 & u^y_2 u^y_1 & u^x_2 u^y_2 & u^y_2 u^y_2 & \cdots \\ \vdots & \vdots & \vdots & \vdots & \ddots \end{pmatrix} .$$

Large eigenvalues λ^* of this matrix indicate correlated displacement involving a large number of particles. The corresponding eigenvectors are the principal components of the system and illustrate that correlation spatially. Henkes *et al.* [Hen12] have shown that $\underline{\mathbf{C}}$ is related to the dynamical matrix $\underline{\mathbf{D}}$ by the relation

$$D_{ij} = \frac{K_{ij}}{m_i} = k_B T \frac{(C^{-1})_{ij}}{m_i} \ ,$$

where K_{ij} is the so-called stiffness matrix and m_i the mass of particle i. As such, the eigenvalues of C_{ij} are interpreted as the inverse of the frequencies of modes in the system:

$$\omega \propto \sqrt{\frac{1}{\lambda^*}} \ . \tag{4.4}$$

Here, it is worth pointing out that since the elements of C_{ij} are a product of two length, the frequencies as computed in the last equation will have 1/m as their unit. The corresponding eigenvectors represent the 'amplitudes' of the modes but cannot be connected to a wavelength. In other words, this state of the covariance matrix will only give information about mode shape and the associated weighting of contribution to the whole spectrum. Because so far only spatial but no temporal information is incorporated into the covariance matrix, no prediction on *real* (angular) frequencies can be made, which is a major drawback. That is why the inverse of the eigenvalues can only be *interpreted* as something like frequencies, assuming a (yet unknown) dispersion relation to exist.

Further, this relation is only valid for virtual particles in a 'shadow system'. It is constructed from the same configuration of the colloids with the same interactions, but neglects the damping of the surrounding fluid. The extracted modes therefore only describe some kind of instantaneous momentum of the real system.

4.2.1. Results

Application of PCA

As a first approach towards the application of principal component analysis, it is instructive to study the spectrum of eigenvalues of the covariance matrix. Figure 4.1.a) shows data from a system at $\Gamma = 200$, thus a little bit below the glass transition temperature at $\Gamma \approx 186$[3], where eigenvalues are sorted by decreasing numerical value (indexed by the 'mode number' m). Different colors correspond to finite measurement times which is discussed in more detail below. The corresponding covariance matrix contains entries from more than 2250 particles, providing sufficient statistics. Starting at very large values for the first few diagonal elements of the covariance matrix, the spectrum drops very fast (consider the logarithmic plot) before gradually turning into a more homogenous distribution close to zero. Because large eigenvalues indicate the most *principal* components, figure 4.1.a) already conveys an important feature of the studied system: The displacement field, which serves as the input for the analysis, can be described to a large extend by only a few basic patterns (these are contained in the eigenvectors which will be discussed later). In other words, if the principal components are interpreted as modes, the system is dominated by only a small number of elementary excitations, because only less than 100 eigenvalues out of more than 4500 have numeric values significantly larger than zero.

As discussed in [Hen12], principal component analysis depends strongly on the available statistics. This is expressed by the quantity $r = 2N/N_\tau$, where N is the number of particles considered (thus showing $2N$ degrees of freedom which also corresponds to the number of modes) and N_τ is the sample number. In figure 4.1, the available

---

[3] Compare section 3.2.6. Throughout this chapter, the data from the heating cycle is used unless explicitly stated.

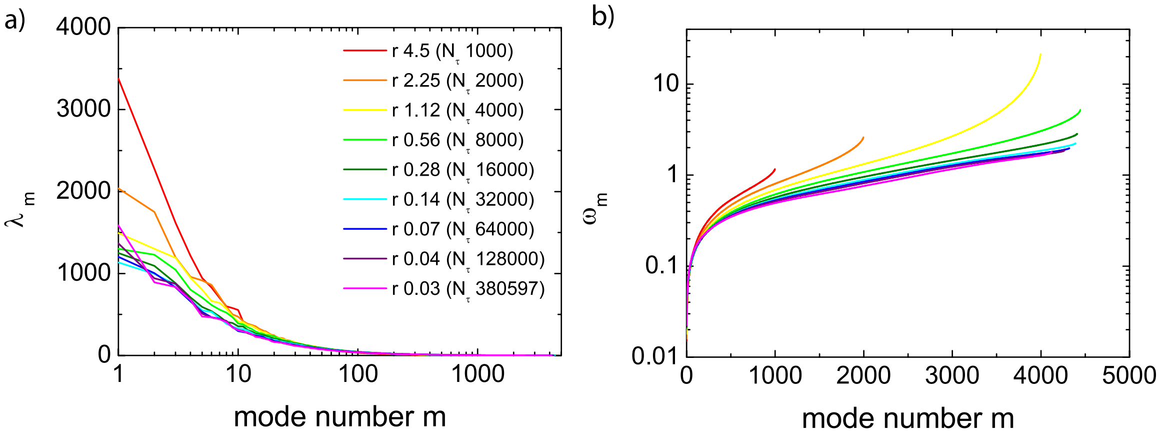

Figure 4.1.: **Spectrum of eigenvalues and corresponding frequencies.**
The legend applies to both graphs.
a) The graph shows the distribution of eigenvalues λ_m^* for different trajectory lengths N_τ. It suggests the dominance of only a few principal components, as it decays rather dramatically over the first couple of eigenvalues (mode numbers) and saturates for trajectories longer than $3.2 \cdot 10^4$ frames.
b) Frequency conversion according to equation (4.4). The dominating eigenvalues translate into low frequency excitations.

trajectories were shortened artificially. It needs large statistics with $r < 0.14$ (this corresponds to $\approx 3.2 \cdot 10^4$ frames) for the spectrum to converge. For larger r, large eigenvalues get overestimated. Although this effect is quite severe, it must not necessarily play a crucial role on the route towards the density of states. This might become more clear in figure 4.1.b), where by equation (4.4) the eigenvalues λ_m^* are assigned to frequencies ω_m. Because the conversion is inverse, the impact of overestimated eigenvalues becomes negligible in the spectrum of frequencies. As a result of this, the curves in graph b) all converge towards small m and ω_m.
On the other hand, insufficient statistics also cause the underestimation of small eigenvalues, leading to a proliferation of high frequency modes (red to green curves). In fact, taking this to an extreme, for $r > 1.0$ the covariance matrix exhibits eigenvalues of zero, resulting in a shortened spectrum (red, orange and yellow curve). However, it should be noted that the corresponding eigenvalues are not amidst the most principal components. Thus, it may be concluded that slowly oscillating, long wavelength excitations govern the vibrational properties of the system, although their number is limited. The proliferation of high frequency modes has little global influence. Here, insufficient statistics would lead to an overestimation of frequencies.

On a side note, the smaller number of eigenvalues found for smaller r up to 0.56

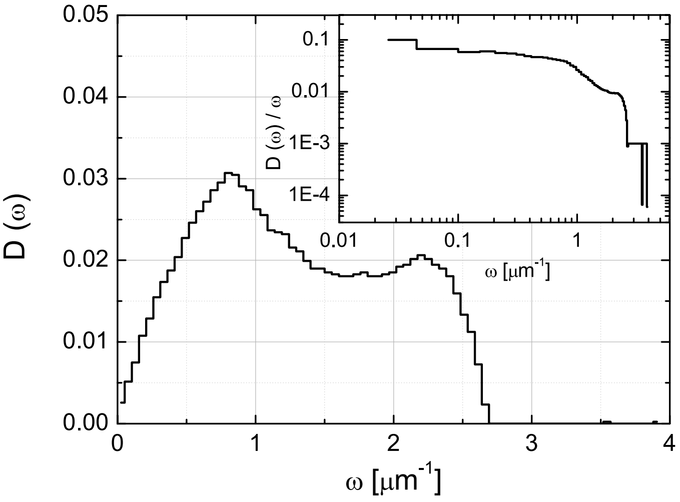

Figure 4.2.: **Density of states.**
DOS of the system at $\Gamma = 200$. The weak double peak structure hints toward Van Hove type singularities. The inset shows the reduced DOS. The plateau at small frequencies suggests Debye behavior.

(barely visible by shortened curves in graph b) is an artifact originating from difficulties to track all particles over such long timescales. If particles are lost, for example because they diffuse out of the field of view, the resulting covariance matrix will be of smaller dimension, yielding a smaller amount of eigenvalues, thus showing a shorter spectrum.

From the spectrum of frequencies, the density of states may be obtained. By binning into a histogram, the slope of figure 4.1.b) determines the number of vibrational states at a given frequency. This is shown in figure 4.2 again for $\Gamma = 200$ with a normalisation to the degrees of freedom $2N$, where the trajectories consisted of $1.28 \cdot 10^5$ frames, corresponding to $r = 0.04$ and covering approximately $T = 4$ days. The time window used to determine the intermediate 'equilibrium' positions was set to $\Delta t = 3600\,\mathrm{s}$, a value below the relaxation time τ_α but well in the plateau exhibited by the mean square displacement. This secures the system is in a metastable state. The binsize was chosen to $\Delta\omega = 0.052\,\mu\mathrm{m}^{-1}$ which smooths figure 4.2 to a reasonable extend. Otherwise, the choice is somewhat arbitrary. Although the influence of $\Delta\omega$ onto the overall shape of the DOS is not severe (for an intermediate binsize), the need to study this aspect remains. This is tackled later in this section as well as in section 4.3.1, where a cumulative quantity much less dependent on the binsize is computed.

The density of states plotted in figure 4.2 emerges from zero and grows almost linearly. This culminates in a pronounced peak at $\approx 0.8\,\mu\mathrm{m}^{-1}$. The subsequent drop wears out into a plateau, terminated by the residual of a second peak at $\approx 2.25\,\mu\text{m}^{-1}$ before dropping rapidly all the way down to zero. Although faint, the distinctive double peak structure in the density of states suggests underlying Van Hove type characteristics, where the singularities originate from the vanishing of group velocity at the Brillouin zone edge of transverse and longitudinal waves, respectively [Hov53]. In order to distinguish between these two types of excitations, however, the corresponding modes need to exhibit plane wave behavior. The shape of the depicted density of states therefore already suggests a strong portion of plane waves in the vibrational spectrum. For these excitations, the system might be treated in the limit of continuum theory. More evidence to that is revealed if the density of states is scaled with the frequency. The inset of figure 4.2 demonstrates the striking linear growth of $D(\omega)$ for small frequencies, which suggests that the Debye picture (in particular equation 4.2) is applicable. In this reduced representation, the second peak of the Van Hove singularities manifests itself as a shoulder, before the number of states becomes zero for high frequencies.

Considering the experimental finite resolution of particle positions, not all data from the covariance matrix might be reliable. Because it comprises of products of length, eigenvalues smaller than the squared smallest resolvable displacement must be subject to noise. Thus, all data above the corresponding frequency may be considered unreliable. With a precision of 0.2 pixel this translates into a critical frequency of $\omega > 7.2\,\mu\text{m}^{-1}$. As evident from figure 4.2, this limit is not reached for the present data.

Statistics and mode structure

The influence of statistics on the eigenvalue spectrum was already discussed in the preceding paragraph and visualized in figure 4.1. Nevertheless, the study of the dependence of the density of states yields even further information.
Figure 4.3.a) shows the results on varying trajectory length, revealing that the number of states initially increases with growing statistics. This is caused by the zero eigenvalues which do not contribute to the histogram at large r. While the frequencies are spread out for short trajectories, they start to concentrate in a region below $3\,\mu\text{m}^{-1}$ as better statistics become available. Note that ‘better’ corresponds to already as much as $5 \cdot 10^4$ samples! It is not until $r = 0.07$ when the distribution develops the second peak and therefore reveals the plane wave dominance. It is noteworthy, however, that at $r = 0.03$ the second peak starts to vanish again. For a trajectory this long (12 days!), the system does not remain in the same metastable state, and particle rearrangements are to be expected. This can be seen in the corresponding mean square displacement (figure 3.6), where at this point the alpha-relaxation has already started. This randomizes the covariance matrix to a certain extend, destroying the underlying long wavelength correlation of plane waves and diminishing the second peak. In

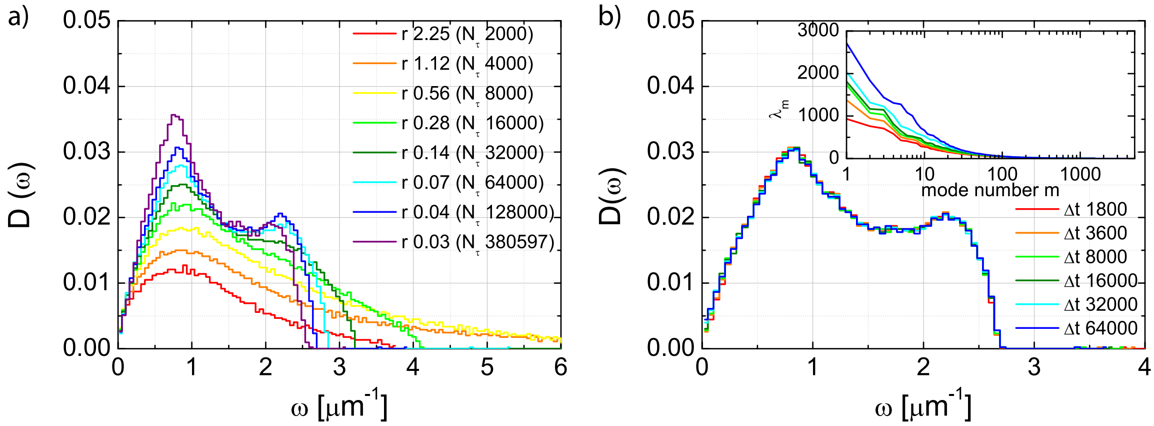

Figure 4.3.: **Density of states for different trajectory lengths and time windows.**

a) Only for long trajectories ($N_\tau > 64000$) the density of states exhibits the double peak structure. For very long times, however, this feature is lost again.

b) Dependence on the choice of the time window Δt for which the intermediate 'equilibrium positions' are determined. The inset shows the spectrum of eigenvalues (compare figure 4.1.a).

contrast, the curve for $r = 0.04$ contains only $1.28 \cdot 10^5$ samples which translates to $3.3 \cdot 10^5$ s. This is just at the onset of the alpha-relaxation, where particles on average have not traversed more than 1/3 of the mean interparticle distance a_0, promoting the restriction of trajectory length to times $T \leq \tau_\alpha$.
Figure 4.3.b) shows the dependence of the density of states on the time interval Δt used to compute the particles intermediate 'equilibrium' position. Apparently the distribution of modes is not affected. This result seems intuitive, because Δt only affects the magnitude of the entries of the covariance matrix. Interestingly though, the corresponding eigenvalue spectrum given in the inset shows a dependence on Δt. However, the lower part of the corresponding frequency spectrum (not shown) remains mostly unaltered, because the conversion is inverse, i.e. the same argument made in the first paragraph of this section holds. As long as all samples (frames) which contribute to the covariance matrix originate from the same metastable state, i.e. are taken from trajectories shorter than the alpha-relaxation, the window size Δt does not matter for determination of the density of states.

Since the eigenvalues of the covariance matrix are only the indicators of the true components, it is instructive to look at the eigenvector structure as well. Figure 4.4.a-e) visualizes the patterns for frequencies $\omega = 0.03, 0.08, 0.19, 0.39, 0.81\,\mu\mathrm{m}^{-1}$, respectively. If the principal components of the displacement field were to be interpreted

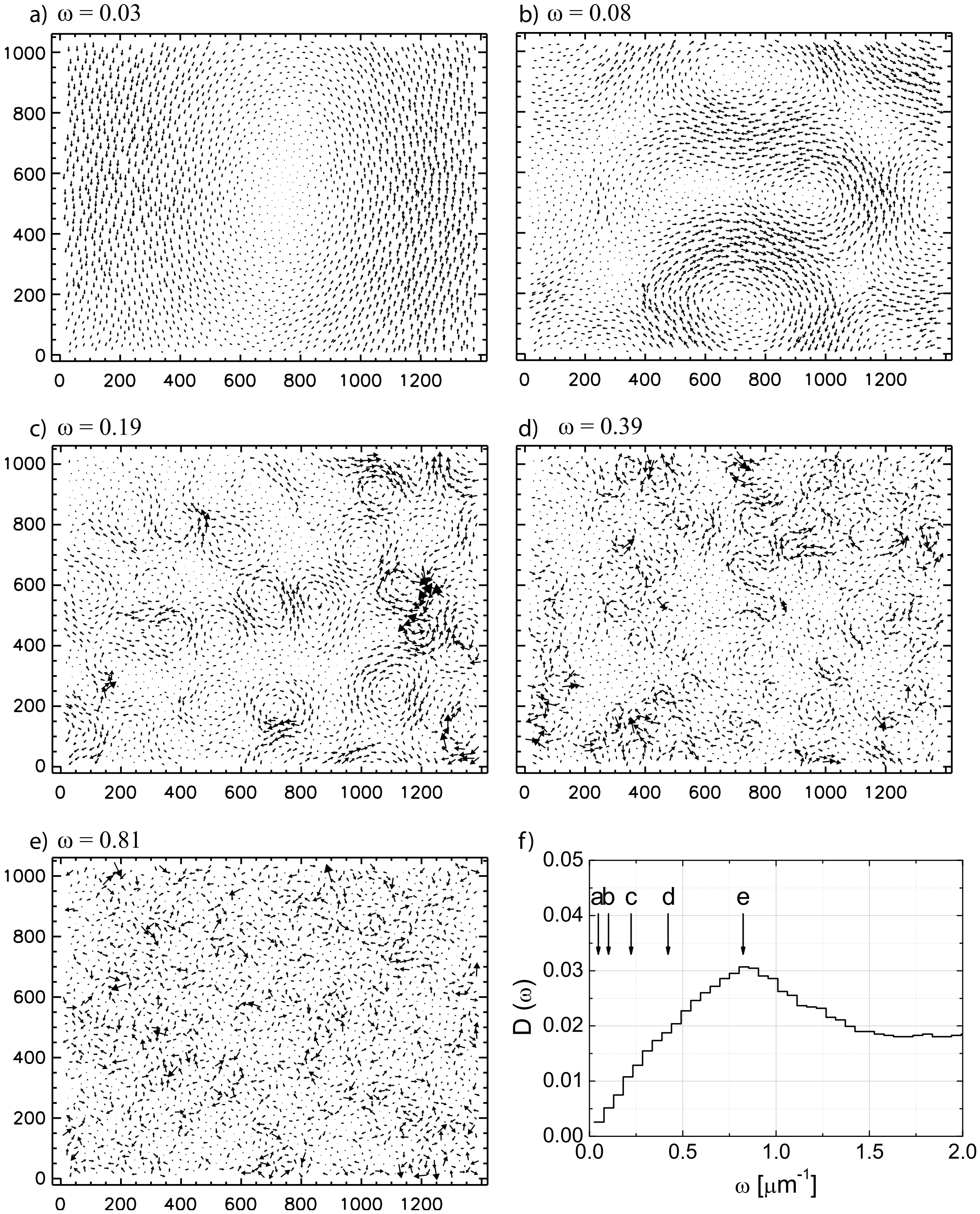

Figure 4.4.: **Structure of the principal components.**
a-e) The eigenmode patterns show decreasing coherence up to the frequency of the first peak.
f) DOS with indication of eigenmode frequencies.

as modes, particles would perform the presented motion in an undamped 'shadow system'. The eigenmode structure yields no surprises and exhibits the expected features: For very low frequency (a-b), motion is largely correlated and homogenous. This represents the behavior of plane waves. The same structure of one large vortex is also typical for crystalline samples [Gho11] indicating that in this particular glassy system at hand low energy excitations can be approximated as plane waves.

For increasing frequency (c-d), the number of vortices grows as their diameter decreases, introducing more and more randomization. The structure also shows features hinting towards slight localisation, indicated by single or clumped up large arrowheads. This is a manifestation of waves scattered by the disorder of the system [Léo11b] and might be connected to the Ioffe-Regel criterion [Shi08]. This type of pattern was also reported in other works. Here, it corresponded to the largest eigenvectors or most principal components [Ash09b, Gho10, Che10, Gho11, Tan12a] and not to intermediate frequencies. This might be a first hint that the softness of the potential present in the experiments conducted in this thesis also allows for much softer modes. Because of their vortex-like appearance, the (abstract) dynamics of these modes was termed 'swirling motion' [Gho10].

Going up to frequencies of modes contributing to the first peak, the coherent character of the components is eventually lost, even on short lengthscales. There appears to be no underlying structure in the excitations, leading to a breakdown of the Debye model (see figure 4.2, inset) from this point on. The patterns can no longer be regarded as principal constituents of the displacement field. Yet, it is these modes that make up the majority of the vibrational excitations picked up by PCA. It is also worth noting again that the distribution of eigenvector components at $\omega = 0.81\mu\text{m}^{-1}$ is not random, because the corresponding eigenvalue is still larger than any noise. Indeed, a quantitative description in the next paragraph will reveal some correlation even in figure 4.4.e).

The position of the described mode patterns in the distribution of states is finally visualized in figure 4.4.f). The stated frequencies correspond to modes number 1, 12, 66, 307 and 1151.

To quantize the decay of coherence up to position (e) at the first peak, a simple scalar product was deployed on the eigenvector components for different frequencies. Between two normalized components $\mathbf{e}_m^i$ and $\mathbf{e}_m^j$ of mode number m, the quantity

$$\Theta_{ij}(r_{ij}) = \mathbf{e}_m^i \cdot \mathbf{e}_m^j$$

measures their alignment. For parallel and antiparallel normalized vectors, Θ_{ij} will become positive and negative unity, respectively. For orthogonal vectors the scalar product is zero. If there exists an underlying coherence, Θ is dependent on the distance r_{ij} of components i and j.

Figure 4.5.a) shows the average $\langle\Theta\rangle$ in dependence of r, where the average was taken over intervals $\Delta r = 3.45\,\mu\text{m}$ which corresponds to $12\,\%$ of the mean interparticle

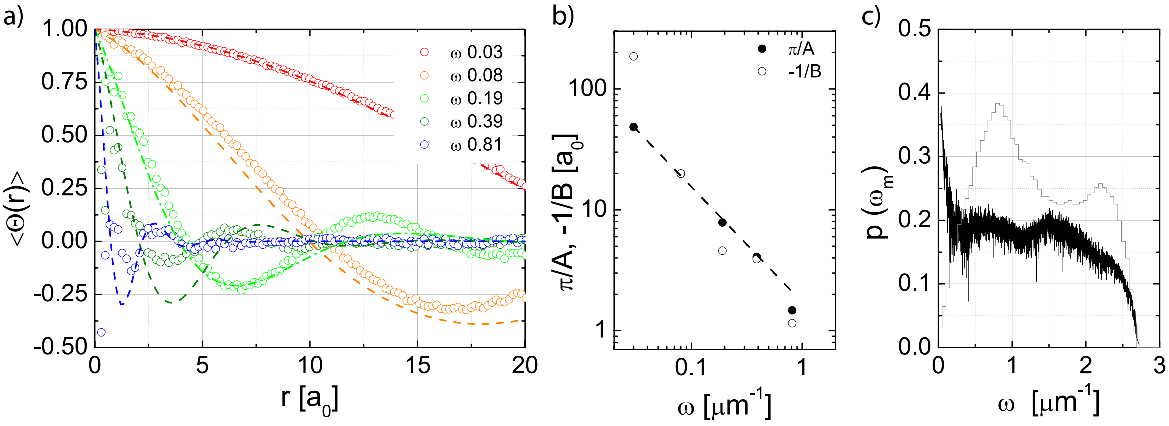

Figure 4.5.: **Measure of coherence and mode population.**
a) The r-dependence of an averaged scalar product of eigenvector components gives a measure for the degree of orientation correlation and its spatial extension. The dashed lines are fits with the model $f(x) = \cos(A \cdot r) \cdot \exp\{B \cdot r\}$.
b) Fit parameters A and B of the model. The periodicity A (filled black circles) obeys a power law (dashed black line).
c) The participation ratio $p(\omega_m)$ measures the population of mode m. In the background, the density of states is plotted again for mapping frequencies. For details, see text.

distance a_0. This quantity becomes zero for a random distribution of orientations. Application to the mode structure in figure 4.4, however, yields oscillatory behavior that decays towards zero only for large distances. This is already numerical evidence for correlation in the eigenvectors $\mathbf{e}_m$. It is striking that even for the highest frequency $\omega = 0.81\,\mu\text{m}^{-1}$, where the corresponding mode pattern appears to be random, $\langle\Theta(r)\rangle$ exhibits some structure and suggests coherence to a small degree on short lengthscales (blue circles).

The data yields quantitative results if fitted with a model $f(r) = \cos(A \cdot r) \cdot \exp\{B \cdot r\}$, where the fit parameters A and B reveal periodicity and decay length, respectively. The fits are shown also in figure 4.5.a) as dashed lines. Apparently, the assumed model fails in the description of the data at the first peak by overestimation, i.e. the correlation is weaker than found by the model at short distances. Further, the position of extrema suffers from uncertainty of $\approx 5\,\%$. For the highest frequency, the agreement is even worse (blue curve) due to scattered data points at $r < a_0$. Nevertheless the decay of $\langle\Theta(r)\rangle$ to zero, i.e. the extension of correlation, and the overall periodicity are reproduced reasonably well.

Because negative values of $\langle\Theta(r)\rangle$ correspond to anticorrelation, the distance π/A from maximum to minimum gives a measure for the spatial size of the vortices. In figure

4.5.b), the fit parameters A and B are plotted versus frequency. A fit to the periodicity (filled black circles) reveals algebraic behavior of vortex size with an exponent of -0.95 ± 0.03 (dashed black line). The fit is quite convincing, merely the bad data point for the $\omega = 0.81\,\mu\mathrm{m}^{-1}$-data is a bit off. The fit parameter for the decay length (empty circles), however, does not show such a clear dependence. This reflects failure of the model to reproduce the correct peak height in graph a), upsetting the confidence in this particular parameter.

Another, maybe more analytic tool for mode pattern analysis is the participation ratio $p(\omega_m)$ [Bri10, Che10]. It measures the degree of spatial localisation of a mode m and is defined by

$$p(\omega_m) = \frac{1}{N}\frac{(\sum_i |\mathbf{e}_{m,i}|^2)^2}{\sum_i |\mathbf{e}_{m,i}|^4}\,,$$

where $\mathbf{e}_m$ is again the according eigenvector of the covariance matrix. The sum runs over all N particles, accumulating all individual components. The participation ratio effectively compares a quantity of the ensemble with a quantity of single particles. For localized modes, which turn up in the patterns as significantly enlarged arrows (see for example in figure 4.4.c), the participation ratio becomes $\approx 1/N$, i.e. only a couple of particles oscillate in these modes. For a relatively homogenous distribution of amplitudes, which corresponds to delocalized modes, $p(\omega_m)$ approaches unity.
As can be seen in figure 4.5.c), the majority of modes in the system is moderately extended. For low frequencies, however, the long wavelength character demands a rise in $p(\omega_m)$. The grayed out density of states in the background indicates this to be only true for the modes contributing to the build up of the first peak. For very high frequencies, the modes finally become localized, which accounts for residual motion in the displacement field not captured by the more principal components.

Behavior towards the glass transition

To capture all aspects of vibrational behavior in the system, the dependence of the density of states on temperature is shown in figure 4.6.a). All of the pictured curves feature the same statistics, i.e. all deviations have a physical origin. For low temperatures, the distribution of excitations becomes very broad, featuring much high frequency modes which show tendencies to localize. Upon reducing the frustration in the system by lowering the external magnetic field, more excitations accumulate in the low frequency region, emphasizing the first peak. When entering the vicinity of the melting temperature, the second peak degrades to a shoulder and vanishes completely upon reaching T_G. This reflects the transition into the fluid state, which is not able to support shear stress and therefore does not allow the existence of transverse sound modes. However, even for $\Gamma = 186$, the structure of the most principal components has not changed yet but instead still exhibits large correlation. This is visualized in figure 4.6.b). The patterns are only broken for temperatures below $\Gamma = 180$, where

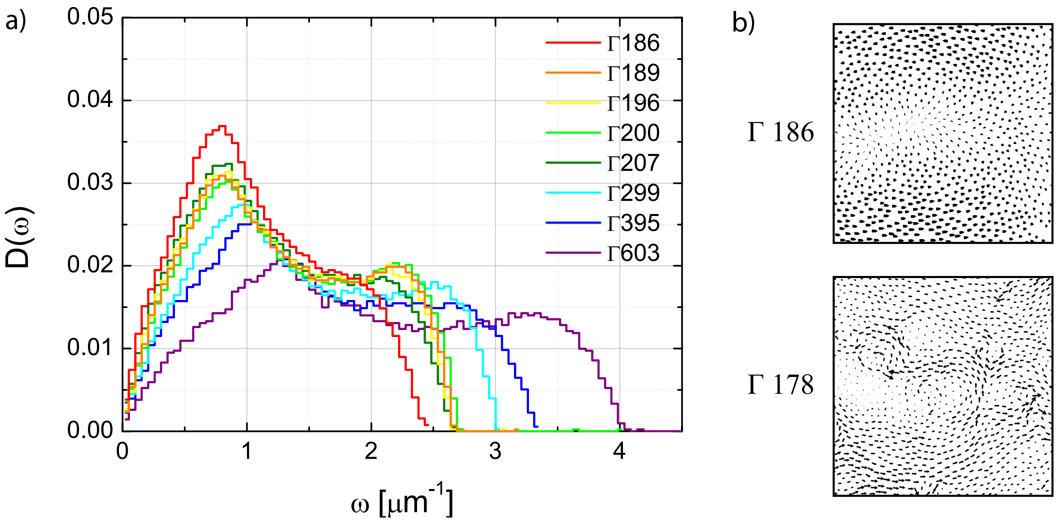

Figure 4.6.: **Temperature dependence of the density of states.**
a) Low temperatures cause a broad distribution of excitations. Unfreezing results in an increase of low frequency modes, while the second peak degrades to a shoulder and vanishes at the melting point $\Gamma = 186$.
b) Mode patterns in the vicinity of the transition temperature.

they also show slight localisation (the data for $\Gamma = 178$ is taken from the cooling cycle, compare 3.2.6).
On a side note, the density of states for the fluid is not shown in figure 4.6.a) because in the droplet, it is not possible to collect the necessary statistics due to arising drift. However, since the mode patterns do not change significantly with the number of frames (not shown), the loss of coherence evident from figure 4.6.b) is not an artifact.

4.3. Derivation from dispersion relations

Besides the covariance matrix, dispersion relations acquired by the method described in [Kei04] contain information on the vibrational spectrum of the system under the assumption of plane wave like excitations as well. This was indirectly tackled in section 4.1 of this chapter already. The central statement of equation (4.1) concerns the dependence of the density of states on the increase of q vectors in a frequency interval, i.e. the dispersion slope. In other words, the mode wavelength affects their distribution in the frequency spectrum. By this, the results obtained in chapter 3 should enable an alternative route to mode analysis.

The first step is to convert the eigenvalues $\lambda(q)$ of the dynamical matrix $\underline{\mathbf{D}}$ to frequencies ω. They are directly proportional, as given by equation (3.4), so that by taking the square root, frequencies are obtained. Because the field of view determines an accessible length scale for the wave vector[4] and the mass of the colloids used in the experiments is known[5], equation (3.4) delivers real frequencies $[\omega] = \text{rad/s}$. The dispersion relation as obtained from the conversion in shown in figure 4.7.a).

In order to close down on the density of states, the Debye velocity demanded by equation (4.2) may be extracted by a linear fit to the small wavevector region of the transverse and longitudinal branches, where the plane wave approximation holds and therefore the Debye model applies. This is indicated by blue lines in figure 4.7.a). The goodness of the fits (error $\approx 3\,\%$) demonstrates the accuracy of the Debye model in the dispersion data. This procedure yields $v_\| = 0.0062\,\text{m/s}$ and $v_\perp = 0.0028\,\text{m/s}$ for longitudinal and transverse sound velocities, respectively. These values may be put together to obtain the Debye velocity $v_D = v_\| v_\perp \cdot (v_\perp^2 + v_\|^2)^{-\frac{1}{2}} = 2.55 \cdot 10^{-3}\,\text{m/s}$ which determines the density of states in the Debye model.

For application of equation (4.1) beyond the Debye model, however, this approach is not sufficient. To obtain the exact wave vector dependent sound velocities $v(q)$, the derivatives of the dispersion curves may be computed by utilizing the five-point stencil of the original data. This method from numerical analysis uses four neighbors and the data point itself to make up a more smooth grid of data [Abr70]. The first derivative of $\omega(q)$ then reads

$$\omega'(q) = \frac{-\omega(q+2h) + 8\omega(q+h) - 8\omega(q-h) + \omega(x-2h)}{12h},$$

where h is the spacing between two data points (given by the smallest wave vector $q_{\min} = 2\pi/L$). The result is shown in figure 4.7.b) as black and red circles for longitudinal and transverse polarization, respectively. Blue horizontal dashed lines mark sound the velocities from the fit in figure 4.7.a). They agree reasonably well with the transverse sound velocity and to a lesser extend to the longitudinal sound velocity in the long wavelength limit.

There is yet a third method to obtain the wavevector-dependent sound velocities. Here, a model from the analytical textbook approach for the dispersion relation is assumed. As derived for example in [Ash09a], a solution for the particles equation of motion leads to the dispersion $\omega(q) = 2 \cdot \sqrt{\lambda/M}\,\left|\sin(\frac{1}{2}\,qa)\right|$, where λ is the force constant of the system (eigenvalue of the dynamical matrix), M the particle mass and a the lattice constant. Fitting graph a) with a corresponding model $\omega(q) = A \cdot |\sin(B \cdot q)| + C \cdot q$ yields constants A, B and C, which in turn can be used in an analytic derivative to calculate the corresponding sound velocities $v(q)$. The linear term is added to account for the structure of the dispersion curves in q space, as the periodicity beyond the

---

[4] Since the dispersion relations are averaged over different directions, the field of view is chosen to $508 \times 508\,\mu\text{m}^2$, which is smaller than the actual available field of view of the camera. This restricts resolution of the wavevector to $1.79\,\text{m}^{-1}$.

[5] With an effective density of $\varrho_{eff} = \varrho_{Coll} - \varrho_{H_2O} = 0.5\,\text{g/cm}^3$, the mass of particles amounts to $2.39 \cdot 10^{-15}\,\text{kg}$.

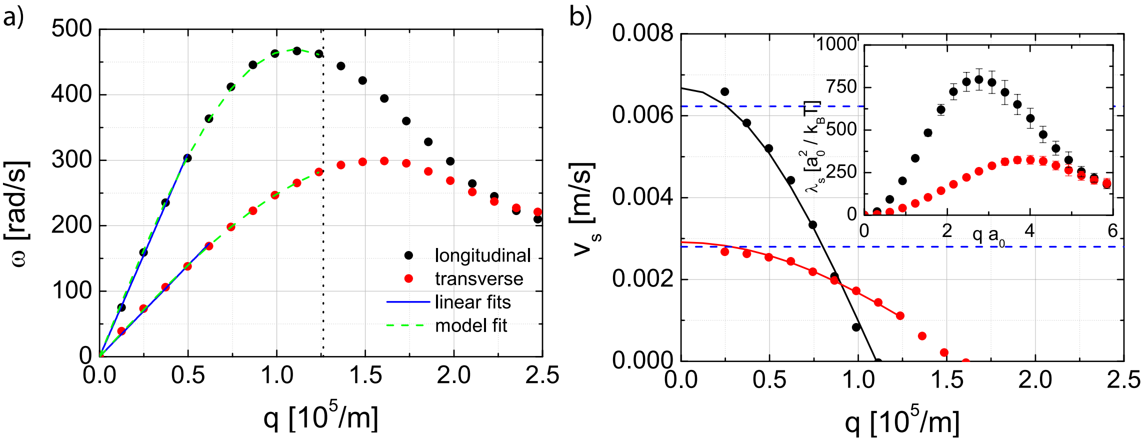

Figure 4.7.: **Sound velocities.**
a) Linear and model fits (solid blue and dashed green lines, respectively) of the dispersion curves $\omega(q) = \sqrt{\lambda_s/M}$ to obtain the sound velocities of longitudinal (black) and transverse (red) waves.
b) The computation of the first numerical derivative $\nabla_q \omega$ yields longitudinal and transverse sound velocities (filled circles). Another route is taken by fitting the dispersion data with a model and obtaining the sound velocities by analytic derivation (solid lines). Dashed blue horizontal lines correspond to the Debye velocities obtained by the linear fit in a). The inset shows the 'original' dispersion relation for the system at $\Gamma = 200$, taken from chapter 3.

quasi Brillouin zone does not decay to zero. The actual fits are shown in graph a) as dashed green lines up to the $qa_0 = \pi$ which is indicated by a dotted vertical black line. The results for the corresponding sound velocities $v_s(q)$ are shown in graph b) as solid lines. They agree with the data obtained by the five-point stencil very well. In addition, they provide information even in the low q regime, where no derivative can be computed due to the lack of neighboring data.

4.3.1. Results

Because the density of states contains *all* vibrational excitations, contributions from both longitudinal and transverse waves have to be accounted for. In textbook approaches, this is realized by simply adding up the respective number of states per wave vector. With experimental data, which may be sparse or exhibit nonlinear spacing, this may be achieved by computing $D(\omega)$ with equation (4.1) separately for longitudinal and transverse branches. Subsequently, the data is sorted into frequency bins accumulating the respective contributions. The evaluation procedure is sketched in figure 4.8.a). The blue bars in the background indicate the resulting histogram, giving

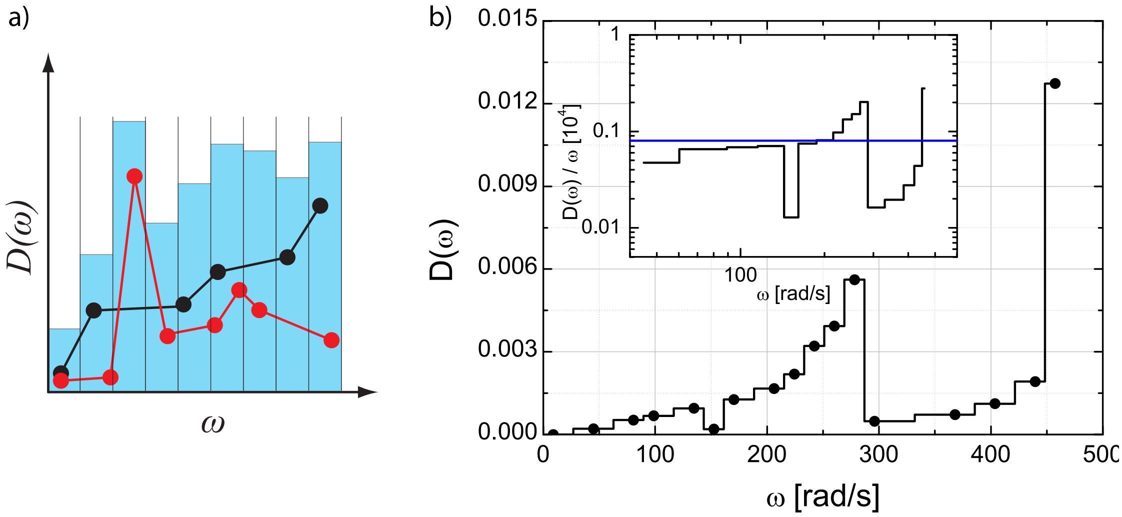

Figure 4.8.: **Density of states from dispersion relations.**
a) Sketch of the evaluation procedure. Data from both branches (black and red symbols) are computed separately before merged in a histogram (indicated as blue bars in the background).
b) Density of states from dispersion relations. Two peaks are reminiscent of the vanishing sound velocities at the quasi Brillouin zone edge. The inset shows the scaled DOS, which is compared to the prediction of the Debye model (blue line).

a distinctive shape to the density of states. Figure 4.8.b) shows the results of the computation. The most distinctive feature are the two peaks. They originate from the flat plateau of the dispersion curves at the quasi Brillouin zone edge and indicate a significant increase in mode density in the frequency spectrum. With an infinite resolution in q space, these peaks would grow into real Van Hoove singularities. The manifestation of the peaks therefore indicates the quality of the field of view.

The existence of peaks in the distribution also raises questions regarding normalisation, because the frequently used approach of referring to the area under the curve depends strongly on the shape of the peaks. The more pronounced the singularities, the lower the baseline becomes. In the case of colloidal experiments, however, the number of involved particles can be determined, which allows the normalisation regarding the available degrees of freedom.

The inset of figure 4.8.b) shows the reduced density of states. By scaling with the frequency, Debye behavior as given by equation (4.2) is obtained. For comparison, the prediction from the Debye model with sound velocities obtained by the linear fits in figure 4.7.a) is indicated by a straight blue line. The model succeeds in catching the average distribution up to the first peak. Especially in the region around 200 rad/s, the two curves coincide. However, the fifth bin of the histogram clearly is subject to incorrect filling. The difficulty here is to achieve a homogenous distribution. Because of sparse q values (their density is given by the size of the field of view), the binsize may not become too small. In this case, the binsize was chosen to $\Delta\omega = 20.7\,\mathrm{rad/s}$. A solution to this dilemma is given in the next paragraph.

Cumulative density of states

A potentially more clear quantity for measuring the population of modes is the cumulative density of states (cDOS) $D_C(\omega)$. Here, all contributions to the DOS are added up with increasing frequency. This approach prevents production of misleading trends in the DOS by 'unfortunate' data binning. Debye behavior is indicated by a quadratic increase of the cDOS. This can be seen easily by writing down the functional dependence of the (Debye-like) DOS $D(\omega) = D^* \cdot \omega$, where $\omega = 0, 1 \cdot \Delta\omega, 2 \cdot \Delta\omega, \ldots, N \cdot \Delta\omega$ and $D^* = L^2/2\pi v_D^2$ can be read from equation (4.2). The value $N = \omega_{\max}/\Delta\omega$ takes into account the discretization of frequencies by sorting the data into bins of finite binsize $\Delta\omega$ (see section 4.2.1). Then, with $\omega = n \cdot \Delta\omega$, the cumulative DOS is nothing more than an arithmetic progression:

$$\begin{aligned} D_C(\omega) &= D^*\Delta\omega + 2D^*\Delta\omega + \ldots + nD^*\Delta\omega \\ &= D^*\Delta\omega \sum_{i=1}^{n} i \\ &= D^*\Delta\omega \frac{n(n+1)}{2} \\ &= \frac{D^*}{2}\left(\frac{\omega^2}{\Delta\omega} + \omega\right) . \end{aligned}$$

Any excess of modes beyond the Debye model will result in a stronger growth.

In figure 4.9.a), this quantity is shown for the inverse eigenvalues λ^* of the covariance matrix (black line). The red line is a quadratic fit for the interval indicated by the shaded region. The only fit parameter m with its uncertainty is given in the lower right corner of the graph. Judging from the convincing agreement between fit and original data for $0 < \omega < 0.75\,\mu\mathrm{m}^{-1}$ (the error only amounts to $2\,\%$), Debye behaviour is present indeed (as already suggested earlier, compare the inset of figure 4.2). At the highest frequencies, the cDOS converges towards one, indicating a decay to zero in the DOS.

In figure 4.9.b), the cumulative DOS is plotted for the data obtained by the derivation of the dispersion curves (black line). Again, the red line is a quadratic fit. Agreement is found up to $\omega \approx 200\,\mathrm{rad/s}$. Here, the error also only amounts to $2\,\%$, confirming Debye behavior. At higher frequencies, however, a clear excess of modes becomes apparent, representing excitations contribution to the first peak. The same is true for the upper end of the spectrum. The non-continous differentiability at $\omega \approx 275\,\mathrm{rad/s}$ is

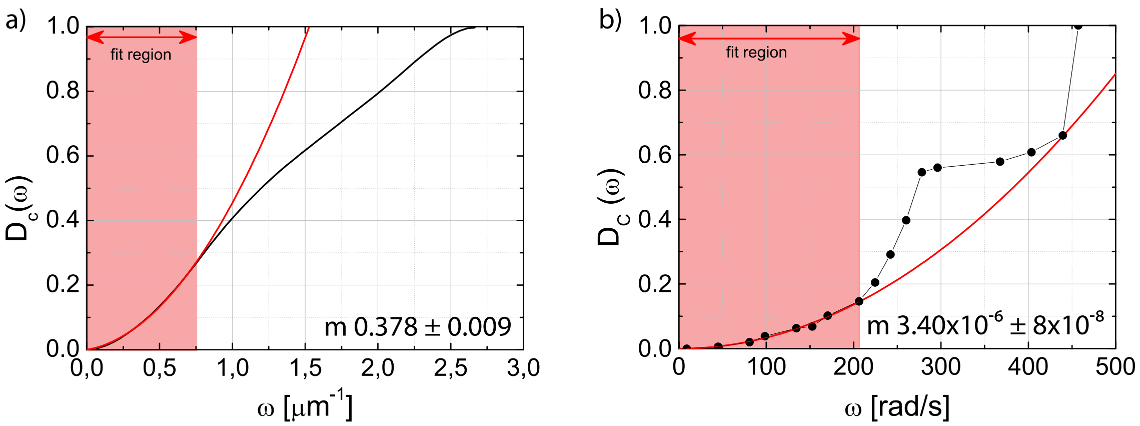

Figure 4.9.: **Cumulative density of states.**
a) cDOS of the inverse eigenvalues obtained by PCA (black curve, compare figure 4.2).
b) cDOS of data from dispersion curves (connected black symbols).
The shaded regions indicate the interval used to fit a quadratic function $f(x) = m \cdot x^2$ (red solid lines). The fit parameter is given in the lower right corner. In both graphs, the low frequency region obeys the Debye model with a deviation of only 2 %.

a striking feature and conveys the fact that this peak will turn into a real singularity for higher resolution in ω. Between the two peaks at $\approx 450\,\mathrm{rad/s}$, the distribution re-engages the fit, hence approaching again Debye-like behavior. This is not surprising as a vital assumption for the dispersion computations was a spectrum of plane waves in the first place.

4.4. Comparison of PCA with dispersion data

To conclude matters, a comparison between the density of states obtained by principal component analysis and by derivation of the dispersion curves is worthwhile. Prior to this, some comments have to be made on the substance of PCA data.
PCA as well as the Fourier approach only process lengthscales. Accordingly, the results can only be interpreted as snapshots of the underlying dynamics. In section 3.1.1, the excitations were assumed to be of plane wave character, fulfilling equation (3.4), and thus providing the means to connect the spatial correlations (i.e. wave vectors) to a temporal domain (i.e. frequencies). For the original PCA data, this coupling is not intrinsically given.
Nevertheless, a couple of publications associate real frequencies to the principal components [Che10, Gre11, Tan12a]. The derivation of this approach is given in a manuscript

by Henkes *et. al.* [Hen12]. There, the relation

$$\omega = \sqrt{\frac{k_B T}{m \cdot \lambda^*}}\,, \tag{4.5}$$

is developed where $k_B T$ is the thermal energy of the system, m the particle mass and λ^* the eigenvalues of the covariance matrix. A vital assumption[6] made is that the solution of the respective equation of motion always features an exponential, time-dependent term $\exp\{-ikt\}$, where k depends on the case but always is proportional to a frequency ω. In other words, plane wave behavior is assumed here as well.
This assumption is a delicate point in some of the cited works, because the boson peak reported there is explicitly attributed to *non*-planar waves ('swirling motions'). This is a very good example for how carefully the results of PCA should be interpreted.

Having found much evidence for plane wave behavior in the system at hand, equation (4.5) is applied here. This allows a comparison of PCA-data with the density of states derived from the experimentally determined dispersion relation by matching the respective units of the 'frequency' axis. In figure 4.10.a), both data are shown. In either case, the same system was analyzed ($\Gamma = 200$, $508 \times 508\,\mu\mathrm{m}^2$, only big particles) and the curves are normalized with respect to the contributing number of particles. Because both evaluation schemes rely on the accumulation of data in histograms and PCA offers more statistics to those bins, its actual density of states appears higher. Better agreement is obtained by normalization with respect to the area under the curve [Hen12]. However, the results then become very susceptible to the peak height of the reminiscent Van Hove singularities, which in turn depends on the binsize $\Delta\omega$ of the applied histogram. For high q resolution of the dispersion relations, where the peaks come much closer to real singularities, the initial agreement is also lost. Therefore, the former normalization proves to be more solid and is applied to the results in this work regardless of its initially bad agreement.
In either case, however, the positions of the first peak at $\approx 250\,\mathrm{rad/s}$ agree very well. This fact is striking, as both methods use two thoroughly different approaches. Apparently, key features of the studied system are picked up either way, which is somewhat reassuring and validates many results of this work.
Figure 4.10.b) compares the cumulative density of states, which does not depend strongly on the choice of external parameters. Thus, the good agreement of the curves for frequencies below $200\,\mathrm{rad/s}$ immediately comes to attention. The distribution of long wavelength modes is therefore adequately described by both approaches. By comparison to the prediction of the Debye model (blue line) it is clear that these modes are of a plane wave character. Significant differences only emerge at large frequencies, where PCA underestimates the amount of excitations. In fact, here the DOS from the

---

[6] This was treated in different cases with underlying Newtonian or overdamped Langevin dynamics or even athermal systems.

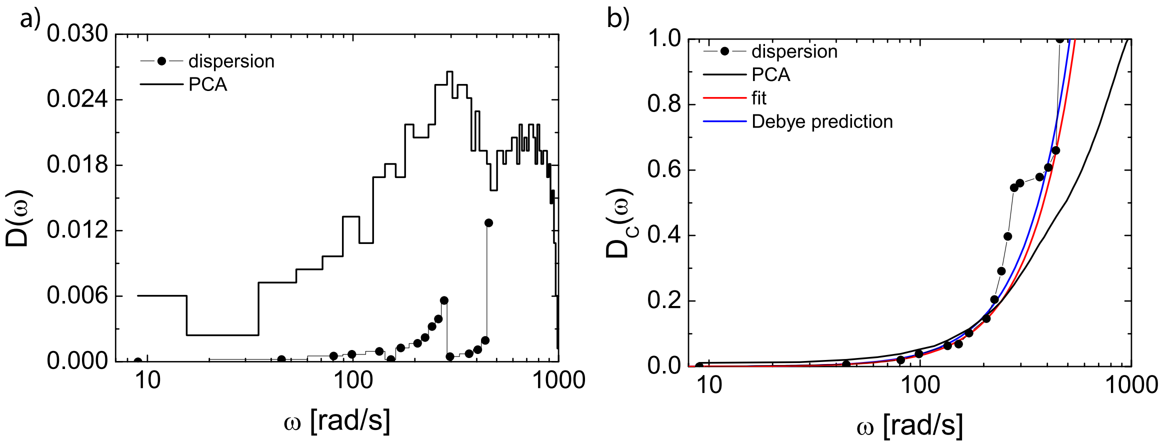

Figure 4.10.: **Comparison of the density of states.**
a) Both curves are computed for the same system and are normalized with respect to the number of degrees of freedom.
b) The cumulative density of states shows very good agreement for the low frequency/long wavelength region between the two methods. The red curve is the quadratic fit from figure 4.9.b), while the blue curve indicates the Debye prediction from the inset of figure 4.8.b).

dispersion relation also deviates slightly from the Debye prediction. This is due to the two different fit models applied (linear and sine, see section 4.3), resulting in a small but distinctive discrepancy (compare quadratic fit, red line).

4.5. Discussion

With the two approaches established, the attention may now be turned toward the relevance of the data to the glass transition or the glassy state in general.
As demonstrated, much of the vibrational excitations present in the system are of plane wave character. This picture is conveyed by evidence in the density of states (Van Hove singularities), the eigenvector structure and the agreement of PCA data with the plane wave Fourier approach. The latter also solidifies the results from chapter 3.
These findings challenge the universality of recently published results, which found even the lower part of the frequency spectrum to consist mainly of short-ranged ‘swirling motions’, i.e. non-planar excitations [Che10, Gho10]. Parts of those modes were also described as localized. This discrepancy in vibrational behavior might have its origin in the significantly different nature of the studied systems. While in the present case those properties are governed by very long ranged soft repulsion (dipolar

$1/r^3$), PMMA hard spheres were used in [Gho10]. Additional perturbations might be induced there also by the three-dimensional nature of this system (coupling to out-of-plane excitations). The treatment of dimensionality in this case is still a matter of discussion [Gho11, Lem12] and therefore also affects the results of [Kay10] where the mode spectrum of a 'disordered crystal' made of PNIPAM particles was investigated in three dimensions. Here, the soft short ranged repulsions additionally might hamper the propagation of planar wavefronts, as will the friction found in these systems [Sti14]. In intrinsically two-dimensional experiments with PNIPAM particles [Che10], the altered hydrodynamics due to confinement between two cover slides most likely also impact the formation of modes (compare chapter 6).

The nature of excitations has also an impact on their spectrum. In the experiments performed here, no proliferation of modes beyond the Debye model at low frequencies was found. Apparently, soft long ranged interactions in almost ideal two dimensional glass formers promote vibrational behavior similar to crystalline systems. Correspondingly, none of the 'anomalous behavior' discussed in the introduction is supposed to be found here. This questions the universality of the findings in [Che10, Gho10, Kay10]. Instead, the (colloidal) glass transition is described here, in accordance to the results from chapter 3, as the crossover from a rigid/solid to a soft/fluid state, where the latter is not able to support transverse (shear) waves. Evidence for this picture is found in the vanishing of the second peak in the density of states as well as the decay of orientational correlation of vibrational amplitudes at the transition temperature.

5. Dynamical heterogeneity

Driving a system towards its glass transition translates into increasing its inherent dynamical relaxation time. Various works over the past two decades have revealed the development of a structure in the spatial distribution of these relaxation times, evident from the correlation of dynamics on the approach to the nonergodic state [Miy88, SR91, Kob97, Wee00, Keg00].
The relaxation times may be associated with particle mobilities and described by a mobility field. While distributed randomly in space in a homogeneous fluid, they appear clustered in disordered solids. This phenomenon is called 'dynamical heterogeneity' and shows that structural relaxation is a nontrivial dynamical mechanism in these systems.

A first explanation for the occurrence of dynamical heterogeneity evolved from the efforts of Kauzmann to connect the glass transition temperature T_G to the entropy difference between the supercooled liquid and the stable crystal [Kau48], yielding the famous 'entropy crisis' and the corresponding Kauzmann-temperature T_K. The relaxation of the liquid, identified as a dynamical process, was later related to configurational entropy by Adam and Gibbs [Ada65]. Configurational entropy counts the number of stable configurations accessible by the system. As the supercooled liquid becomes nonergodic with decreasing temperature, the configurational entropy also drops, because the increased frustration limits the available configuration space. In other words, the number of sites a single particle can travel to decreases, because neighboring particles begin to obstruct movement (known as the 'cage effect' from mode coupling theory [Bar89]). In fact, in order to move at all, neighboring particles have to rearrange themselves in order to let the initial particle pass through. This set of particles was termed 'cooperatively rearranging region', illustrating the underlying mechanism of this simple model pretty well. It also becomes clear from those considerations that these regions are expected to grow with decreasing temperature, because an increasing amount of (coordinated) rearrangement is needed for a single particle to move. This fact is also captured in recent theoretical work [Gar02].

The study of dynamical heterogeneity has also led to considerations about perceiving the glass transition as a nonequilibrium phase transition. Because of its fluctuation-dominated character, it reminds of critical phenomena with a growing static correlation length. The theoretical tools like renormalization group or field theory would be applicable if this correlation length could be determined in glassy systems. At the first

glance, it seems rather obvious to pick up on the length scale of those cooperatively rearranging regions introduced in the preceding paragraph. However, these turn out to be hard to determine for the following reason: The distinction between mobile and immobile particles is not static, but dynamical. In other words, all attempts to grasp this content via standard methods as density correlation (for example by scattering experiments) are bound to fail. Usually, the studied functions only depend on densities at two different locations, but only one single point in time. The additional dimension *time* is at most used for averaging. Vice versa, common functions studying the dynamical properties of a system average over spatial distributions.
A possible approach are so-called *four-point functions*, which correlate the information available at two points, each at two times [Das91, Sil99, Glo00]. In other words, rather than an ensemble of snapshots, an ensemble of 'movies' (i.e. linked trajectories) has to be investigated, as the phase transitions broken symmetry would be located in space time (trajectory space) rather than real space.

In order to study heterogeneous dynamics with the experiment described in this thesis, the timescale on which those appear has to be determined first, since earlier investigations yielded static results in the glassy state [Maz11]. For this, it is reverted to an established method before the question of a correlation length is tackled.

5.1. Overlap order parameter and susceptibility

As a starting point to describe spatial-temporal correlations, usually a function

$$f(t) = \int \mathrm{d}\mathbf{r}_1 \mathrm{d}\mathbf{r}_2 \rho(\mathbf{r}_1, 0)\rho(\mathbf{r}_2, t)\delta(\mathbf{r}_1 - \mathbf{r}_2)$$

is considered. Here,

$$\rho(\mathbf{r}, t) = \sum_{i=1}^{N} \delta(\mathbf{r} - \mathbf{r}_i(t))$$

is the point density of N particles in a volume V. This function simply correlates the density at two different points in time and must therefore still be considered *two-point*. Yet, $f(t)$ will indicate a timescale which is related to *four-point* quantities as shall be seen later. For short times, $f(t)$ contains information about the number of particles with slow dynamics. In fact, only particles which overlap their initial position or randomly travel to the starting point of another particle contribute to the integral. Thus, this function will decay very rapidly due to the vibrational motion of particles. However, the correlations one is interested in occur at longer time scales. This was tackled in the literature [Fra99, Glo00] with the discussion of a coarse-grained approach, which also addresses experimental issues[1]. By introducing an overlap function

$$w(|\mathbf{r}_1 - \mathbf{r}_2|) = \begin{cases} 1 & \text{if } |\mathbf{r}_1 - \mathbf{r}_2| \leq a \\ 0 & \text{if } |\mathbf{r}_1 - \mathbf{r}_2| > a \end{cases}$$

in terms of a paramter a, $f(t)$ may be rewritten as

$$Q_4(t) = \sum_{i=1}^{N} \sum_{j=1}^{N} w(|\mathbf{r}_i(0) - \mathbf{r}_j(t)|) \tag{5.1}$$

and acts as an order parameter. In the computation of this quantity, a may be associated with some characteristic length as cage size, vibrational amplitude or particle diameter. Because the decay behavior of the order parameter depends crucially on a, figure 5.1.a) shows $\langle Q_4(t)\rangle/N$ for different values, where the average is taken over time[2]. The emerging function can be interpreted as the fraction of particles overlapping with their initial position in a later frame. For very short times, where all particles still remain at their respective starting position, $Q_4(t \to 0)/N$ obviously equals one. For later times, this function does not decay to zero because the probability that a particle overlaps the starting position of a neighboring particle does not vanish. The fraction of those particles is exactly given by the long time limit of $\langle Q_4(t \to \infty)\rangle/N$. Accordingly, this value becomes larger for increasing a, as apparent from the graph.
Because the data conveys dynamical information, a two step process typical for glassy systems becomes visible for $a \geq 1.725\,\mu\text{m}$. This corresponds roughly to the diameter of small particles. The curves drop to a plateau, which indicates arrest. In other words, only a fraction $1 - \langle Q_4(t)\rangle/N$ of particles is mobile enough to rearrange significantly.
In figure 5.1.b) $\langle Q_4(t)\rangle/N$ is shown for different states below the glass transition temperature. The overlap parameter was chosen to be $a = 4.485\,\mu\text{m}$, which is about the diameter of the big particles. The reason for that choice is discussed later in this section.

For low temperatures (high interaction strength), the plateau extends over more than two decades at a very large value. Almost all particles remain localized. While this does not give any information about the correlation of these particles yet, it determines the timescale on which these correlations *might* occur. The upper bound is given by the eventual decay of the plateau at $t \approx 10^5$ seconds. For longer times, the initial structure is lost, i.e. all particles have left their starting positions and the overall dynamics is thus uncorrelated as in a fluid (it is stressed here again that this conclusion depends on the choice of a).

Figure 5.1.b) confirms the perception that the persistence time of a cage (in the mode

---

[1] Because of limited spatial resolution in experiments, the decay of $\langle Q_4(t)\rangle/N$ evaluated with a point density is vastly accelerated, giving misleading results. Instead, $\rho(\mathbf{r}, t)$ should rather be interpreted in terms of a volume fraction, paying respect to the finite size of particles.

[2] Compare section 3.2.6. Throughout this chapter, data from the heating cycle is used.

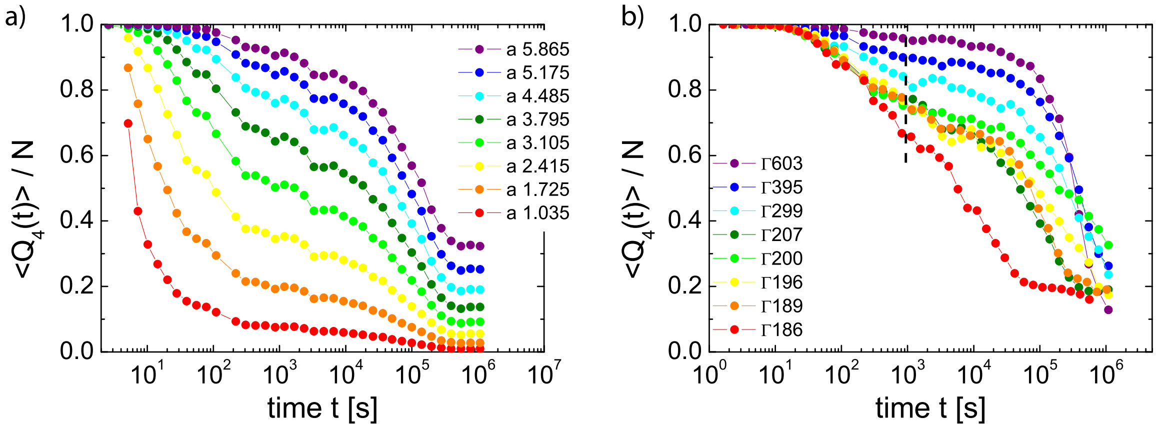

Figure 5.1.: **Order parameter $Q_4(t)$.**
a) For $\Gamma = 207$, decreasing the overlap parameter a (given in microns) accelerates the decay of $Q_4(t)$. For values comparable to the particle diameter $\sigma_S = 2.5\,\mu$m of the small species, a two step relaxation process marked by a plateau emerges. The mobile fraction of particles *might* be spatially correlated on timescales given by the plateau.
b) Temperature dependence of $Q_4(t)$ with $a = 4.485\,\mu$m. The plateau value drops with increased temperature, indicating a smaller fraction of static particles. The onset of the plateau is constant for all temperatures, as indicated by the black dashed line. The choice of a will become clear later.

coupling picture) extends for lower temperatures, facilitating a prolonged correlation time, as the plateau grows in length for increasing Γ. The same result is somewhat conveyed by the alpha relaxation in mean squared displacement data (figure 3.6, section 3.2.3).
The lower bound of a possible correlation time is given by the onset of the plateau, where only a fraction of particles rearranges (possibly cooperatively). It is noteworthy that the onset of the plateau/shoulder occurs always at the same time, as indicated by the black dashed line. This persists although the overall dynamics is increased for lower Γ, as indicated by the faster initial drop of those curves. This intriguing fact suggests a short correlation time window for low Γ, while deep in the glassy state, the distribution of lifetimes of 'dynamical clusters' might be much more extended. For times $t < 100$ seconds, the short time diffusion is visible (compare again the MSD in figure 3.6).

Because of the high computational effort for such extremely long sets of data, a coarse graining was applied, where only frames of every 100 seconds were evaluated. To probe the short time regime nevertheless, a second calculation with high temporal resolution (but significantly shorter dataset) was done as well. The data shown in figure 5.1 incorporates both.

Next, the connection between the timescales contained in $Q_4(t)$ and four-point quantities is outlined. For this, the four-point time dependent density correlation function

$$\begin{aligned} G_4(\mathbf{r}_1, \mathbf{r}_2, \mathbf{r}_3, \mathbf{r}_4, t) = &\langle \rho(\mathbf{r}_1, 0)\rho(\mathbf{r}_2, t) w(|\mathbf{r}_1 - \mathbf{r}_2|) \rho(\mathbf{r}_3, 0)\rho(\mathbf{r}_4, t) w(|\mathbf{r}_3 - \mathbf{r}_4|)\rangle \\ &- \langle \rho(\mathbf{r}_1, 0)\rho(\mathbf{r}_2, t) w(|\mathbf{r}_1 - \mathbf{r}_2|)\rangle \times \langle \rho(\mathbf{r}_3, 0)\rho(\mathbf{r}_4, t) w(|\mathbf{r}_3 - \mathbf{r}_4|)\rangle \end{aligned}$$

is considered. The corresponding radially averaged four-point correlation function $g_4(r, t)$ is the time-dependent analogue to the well known static density correlation function $g(r)$, also called the pair correlation function [Lac02]. It picks up dynamically changing structures. Theoretical work [Lac03] showed that

$$g_4(r, t) = \left\langle \frac{Q_4(t)}{N} \right\rangle^2 g_4^\star(r, t) \, ,$$

where $g_4^\star(r, t)$ contains the structural information of the initial configuration, but only considers particles which are found overlapping at time t. That is, $g_4^\star(r, t) = g_{\mathrm{ex}}(r) - 1$ where, depending on the time t, certain particles are excluded from the calculation of $g(r)$ (indicated by the subscript ‘ex’).
Intriguingly, this means that $Q_4(t)$ acts as an envelope for the amplitude of the four-point density correlation function, i.e. $Q_4(t)$ governs whether there may be possible spatio-temporal correlations or not, and if so, how strong they might be.

Theoretical consideration of these kind of functions are manifold [Fra99, Don02, Glo00, Lac02]. A noteworthy achievement is the equation for a quantity $\chi_4(t)$,

$$\chi_4(t) = \int \mathrm{d}\mathbf{r}_1 \mathrm{d}\mathbf{r}_2 \mathrm{d}\mathbf{r}_3 \mathrm{d}\mathbf{r}_4 G_4(\mathbf{r}_1, \mathbf{r}_2, \mathbf{r}_3, \mathbf{r}_4, t) \, ,$$

which is the spatio-temporal analogue to the isothermal compressibility $\kappa_T = -\frac{1}{V}(\frac{\partial V}{\partial P})_T$, because the latter is proportional to the volume integral over $g(r) - 1$ [Han06]. Thus, the temporal dependence of the four-point density correlation function is contained in $\chi_4(t)$. Interestingly, $\chi_4(t)$ can also be expressed by fluctuations of the overlap function [Lac03]

$$\chi_4(t) = \left\langle Q_4(t)^2 \right\rangle - \left\langle Q_4(t) \right\rangle^2 \, . \tag{5.2}$$

This shows again that $Q_4(t)$ contains the temporal component of possible spatial correlations. Extended theoretical analysis [Lac03] finds $\chi_4(t)$ as a function growing from zero into a peak, where the peak position reflects the correlation time. For decreasing temperature in the supercooled regime, this peak becomes more pronounced and shifts to longer times.

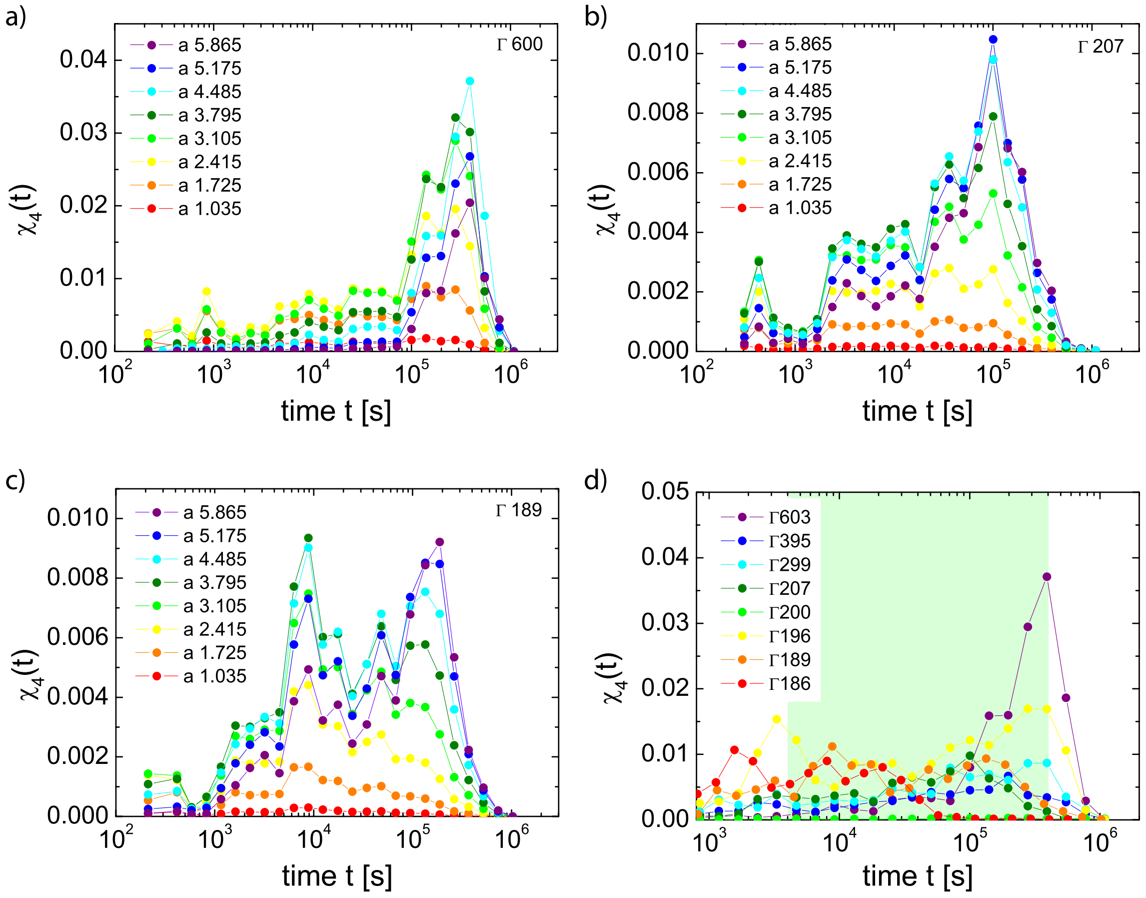

Figure 5.2.: **Susceptibility of the four-point correlation function.**
a-c) For $\Gamma = 603, 207, 189$, increasing a (given in microns) yields growing fluctuations up to a value of roughly the diameter $\sigma_B = 4.5\,\mu\text{m}$ of large particles, where $\chi_4(t)$ saturates. Thus, $a = 4.485\,\mu\text{m}$ is chosen for all calculations in this section.
d) $\chi_4(t)$ for different temperatures. Noisy data prevents the unambiguous identification of correlation times.

In figure 5.2.a-c), the results for $\chi(t)$ are plotted in dependence of the overlap parameter a for three different temperatures as indicated in the upper right corner of the graphs. Equation (5.2) was evaluated by binning the $\langle Q_4(t)\rangle/N$-data as presented in figure 5.1.a) into time intervals of $\Delta t = 200$ seconds and computing the respective squared averages. Naturally, the fluctuations of $Q_4(t)$ initially grow with a. Except the case $\Gamma = 603$ deep in the frozen state, reaching the diameter of big particles σ_B gives the larges signal, i.e. the area under the curves is maximized. This furthers the notion that the vibrational amplitude is about the size of σ_B and only slightly becomes smaller deep in the glassy sate (compare graph a). Thus, $a = 4.485\,\mu\text{m}$ was also used

in figure 5.1.b).
Figure 5.2.d) shows $\chi_4(t)$ for different temperatures. The data is rather noisy such that peaks indicating different correlation times can not be identified unambiguously (with the exception of $\Gamma = 603$). Yet, it seems like the distribution is bordered by the highest and lowest interaction strength as would be expected. Therefore, the correlation timescale is located between $4 \cdot 10^3$ and $4 \cdot 10^5$ seconds as indicated by the green shading.

The bad quality of figure 5.2.b) is a consequence of noisy $Q_4(t)$ data. For a smooth order parameter, $\chi_4(t)$ would only pick up the steep decaying part of the curve (as it is the case in the present data only for $\Gamma = 603$, see figure 5.1.b). In other words, $\chi_4(t)$ should be sensitive to significant changes in $Q_4(t)$, not to its small-scale fluctuations due to uncertainty. Especially because statistics get sparse for times above 10^5 s, the curves become unreliable in this region, as demonstrated by the overlap found in figure 5.1.b) at the upper end of the timescale. This effect is dramatically magnified in the fluctuation data, thus limiting the interpretation of $\chi_4(t)$.

5.2. RMS spatial correlation function

Since $Q_4(t)$ and $\chi_4(t)$ only study the temporal behavior of dynamical patterns, other quantities tackling the spatial distribution have to be developed. For a measure of local dynamics, the root mean square (RMS) of vibrational amplitudes

$$U_i(\mathbf{R}_i) = \sqrt{\left\langle |\mathbf{R}_i - \mathbf{r}_i(t)|^2 \right\rangle_{\Delta t}} \tag{5.3}$$

is a good quantity. It is calculated per particle i and reflects its average 'activity' during the time interval Δt. As in section 3.1.1, $\mathbf{R}_i$ denotes the averaged particle position and $\mathbf{r}_i$ is the particle position at time $t \in \Delta t$. Although it is not explicitly denoted in equation (5.3), $U_i(\mathbf{R})$ is of course dependent on the length of Δt, implied by the time dependence of $\mathbf{R}$. For short times being of the order of vibrational timescales, U will be distributed homogeneously among all particles. This is expected to change if accessing the region where $\chi_4(t)$ grows above zero (compare figure 5.2). Furthermore, it is an interesting quantity because it is also dependent on time t if the assumed heterogeneities are not static. Thus, for a reasonable evaluation of $U(\mathbf{R})$, it is eminent to extend the measurement timescale t well above Δt. Otherwise, the RMS of vibrational amplitudes will convey only a static picture. Former experiments, which investigated a similar quantity[3], could not resolve the fluctuating nature of dynamic heterogeneity

---

[3] Dynamical heterogeneities were studied using an integrated square displacement (ISD) $c_i = \frac{1}{M}\int_0^\tau \Delta r_i^2(\tau)\mathrm{d}t$, where $M = \sum_{j=0}^{N}\int_0^\tau \Delta r_j^2(\tau)\mathrm{d}t$ is the normalization factor and $\Delta r_j^2(\tau)$ is the individual squared displacement of particle j for a lag time τ.

because measurements ‘only’ extended to one or two days [Maz09, Maz11]. Apparently, the system alters its dynamics on even longer timescales.

In the following, snapshots of the system at different temperatures are shown, exhibiting a spatial distribution of dynamics. Dynamics are indicated by symbol size, where large symbols correspond to large root mean square vibrational amplitudes. Figure 5.3.a) shows the system at $\Gamma = 395$, deep in the glassy state. The RMS was computed over a time interval of $\Delta t = 6.4 \cdot 10^4$ seconds, while the whole measurement lasted for $10^6\,\mathrm{s} \approx 12\,\mathrm{days}$. It becomes evident immediately that dynamics are heterogeneously distributed, as some ‘active’ regions are visible in the lower half. They are generated by cooperatively moving particles, such that their respective ‘cage’ (energy minimum) shifts significantly more than a vibrational amplitude. There is also no separation between large and small particles, indicated by two different colors (big - red, small - blue). Both species contribute to a comparable extend to the heterogeneity. Besides regions of increased motion, some single particles also show a large RMS (upper center). These may be attributed to single events, where a particle breaks its cage. In this case, the RMS becomes equal to half of the distance traveled, which is multiples of the vibrational amplitude. This does not affect neighboring particles [Maz11].

Figure 5.3.b) shows the system state at $\Gamma = 186$, close to the glass transition temperature at $\Gamma \approx 185$ (compare chapter 3). The dynamics are still distributed heterogeneously, with highly active regions in the bottom, the top left and in the top right. In contrast to the deeply frozen system, however, the regions have grown in size significantly, up to a point where they connect in some places.

The intermediate case is shown in figure 5.4 for $\Gamma = 200$. The heterogeneities appear only marginally larger than for $\Gamma = 395$, but certainly are more numerous. Single events are almost completely suppressed, they appear occasionally pairwise (three pairs can be found in graph a) in the center), although this is, technically, no longer a single event. Both Graphs a) and b) originate from the same measurement run but are computed for trajectories 134 hours apart. Apparently, the structure of dynamics has changed during this period, meaning that it is not static on this timescale. Rather, the dynamics fluctuate, such that active regions become inactive and vice versa.

This spatio-temporal character of dynamic heterogeneities can best be grasped in form of movies, where each frame contains a distribution of RMS as shown in figures 5.3 and 5.4. Each successive frame constitutes of slightly changed averaged particle positions $\mathbf{R}$ and incrementally growing or shrinking respective RMS values. Thus, a sequence of these images reflects a simplified view on the system, where spatial fluctuations of particles are damped due to the averaged particle positions. Instead, the information of vibrations is encoded in the particle size which appear to grow or shrink depending on their ‘activity’. In the following, certain aspects of these movies are evaluated quantitatively.

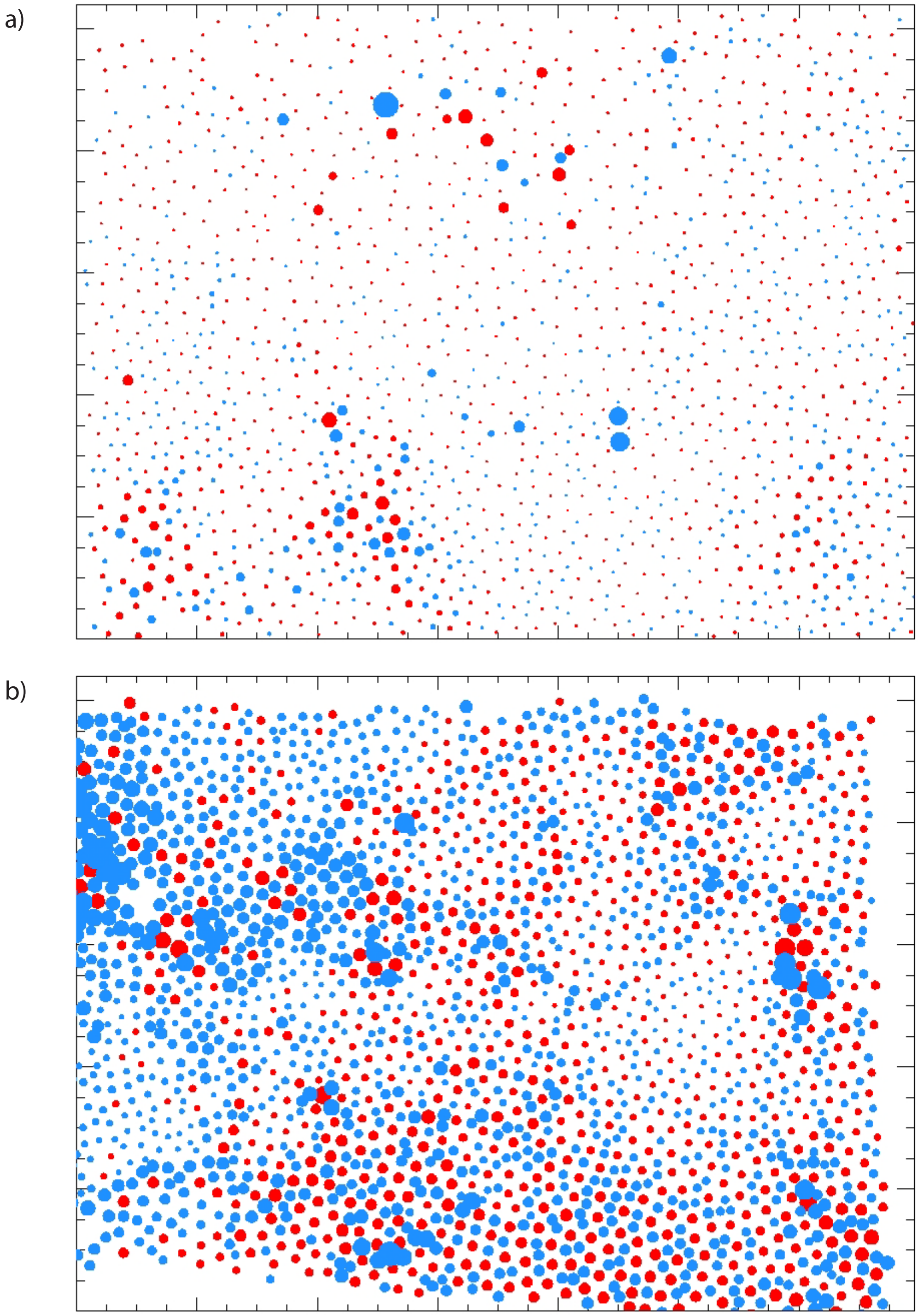

Figure 5.3.: **Dynamic heterogeneities.**
a) The RMS of particles at $\Gamma = 395$ deep in the glassy phase. Besides regions of increased activity, also single events occur.
b) The RMS of particles at $\Gamma = 186$ just above the glass transition temperature.

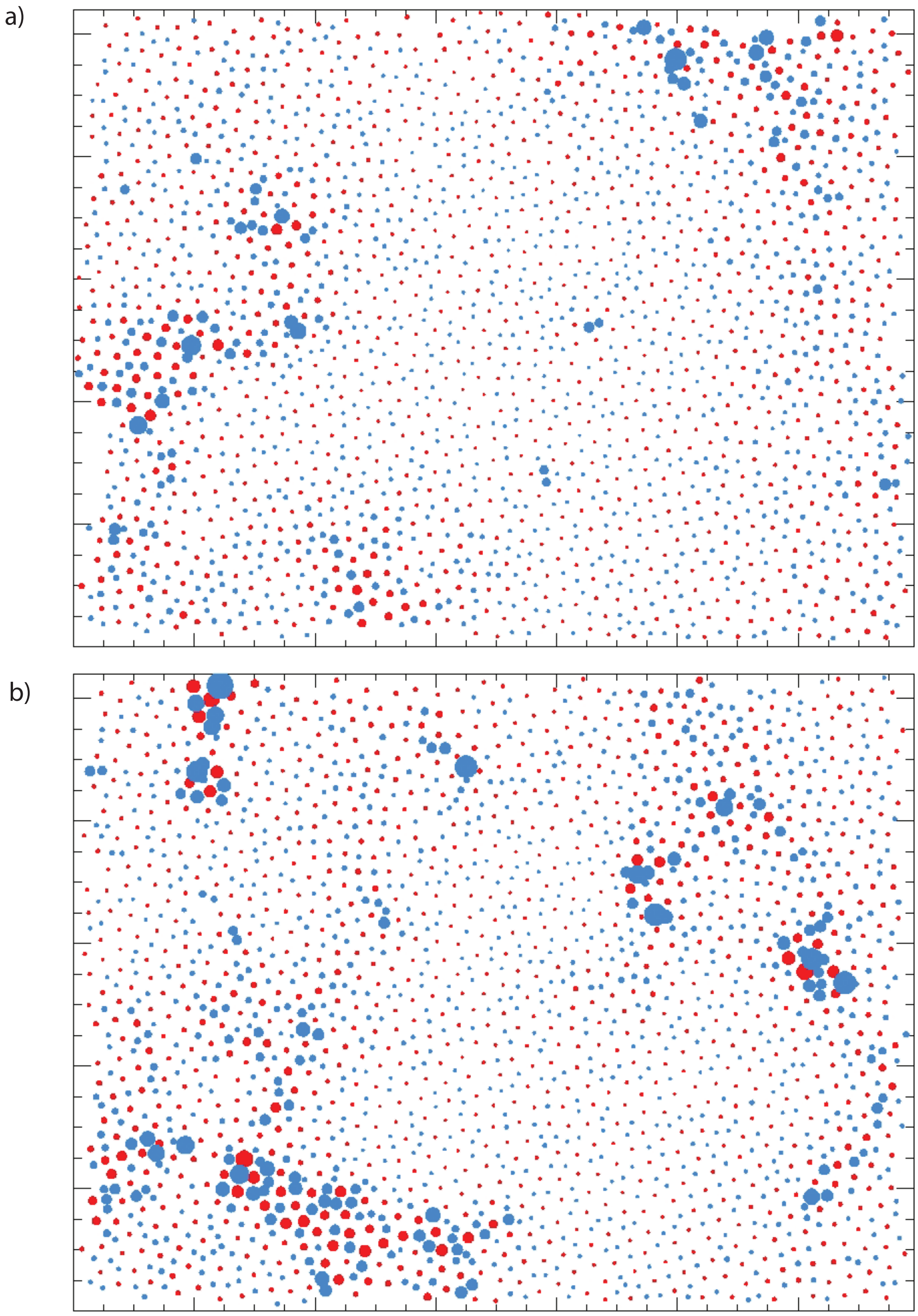

Figure 5.4.: **Time evolution of dynamic heterogeneities.** Snapshots of the distribution of vibrational amplitudes for the system at $\Gamma = 200$. Graphs a) and b) are obtained with the same parameters, but 134 hours apart.

5.2.1. Correlation length

One avenue towards the determination of the spatial expansion of the observed dynamic heterogeneities is the application of correlation techniques known from scattering experiments. In dynamic light scattering (DLS), for example, one aims to access the dynamics of the investigated system by studying the intensity fluctuations of scattered coherent and monochromatic light. The idea behind this approach is such that any change in structure of the sample will cause altered conditions for constructive or destructive interference, thus changing the scattered intensity in a fixed direction. Within this intensity fluctuation, information about the scatterers' dynamics is contained. From a recorded time series of the intensity, the first step to derive the desired information is to generate the normalized intensity autocorrelation function

$$g_2(\tau) = \frac{\langle I(t) \cdot I(t+\tau)\rangle}{\langle I(t)\rangle^2}\,. \tag{5.4}$$

Here, $I(t)$ is the measured intensity at time t, while τ describes a lag time. Of course, $g_2(\tau)$ is implicitly also dependent on the wave vector q of the scattered light. However, this quantity is usually kept fixed. For short delay times (compared to the system's internal dynamics timescale) this function retains its value because the system has not changed much, i.e. $\lim\limits_{\tau\to 0}\langle I(t)I(t+\tau)\rangle = \langle I^2(t)\rangle$. For longer delay times, on the other hand, this function is expected to decay. For very long delay times the intensities become uncorrelated such that $\lim\limits_{\tau\to\infty}\langle I(t)I(t+\tau)\rangle = \langle I(t)\rangle^2$. Therefore, a decay to unity is expected.

Much of the theory on how decaying correlation functions are connected to dynamical features, however, deals with the electric field. To align theory and experimental data, the Siegert relation [Sie43]

$$g_2(\tau) = 1 + \beta\left[g_1(\tau) - 1\right]^2 \tag{5.5}$$

is used, which connects the intensity autocorrelation function (sometimes called a second-order autocorrelation function) with the field autocorrelation function (first-order autocorrelation function).

This approach might also be utilized for the studies of dynamical heterogeneities by exchanging the time dependence with a spatial one such that $I(\tau)$ becomes $U(\mathbf{r})$ where U denominates the RMS at vector $\mathbf{r}$. Hence, for every frame, each particles vicinity is correlated with its RMS. In the following, this function is called the normalized RMS spatial correlation function. For the application to experimental data, however, some considerations have to be done first.

Because a direct approach is computationally too demanding, the Wiener-Khintchin-theorem will be used instead. It connects the power spectrum of a time series x describing a stationary process with its expected value $E\left[x(t)x^{\star}(t-\tau)\right]$ [Wie30, Khi34].

Since equation (5.4) expresses such an expected value, $g_2(\mathbf{r})$ may be calculated by two consecutive Fourier transformations $\mathcal{F}$:

$$g_2(\mathbf{r}) = \frac{\left\langle \mathcal{F}^{-1}\left(|\mathcal{F}(U(\mathbf{r}))|^2\right)\right\rangle}{\langle U(\mathbf{r})\rangle^2}\,, \tag{5.6}$$

where $\mathcal{F}^{-1}$ denotes an inverse Fourier transformation. A more detailed demonstration of the above application of the Wiener-Khinchin-theorem is given in the appendix C. The spatial Fourier transformation $\mathcal{F}$, however, demands an equidistant spaced grid. So far, only discrete (averaged) particle positions are available which are randomly distributed. Therefore, it is necessary to interpolate the spatial distributions of the RMS, as shown in figures 5.3 and 5.4, onto a regular lattice. This is achieved by the application of quintic polynomials to the triangulated particle positions [Aki78]. The result of the interpolation of figure 5.4.a) is shown in figure 5.5.a). An extrapolation grid of 1392 × 1040 cells was used, corresponding to the camera resolution used during the data acquisition process. Light red color corresponds to a large RMS, while dark colored regions indicate relative immobility. The features visible in the original image are well reproduced. The extrapolation is normalized with the mean value of $U(\mathbf{r})$. Because the triangulation obviously extends only to the particle positions bordering the field of view, the edges have to be excluded from any calculations. Considering this, Fourier (back) transformation of this yields the desired $g_2(\mathbf{r})$.

Figure 5.5.b) shows the result after performing a time average over all frames. In the color map, red corresponds to large values (i.e. high correlation) and blue/purple to low values (i.e. low correlation). Apparently, $g_2(\mathbf{r})$ spikes at the center and decays rather fast. For a grasp of length, the black bar (highlighted by a white background for better visibility) in the lower right corner corresponds to a mean interparticle distance a_0, so that the peak in the center can be attributed to the RMS of a probe particle, correlated with itself. The increased correlation indicated by the green and turquoise colors (compared to the average value given by the blue/magenta area), which extends over some few mean particle distances, hence may be traced back to the average size of a dynamically active region.

To keep the computational effort in reasonable boundaries, a coarse graining was applied to the time series. Only frames taken every 800 seconds are used in the computation of $g_2(\mathbf{r})$. This was checked to have no impact on the results, because the time interval used to determine the equilibrium positions was chosen much larger. It was made sure that still 80 frames contributed to each $U(\mathbf{r})$.

For a more quantitative analysis, the spatial distribution of $g_2(\mathbf{r})$ may also be averaged radially because of the isotropy of the system. This becomes apparent from figure 5.5.b) which exhibits radial symmetry. Thus, the normalized RMS spatial correlation function becomes $g_2(r)$ and is plotted in figure 5.6.a), top graph. It exhibits an intercept just above 1.08 and decays to unity. This is a typical behavior for intensity autocorrelation functions $g_2(t)$, where the corresponding field does not follow

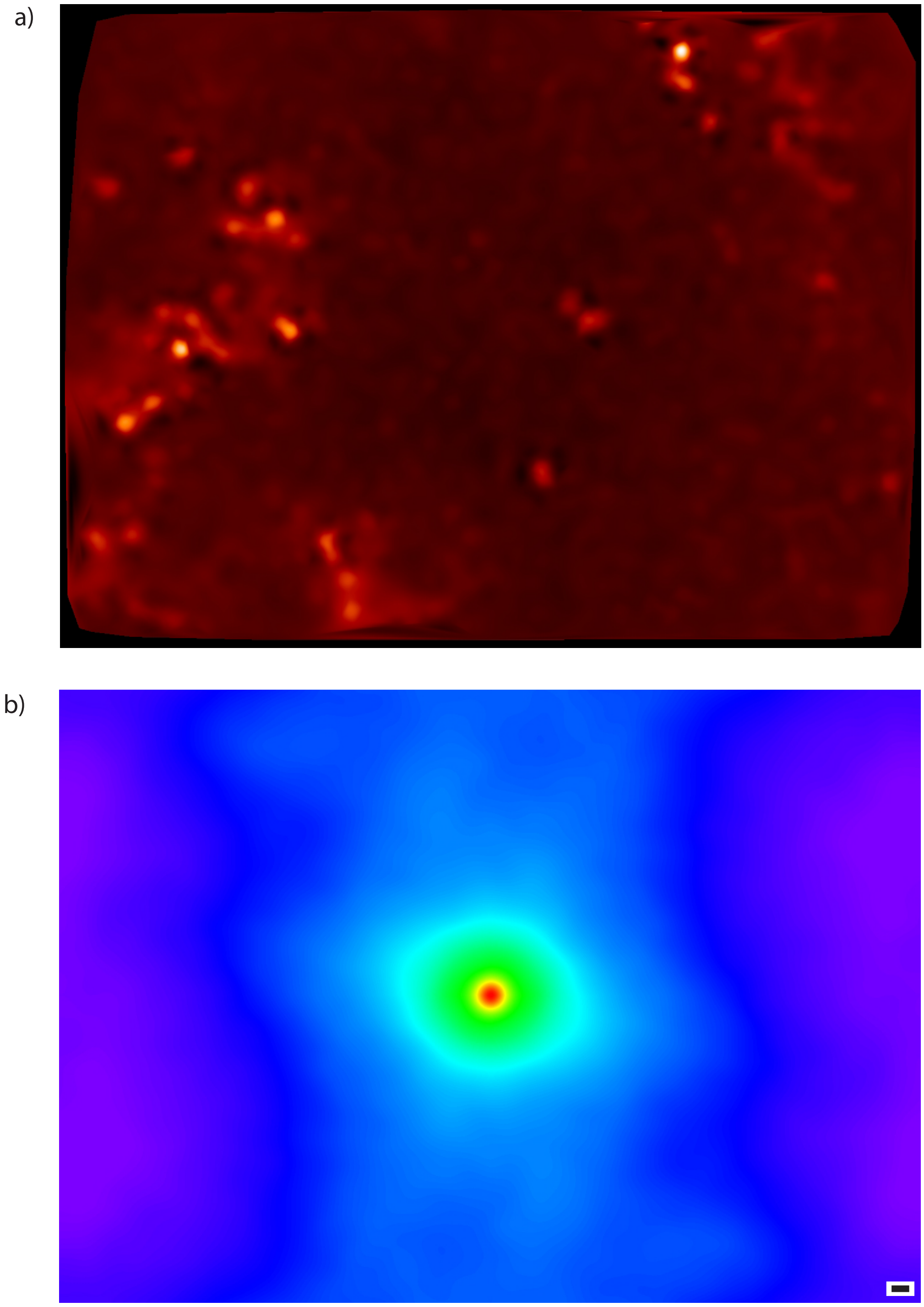

Figure 5.5.: **Extrapolation of discrete RMS values.**
a) Snapshot of the quintic extrapolation onto a regular grid of the data shown in figure 5.4.a). The color code indicates regions of increased dynamics by light red, while dark color corresponds to a small RMS value.
b) $g_2(\mathbf{r})$ computed via equation (5.6). Red corresponds to large correlation, blue/purple to low correlation.

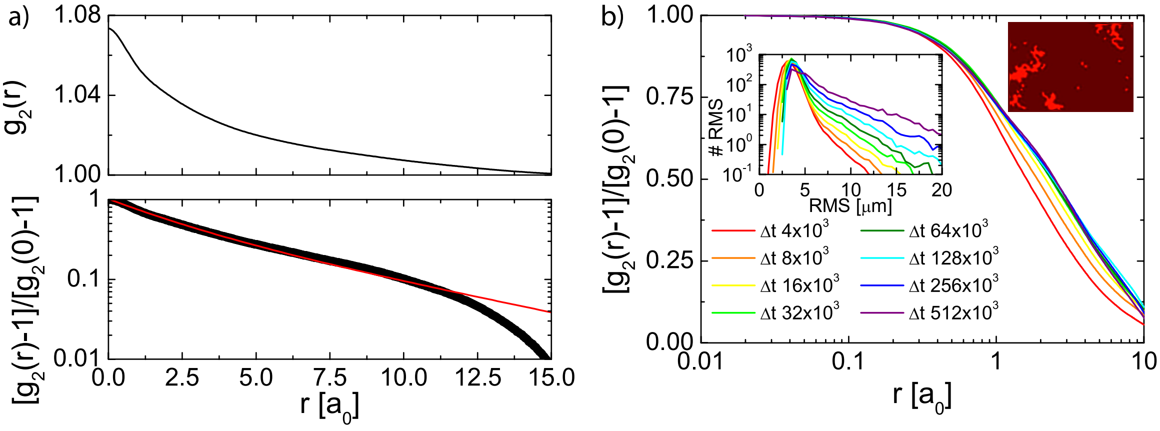

Figure 5.6.: **RMS spatial correlation function $g_2(r)$ for $\Gamma = 200$.**
a) (Top graph) $g_2(r)$ exhibits the features of a typical normalized intensity autocorrelation function with an intercept between 2 and 1. (Bottom graph) The normalized $g_2(r)$ in a half logarithmic representation exhibits a double exponential decay over some average interparticle distances. The red line is a fit. For details, see text.
b) Normalized RMS autocorrelation function for different time windows Δt. The curves show convergence towards averaging times between $32 \cdot 10^3$ and $128 \cdot 10^3$ seconds. The first inset (top left) shows the distribution of the averaged RMS which exhibits an exponential tail. The second inset (top right) is an extrapolation of RMS, where only particles contributing to the tail were taken into consideration.

a Gaussian distribution. For convenience, $g_2(r)$ is always plotted as $\frac{g_2(r)-1}{g_2(0)-1}$ in the following, thus normalized in a fashion similar to the Siegert relation. In a plot with logarithmic y-axis (figure 5.6.a) bottom graph), $g_2(r)$ exhibits a double exponential decay for a length up to ten interparticle distances. This is indicated by the red line which is a three parameter fit to the data. The model used here is given by $f(x) = A\left[\exp\{-\frac{x}{r_1}\} + \exp\{-\frac{x}{r_2}\}\right]$ with the resulting fit parameters $A = 0.51$, $r_1 = 1.86$ and $r_2 = 6.42$. In both cases, the fit accuracy is better than 99 %. The deviation of the model from the data for $r \geq 10\, a_0$ is not as severe as it seems on the first glance, but merely a consequence of the logarithmic representation. For the correlation length obtained by the fit, the model is in very good agreement with the data and can be made even better if only the region up to $r = 10\, a_0$ is fitted. To understand the existence of two correlation lengths rather than a single one, it is instructive to take another look at the snapshots in figure 5.4. As already discussed, ‘single events’ occur, where two particles exchange positions. These are visible in graph a) as pairs of enlarged blue blobs. Obviously, because of the increased dynamics far above average, these particles contribute well to the RMS. The respective correlation length, however, only extends as far as two interparticle distances (the distance between the two particles plus two times half the distance to their respective neighbors), which is in agreement with the fit parameter $r_1 = 1.86$. As mainly small particles (blue color code) are involved in this procedure, the decay length r_1 may be attributed to a structural feature generic to systems with soft long ranged interactions. Previous works found a clustering of small particles at the vertices of the Voronoi cells of big particles [Ebe08b, Ebe09b]. Because the interaction energy between two small particles is 100 times less than between two big particles, this particular (static) structural arrangement allows for the described specific rearrangement mechanism responsible for the twofold exponential decay of the normalized RMS spatial correlation function.

The second decay length $r_2 = 6.42$, on the other hand, represents the extension of the much larger dynamically active areas. This gives some quantitative measure of the size of the dynamical heterogeneities in the system. As can be seen from figure 5.4, they extend indeed some couple of interparticle distances. However, the heterogeneities appear in rather irregular shapes, some of them being more compact while others take elongated forms. Thus, the correlation length r_2 only describes some average size. Nevertheless, it should quantify the system characteristically for a given temperature.

Finite time effects

Before the temperature dependence of r_2 is addressed, some attention should be payed towards the finite time behavior of the normalized RMS spatial correlation function. As already discussed when introducing $g_2(r)$, it is not only dependent on the time t (the heterogeneities are not static), but also on the time window Δt which is used to calculate the intermediate particle positions and the respective RMS. Therefore, Δt was varied for the data set of $\Gamma = 200$. The resulting correlation functions are shown in figure 5.6.b). For short time windows (red, yellow and orange colored curves), the heterogeneities appear smaller as $g_2(r)$ decays faster. This phenomenon is due to 'cooperative rearrangements' occurring on a slower timescale, because heterogeneous dynamics involve the shift of average particle positions. From figure 5.4 it is evident that the strongest 'cooperative rearrangements' occur in the center of the heterogeneities, and are gradually ebbing out towards the edges. Consequently, very small displacements at the 'edges' of heterogeneities can not be properly resolved within short time windows because they are buried by the homogenous background noise. The shorter the time window, the more of the dynamically active regions is 'melted' away.

For longer time windows up to $512 \cdot 10^3$ seconds, the curves converge. On this time scale, the size of the heterogeneities is not affected by the choice of Δt. Merely, the difference in RMS between particles belonging to a rearranging region and those who do not becomes smaller, because dynamically active times start to be averaged out. For the time windows shown in figure 5.6.b) this does not yet occur, but for longer

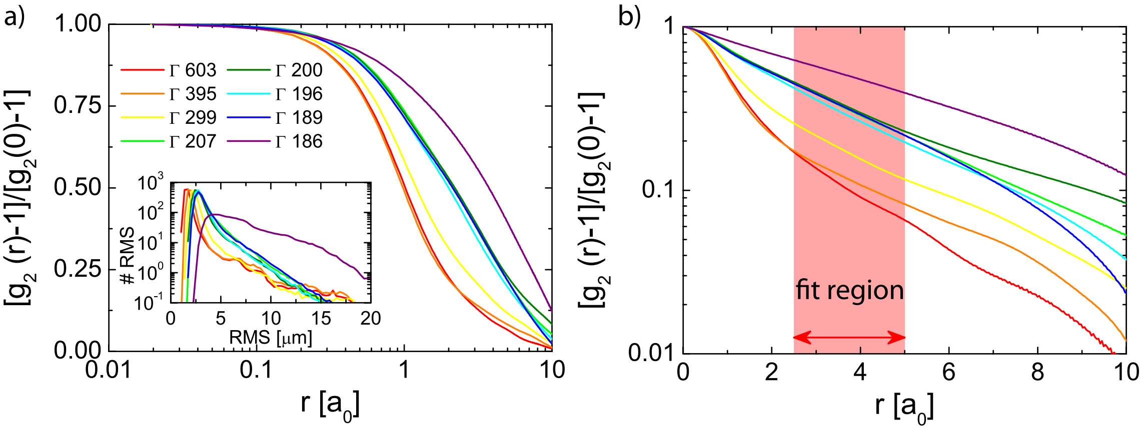

Figure 5.7.: **Lengthscale of dynamic heterogeneities.**
a) Temperature dependence of the normalized RMS spatial correlation function. The inset shows the respective RMS distribution.
b) $g_2(r)$ in a log-lin representation to clarify the decay stages. The correlation length is obtained by a fit in the shaded region.

times it becomes more and more difficult to distinguish between fast and slow dynamics. Eventually, a homogenous distribution is expected because all dynamics will be averaged out for $\Delta t \to \infty$.
The inset of figure 5.6.b) shows the distribution of RMS for the different time windows discussed above. It exhibits an exponential tail towards large RMS, which grows for larger Δt as expected. As it turns out, the dynamical heterogeneities are composed of particles with an RMS contributing to the tail. In other words, the exponential tail in the RMS distribution is a signature of dynamical heterogeneity. This illustrates the argument that for large Δt, RMS values belonging to heterogeneities become indistinguishable from those who do not, because eventually the whole distribution contributes to the tail. The extrapolated RMS distribution for only those particles of the tail is shown in the second inset of figure 5.6.b). It shows the same dynamically active regions as figure 5.5.a). Because of a different mean RMS value, the normalization has slightly changed such that the image appears much smoother.

Temperature dependence

The technique developed in the last paragraphs was applied to data at different temperatures. As expected, the spatial expansion of dynamical heterogeneities is directly affected by the resulting rigidity of the system. Coming from the deeply frozen state, figure 5.7.a) indicates that dynamically active regions grow in size upon approaching the melting point as the curves for higher temperatures shift to the right. It is note-

worthy that the data fall in basically one of three categories. Deep in the glassy state (i.e. $\Gamma = 603, 395$), it is difficult to distinguish between the different $g_2(r)$, i.e. the structure of dynamics does not change much. Upon lowering the particle interaction energy down to the glass transition (compare chapter 3), the curves begin to loose their characteristic s-shape (which is responsible for the two step decay and resulting in two distinct correlation length r_1 and r_2). For $\Gamma = 207 - 189$, the curves are largely indistinguishable in the present representation. The last curve at $\Gamma = 186$ then extends significantly further to the right, although Γ has only decreased by a value of $\Delta\Gamma = 3$. This indicates a considerable jump in the average size of dynamical heterogeneities and is investigated further below.
The inset shows the respective RMS distribution. As expected, its peak shifts to larger values for increasing temperature (decreasing Γ). This reflects the growth of thermal vibrations. An interesting feature to note is the increase in particles contributing to the exponential tail, which is a natural consequence of growing heterogeneities. Strikingly, the curve for $\Gamma = 186$, which lies at the verge of the transition, has a significantly different shape compared to the ones deeper in the glassy state as basically all particles have started rearranging. This is in accordance to figure 5.3.b).

Figure 5.7.b) presents the same data as figure 5.7.a) with logarithmic y-axis to identify the decay behavior. As in a), the high Γ curves somewhat collapse, as do the curves around $\Gamma = 200$. They start to deviate at about six interparticle distances. This reflects an inaccuracy of the method, which implicitly assumes a spherical shape of the heterogeneities. In the extrapolation and successive averaging steps, the true fractal nature (apparent from the snapshots in figures 5.3 and 5.4) is lost. Considering the limited field of view which only captures a small number of dynamically active regions, the statistics for larger correlation distances are sparse. Thus, any erratic behavior in this region should be no surprise. Therefore, the attention is focused on distances $r \leq 5\, a_0$.
Coming from the arrested state, the remarkable step exponential decay is well visible. It vanishes upon entering the vicinity of the transition temperature. As the cause of this first decay was identified with small particles interchanging their positions, it may be derived from this data that this mechanism is absent at high temperatures, although it might be simply hidden beneath the overall increased dynamics. In either case, this first decay in $g_2(r)$ is not caused by the spatial extension of dynamically active regions. To extract those, the curves are fitted with a single exponential $f(x) = A \cdot \exp\{-\frac{x}{\xi}\}$ in the region indicated by red shading. This restricts the fit to a lengthscale above the first decay at higher Γ but below the erratic deviations at larger r.

In figure 5.8, the correlation length ξ, which determines the average size of the dynamical heterogeneities, finally is presented. It is extracted from $g_2(r)$ by a fit. Details to this procedure are given below. Coming from low temperatures, ξ increases moderately down to $\Gamma = 189$. Here, it suddenly ramps up severely. This marks the

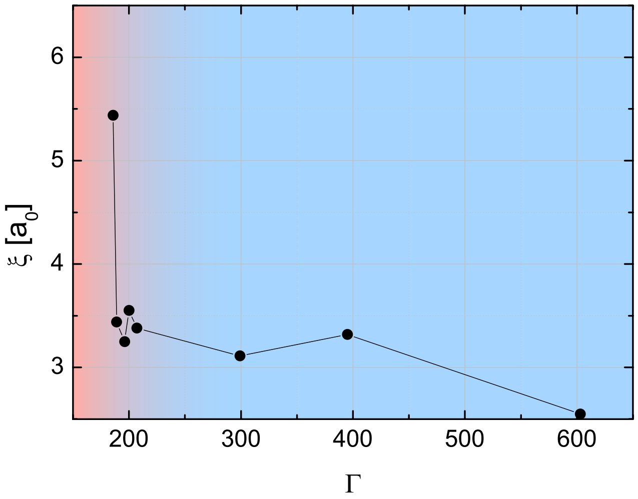

Figure 5.8.: **Correlation length of dynamical heterogeneities.**
Correlation length ξ for different temperatures extracted by fitting a single exponential to the middle part of $g_2(r)$. Shading distinguishes between ergodic (red) and non-ergodic (blue) state.

transition from the dynamically arrested to the ergodic state, which is indicated by the underlying shading (red = fluid, blue = arrested).

The finite size of the field of view and the consequential limited number of observable heterogeneities is also held responsible for the non-monotonic behavior of $\xi(\Gamma)$. The overall trend, however, which indicates a slow increase of ξ up to the transition temperature becomes clear from the data. The sudden growth at $\Gamma = 186$ also lies beyond any statistical error.

5.2.2. Discussion

As it turns out, the experiments conducted in this thesis suggest a growing lengthscale in spatio-temporal dynamics upon approaching the glass transition temperature from the frozen state. This finding is exceptional in a sense that the literature is usually concerned with regarding the transition from the fluid side, where such a growing lengthscale is discussed. The nature of the experiment and the corresponding measurement time scale demanded by the technique developed in this chapter make it *very* hard to tackle the problem on the fluid side.

As mentioned in the introduction, the theoretical framework of critical fluctuations and continuous phase transitions demands the discussed lengthscale to diverge. The results of this chapter can not support this claim due to several reasons. First, because the final, crucial increase in $\xi(\Gamma)$ is only represented by a single data point, a statement about the nature of this growth can not be made. Second, the peak height, although representing a 60 %-increase above the preceding values, only measures about 100 micron, that is 6 % of the diameter of the field of view. On this note, it is questionable to which extend the limitations of the field of view allow to grasp the explosive spatial expansion of dynamical heterogeneities in the first place. A true divergence, caused by fluctuations on *all length scales*, would imply a growth up to the lengthscale of the whole sample, which obviously can not be resolved with the much smaller dimensions of the camera chip. In fact, if the correlation length exceeds the field of view, the local dynamics would appear homogenous again. This limits the measurable correlation length to a fraction of the field of view, and evidence for diverging behavior can only be derived from the shape of the growth. Because the accuracy of temperature for the binary system only lies within ± 3 units of Γ, a higher temperature resolution than achieved here already is not feasible.

In conclusion, the data acquired in the scope of this thesis prove the existence of dynamics heterogeneously distributed in space-time. Established approaches via the overlap function $Q_4(t)$ and the corresponding susceptibility $\chi_4(t)$ allow the estimation of a time scale for the lifetime of these heterogeneities. The development of a novel approach utilizing correlation techniques from scattering physics revealed their lengthscale, which was found to be growing in the vicinity of the glass transition. However, statements about the strength of the growth could not be made due to experimental restrictions.

6. Measurements on substrates

As a side project, some measurements have been conducted on solid substrates (compare section 2.3.2). Compared to droplet experiments, first attempts with monodisperse systems showed a significantly improved steady state with drift rates lower more than an order of magnitude [Deu13b, Pol14]. On a first glance, this makes these types of system ideal to tackle the glass transition from the fluid side, because it becomes very easy to conduct long-time measurements even in the nonergodic state. These data would provide a rounded picture of the density of states below T_G. On the other hand, the influence of pinning or the altered bead dynamics above a surface might bias the data, especially the studies of vibrational phenomena, which is a interesting physical perspective in itself.

6.1. Dynamics on substrates

First of all, the handling of pinned particles has to be determined. Similar to the method described in [Wil12, Deu13a], immobile beads were identified by their area coverage[1] in trajectory space, i.e. a circle covering the trajectory for every particle was constructed. The corresponding distribution of (trajectory) diameters is shown in figure 6.1.a) for the system at $\Gamma = 192$. It exhibits a pronounced maximum between 10 and 15 μm, with a tail towards larger diameters for a measurement of $T \approx 3500$ seconds. For smaller trajectories, the distribution decays rapidly, marking the immobility of pinned particles. This is indicated by red shading. The inset shows a small part of the field of view containing some exemplary trajectories for 3500 seconds. Two of those only appear as small dots because of their binding to the substrate. The rest can diffuse rather freely, resulting in a large area coverage. This is indicated by the green circle, the diameter which contributed to the main figure. By setting a cutoff value (here: 7 μm) excluding contributions to the left hand of the distribution's flank, pinned particles were determined. For different measurements at varying interaction strength, the cutoff value had to be carefully tuned. A 'pinning strength' of about 1.25 % of rather immobile particles was found for all data acquired on the substrate. It has to be considered that the pinning fraction of particles is not unambiguously separable from the mobile ones. Even perfectly immobile particles have a finite area coverage due to overlapping effects of finite optical resolution, electronic noise of the

---

[1] 'Area coverage' means the area a particle diffuses over in a given amount of time. In other words, it is the lateral extension of its trajectory.

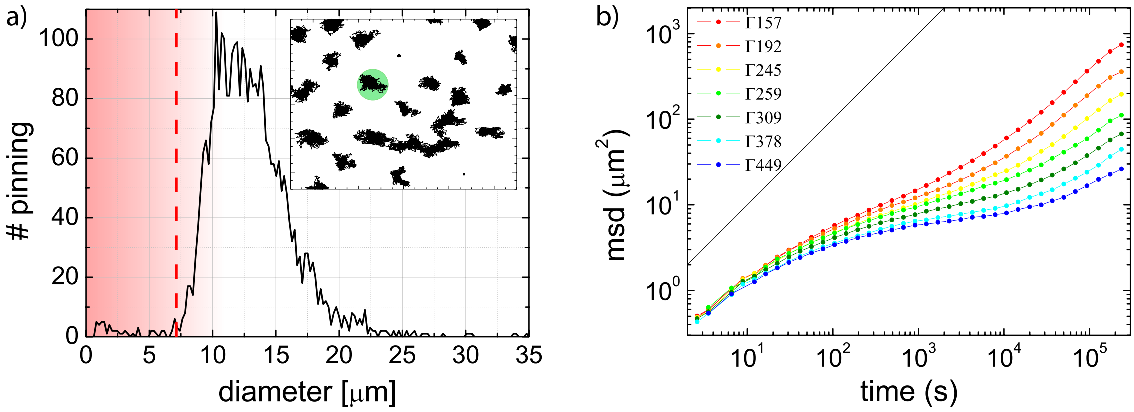

Figure 6.1.: **Dynamics on solid substrates.**
a) Distribution of trajectory diameter for $\Gamma = 192$ after $T \approx 3500$ seconds. The red shading indicates pinning particles, the cutoff is given by the red dashed line. Inset: Trajectories including two pinning particles. The green circle exemplary indicates the area coverage of an unbound particle.
b) As in the ideal system without substrate interaction, $\langle \Delta r^2(\tau) \rangle$ develops a shoulder for increasing interaction strength, which crosses over into a plateau marking dynamical arrest. The quality of the data enables the unambiguous identification of a decreasing plateau value for lower temperatures.

CCD and intensity fluctuations (to which also the constantly rearranging environment contributes, causing differences in mutual illumination). Yet, diameters of $5\,\mu$m and above can not be explained by mere noise. Rather, it seems that certain bounds are 'flexible' to some extend, such that affected particles perform Brownian motion but are constricted to a very localized portion of the sample. Apparently, those particles are anchored to the substrate in some way. This binding mechanism is not understood, but might be due to some flexible polymer linking the bead to the substrate. Further, it was observed that in some cases, the bonds are not permanent, i.e. particles may break free from or become trapped by the surface after a finite amount of time. This makes it somewhat difficult to unambiguously distinguish between free and pinned particles, and the method presented here turns out to be the best shot. On this account it is noted that different mobility criteria were tested, the trajectory diameter being one of them. Integrated mean squared displacements and box area (covering trajectories in rectangles rather than circles) yielded a nearly identical distribution and hence similar results.

In figure 6.1.b), the mean squared displacement (compare figure 3.6, section 3.2.3) is shown. Contributions of immobile particles were excluded as described above. The

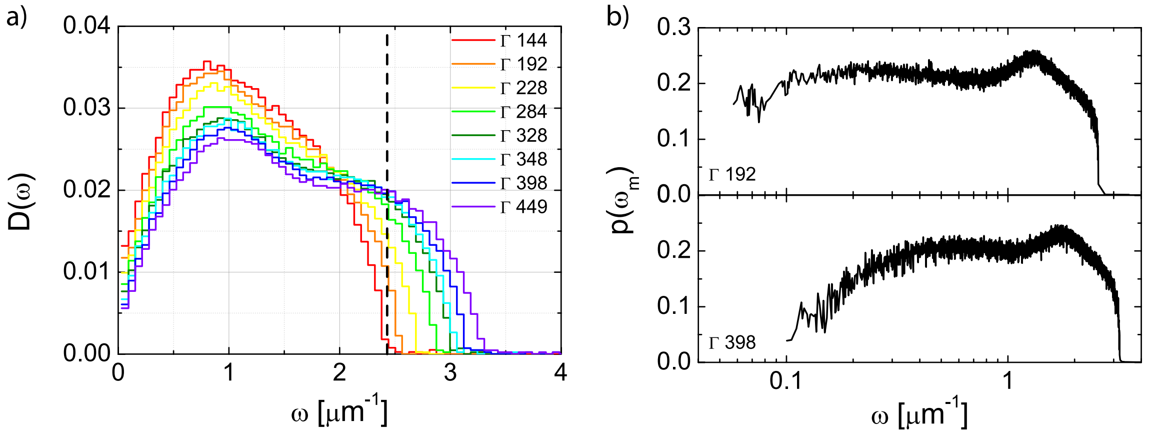

Figure 6.2.: **Density of states on substrates.**
a) The decreasing temperature facilitates the formation of a second peak in the distribution of inverse eigenvalues of the covariance matrix. This result is identical to the substrate-less case.
b) Participation ratio of modes in the supercooled and frozen state.

data is of remarkable quality, exhibiting a continuous decrease of the plateau value for increasing interaction strength, accompanied with a delayed onset of alpha relaxation. This illustrates the physical picture of a rising number of caged particles, where the cage size simultaneously shrinks.

6.2. Vibrations on substrates

To study the influence of a solid substrate and pinning particles on vibrational excitations , trajectories of $N = 2200$ particles in $N_\tau = 6 \cdot 10^4$ frames covering a measurement time of $T = 2 \cdot 10^5$ seconds were evaluated. Again, immobile particles were excluded prior to any analysis. From this data, the covariance matrix C_{ij} was computed and diagonalized. Concerning the statistics, it was found $r = 2N/N_\tau \approx 0.07$ which is low enough to yield converging results (compare section 4.2.1). Considering the slower dynamics, the averaging window was chosen to 8000 seconds, although this quantity has little influence on the resulting distribution of inverse eigenvalues (compare section 4.2.1). The corresponding spectrum is plotted in figure 6.2.a) for varying temperatures, ranging from fluid $\Gamma = 144$ to deeply frozen $\Gamma = 449$. The data shows the development of a shoulder upon increasing interaction parameter, bestowing a shape to the spectrum similar to that in section 4.2.1. The main difference, however, is that the shoulder does not evolve further into a peak; the discussed Van Hoove-type singularities are less pronounced in this case.

The dashed vertical line marks the limit of physical relevance, above which the product of fluctuations in C_{ij} becomes smaller than the optical resolution, thus attributing

this part of the spectrum to noise.
Figure 6.2.b) presents the participation ratio $p(\omega_m)$ of modes in the supercooled $\Gamma = 192$ and glassy $\Gamma = 398$ state. Intriguingly, the distribution decays for low frequencies, indicating a localization. This is contradictory to the results in chapter 4.2.1. There, an increase of $p(\omega_m)$ was found which indicated correlation of the mode patterns. This was attributed to the plane wave character of long wavelength excitations. Stunningly, the disordered nature of modes on a substrate becomes more pronounced upon cooling.

Now, the structure of the modes contributing to the density of states is analyzed in more detail. In figure 6.3, the eigenvectors corresponding to the most principal component of the spectrum at different temperatures are shown. Arrows correspond to amplitudes of particles in this particular mode, and red dots indicate the position of pinned particles. On the fluid side (graphs a) and b), $\Gamma = 144, 192$ respectively), the mode structure appears largely uncorrelated, in amplitude as well as in orientation. This is equivalent to the findings in chapter 4, where the system below $\Gamma = 185$ exhibited 'swirling motions' that are largely uncorrelated at larger lengthscales (compare figure 4.6). Quite natural, the low interaction strength does not support the propagation of well-polarized elastic excitations. For increasing interaction strength in the glassy state, the orientational correlation increases, but never becomes comparable to the extension found in the system supported by the water-air interface. Additionally, increasing localization is found in this temperature range even for low frequency excitations indicated by the clustering of large arrows. This illustrates the findings of the participation ratio above.

While the occurrence of immobile, yet interacting particles most likely contributes to the less coherent nature of the mode patterns identified here, there might be even more generic mechanisms at work. Since the dynamics of a bead in front of a wall scale with the distance and Brownian motion probes a portion of elevations [Pri90b, Pri90a], the displacement field determining the components of the covariance might be biased. To some extend, this can be compensated by using a large averaging window Δt. However, since this effect is supposed to be spatially heterogeneous due to non-uniform surface and particle charge distributions [vG01], a residual bias will always remain.
Depending on the lengthscale of this chemical inhomogeneity, diffusion of particles might also happen in an Arrhenius-like fashion, such that particles need (thermal) activation energy to propagate from one place to another, resulting in a ratchet-like motion. With sufficient resolution to pick up this effect, it would again bias the displacement field very strongly.

To probe these influences on the analysis described in chapter 3, the dispersion relations for strictly plane wave like excitations were calculated. Figure 6.4.a) shows longitudinal (filled symbols, top) and transverse (empty symbols, bottom) bands. Due

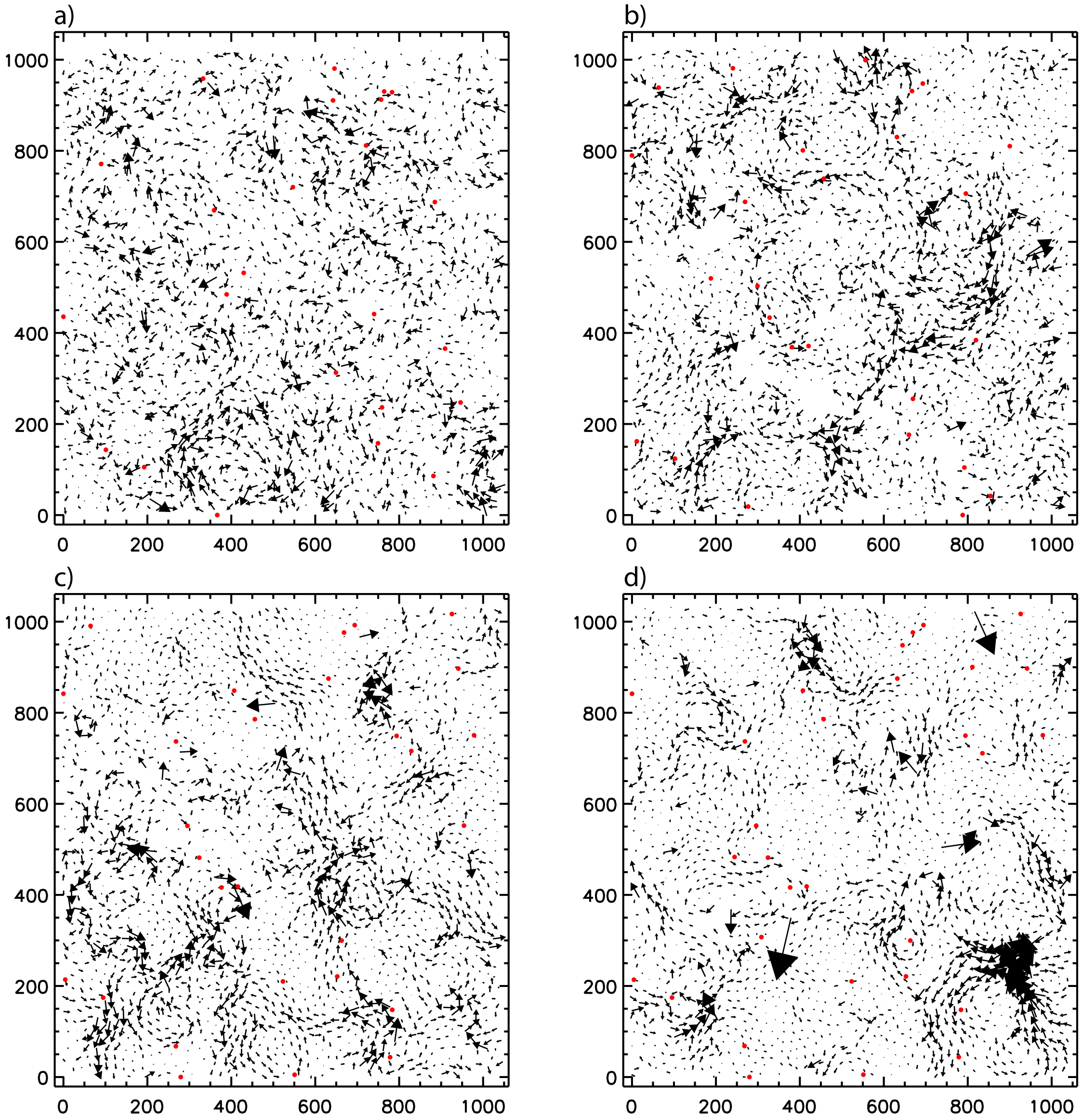

Figure 6.3.: **Mode structure on substrates.**
The eigenvector structure of the most principal component is shown for a) $\Gamma = 144$, b) $\Gamma = 192$, c) $\Gamma = 259$ and d) $\Gamma = 398$. Red dots indicate the position of pinned particles.

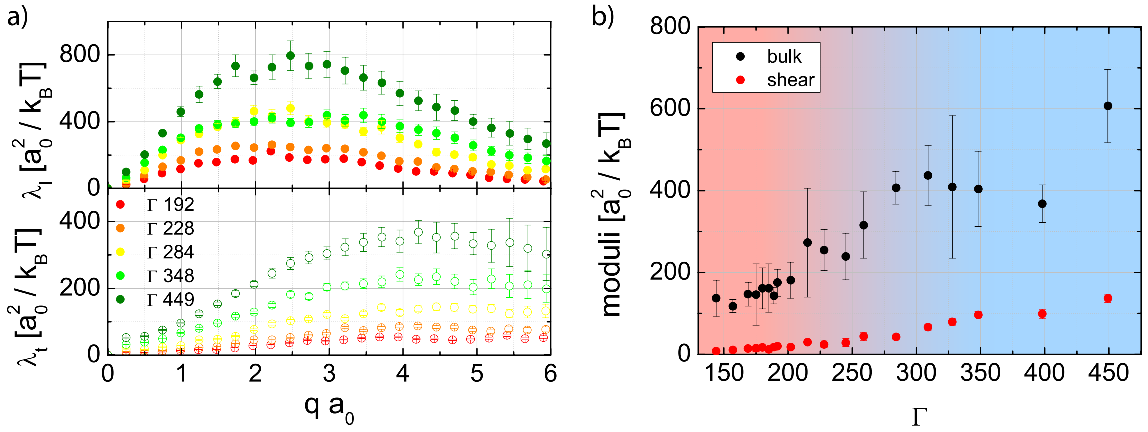

Figure 6.4.: **Displacement field analysis on substrates.**
a) Dispersion bands for longitudinal (filled symbols, top) and transverse (empty symbols, bottom) excitations. The data is noisy (not visible in this representation due to scaling) and does not exhibit Debye behavior.
b) Temperature dependent elastic moduli. The transition from liquid to solid appears continuous, as indicated by the shading.

to scaling, the roughness of the curves is not visible very well. However, it becomes apparent in graph b) where the subsequently extracted moduli are plotted. As a consequence, this data gives no indication about a discontinuous transition from the liquid to the solid state, i.e. on solid substrates, the transition appears continuous.

6.3. Discussion

In summary, it becomes clear that solid substrates are inferior to the water-air interface when it comes to the study of long-ranged vibrational excitations. Pinning and/or profound hydrodynamic interactions severely influence the propagation of modes and effectively induce scattering even at longer wavelengths. Therefore, any well-defined polarization is lost. As a result, the structure of modes as determined by PCA shows a lack of coherence but strong localization. While it seems intuitive that immobile particles facilitate the latter phenomenon, it must be pointed out that figure 6.3 does not show such a correlation directly.
This might also concern results on the density of states of colloidal systems obtained by other groups [Che10]. There, the proliferation of low frequency modes in the spectrum might also be caused by the substrate influence, as those modes appear to be of non-planar nature. This affects the discussion about the notorious boson peak, because the results of this thesis deliver evidence for a non-universal vibrational behavior of glassy two-dimensional colloidal systems.

These results underline the importance of interfaces in two-dimensional systems. In order to facilitate unperturbed mode patterns, i.e. provide the necessary wave front stability in the long wavelength limit, lateral interactions between particles and substrate should be minimized. This may be realized by deploying a water-air interface, which conveyed a coherent picture of long-ranged vibrational excitations in chapter 3 and 4.

Conclusion & Outlook

In this thesis, experiments were performed on a colloidal glass former. Two species of superparamagnetic polystyrene beads (diameters $\sigma_B = 4.5\,\mu\text{m}$ and $\sigma_S = 2.8\,\mu\text{m}$) were confined by gravity on a completely flat water-air interface, providing an almost ideal two-dimensional system. Thermal excitations perpendicular to the plane are only of a few *per mille* of the particles' diameter, and in-plane particle-substrate interactions are absent. The dipolar pair interaction between particles is tunable via an external magnetic field, enabling an *in situ* control of the effective system temperature and providing the interaction energy between all particles at all times. A sophisticated computer program autonomously controls the setup, keeping the system in a metastable state for times up to several months. Video microscopy allows for the continuous tracking of ≈ 2000 particles up to 10^6 seconds (almost 12 days).
Complementary experiments have been conducted on solid substrates with the goal of providing even more stability for measurements in the fluid phase. To reduce pinning strength and provide a chemically homogenous background, measurement cells were spincoated with PMMA. To avoid oxidation of superparamagnetic beads by UV-glue, the cells were sealed in two consecutive steps.

It is generally acknowledged that glasses in two dimensions behave like their three-dimensional counterparts. Nevertheless, there might be yet undocumented phenomena specific to monolayers, for example long-ranged Mermin-Wagner fluctuations. Results of the present thesis highlight the intrinsic influence of the substrate, which possibly alters the system's behavior dramatically.

In both studied cases (solid and water-air interface), the system exhibited a slowing down of dynamics with increasing interaction parameter, as indicated for instance by the mean squared displacement. The emergence of a plateau marked dynamical arrest, typical for (disordered) solids. At the same time, the amorphous structure of a fluid was preserved.

Experimental data was acquired for different temperatures to study the emergence of rigidity at the glass transition. By defining and analyzing the displacement field of thermal vibrations in Fourier space, dispersion relations of acoustic waves were extracted. This effective plane wave approximation is expected to hold in the long wavelength limit, where the local disorder of the system becomes negligible. Isotropy was exploited to enhance statistics, resulting in very smooth data and allowing a pre-

cise extrapolation towards infinite wavelength ($q \to 0$). This yields the macroscopic elastic response by virtue of continuum elasticity theory. The high stability of the sample (i.e. strikingly low collective motion like drift) allowed for a precise determination of the glass transition temperature $\Gamma_G = 197 \pm 5$ by finding a sharp onset in the temperature-dependent shear modulus μ. This confirms a discontinuous transition scenario, in accordance with simulation and theoretical work recently published.
In a further analysis of the method applied here, finite time behavior was tackled, showing striking stability of the shear modulus. The emerging plateau extends into times in the alpha relaxation regime, i.e. times where structural relaxation and Mermin-Wagner fluctuations kick in. This was attributed experimentally to the comparatively large amplitude of shear waves, such that the corresponding wavefronts are less likely to be deformed by local disorder of the system. Both bulk and shear modulus exhibit an algebraic scaling for high frequencies, which is not yet theoretically described.

Vibrational excitations were tackled further in a principal component analysis (PCA), a tool gaining recent attention in colloidal systems. By calculating the covariance matrix from the particle displacement field, modes are accessed by its eigenspectrum. Measurements providing outstanding statistics ($38 \cdot 10^4$ configurations) could provide evidence for two peaks in the resulting density of states, which are identified as residues of Van Hove singularities. Upon decreasing the interaction strength, the second peak vanished, attributed to the failing support for shear waves. Interestingly, no evidence for an excess of low frequency modes in the density of states was found at any temperature, a feature commonly seen in atomic and molecular glasses at low temperatures and recently reported to exist in colloidal glass formers as well.
By analyzing the eigenvector structure of the covariance matrix, the mode pattern could be visualized. For the most principal components of the covariance matrix, it becomes evident that the system promotes highly correlated motions at long wavelength, capturing the plane wave character in the continuum limit. These results further validate the Fourier approach to elasticity discussed in the last paragraph, which rounds up the image of vibrational excitations in the system.
Effort was put into the connection of dispersion data with the covariance eigenspectrum, yielding a distribution governed by two Van Hove singularities originating from the vanishing sound velocities at the Brillouin zone edge in both cases. The cumulative density of states showed good agreement in the low frequency region. Both data follow the Debye model very well, again highlighting the continuum character of the soft dipolar system.

Additionally, the phenomenon of heterogeneous dynamics was studied. Utilization of an overlap order parameter $Q_4(t)$ and the associated four point density correlation susceptibility $\chi_4(t)$ hinted towards a timescale of possible spatial correlation roughly between $4 \cdot 10^3$ and $4 \cdot 10^5$ seconds. In the experiments of this thesis, long-time data was used to calculate the root mean square of vibrational amplitudes, a quantity which showed spatio-temporal fluctuations on timescales of the order of $6.4 \cdot 10^4$ seconds, in good agreement with the $\chi_4(t)$ data. Extrapolation onto a regular grid and subsequent application of correlation methods known from light scattering experiments suggested a growing length scale of fractal regions exhibiting increased dynamical activity in the vicinity of the transition temperature Γ_G. Yet upon melting the system from the non-ergodic state, no evidence for critical behavior was found.

Finally, attempts were made to study the glass transition on solid substrates with a pinning strength of about 1 %. The Fourier displacement field analysis could not locate the transition temperature unambiguously. Within the given resolution, the discontinuity was not detectable. Studying the mode structure by PCA, it became apparent that even in the long wavelength limit, clean plane waves are not supported. This effect is believed to be caused by the presence of the substrate, e.g. by pinning facilitating localization. This might explain the discrepancy found in the density of states reported by other groups. In turn, this yields evidence that the notorious excess modes often discussed are not as universal as widely believed and motivates once again the tremendous experimental effort undertaken to produce a water-air interface without lateral interactions. Hence, the experiments on colloidal monolayers performed here are unrivaled worldwide and present the best realization of a quasi two-dimensional system.

In this regard, it could be interesting to quantify the influence of pinning on the disordered mode structure. For this, new droplet experiments with immobile particles induced by optical tweezers would be required. While clarifying the role of the ‘boson peak’ in two dimensions, these results could also be used to follow a recent approach to the glass transition discussed in the literature [Cam12, Kob13]. There it is proposed to artificially induce static disorder (for example due to pinning) in order to reduce the configurational entropy of the liquid state. It is theorized that this might enable a delay of the glass formation by preventing a premature fall out of equilibrium, such that one would enter a temperature regime close to the Kauzmann temperature T_K. This could allow the study of a transition very similar in nature to the debated thermodynamic one at T_K. The pinning strength proposed are of the order of 20 % which could be realized also on substrates. Considering the improved stability, taking this route might easily be fruitful.

Another intriguing, yet unanswered question is that of hysteresis in the glass transition, commonly associated with the specific heat [Coh79, Jäc86]. The cooling-heating cycle performed in this thesis gives a first clue towards a hysteresis of rigidity as well, where T_G shifts to higher temperatures when coming from the frozen state. The data on this is sparse, however, and this matter would need to be illuminated further in more experiments.

Another approach to study glassy elasticity is to probe excitations of particles from their 'equilibrium position' locally. By taking a triangular set with optical tweezers and rotating it over a defined angle in analogy to a disk in an elastic continuum, the shear modulus may be acquired, because the corresponding relaxation time is dependent on the deformation energy [Wil02]. This results in a idealized shear modulus of a system without any defects and a glass can be regarded as a system consisting of *only* defects, the comparison with the macroscopic shear modulus obtained in this thesis would be interesting. Yet another way to probe rigidity would be to devise micro-rheology experiments, where an object (possibly some particles held together by optical tweezers) is dragged through the colloidal glass, enabling to study compressional and shear-induced rupture on a single particle scale.

As the phenomena accompanying the glass transition are numerous, the experiment described here may be used to study many more of them. In the following, some ideas are sketched without going into much detail. Due to the possible ultrafast regulation of interactions, aging effects could be investigated [vM05, Pra07]. While slow cooling did not provide any evidence on the timescale of weeks, measurements of a fast quench to low temperatures might shed some light on these phenomena. Closely related are memory effects [Jon98, Sas05], implying that structure and dynamics are dependent on the preparation history. This issue could be tackled by measurements quenching Γ over various amounts of time and comparison of the results. Further, experiments could be conducted probing the dependence of the glass transition on confinement [Jac96, Sch04]. The different geometries could be provided again by optical tweezers, effectively pinning down 'walls' of particles. Alternatively, on substrates, desired obstacles (walls, circles, cylinders etc.) made of glass could be simply glued into the cell.

Zusammenfassung

In dieser Arbeit wurden Experimente an einem kolloidalen Glasbildner durchgeführt. Darin werden zwei Arten von superparamagnetischen Polystyrolkugeln (mit Durchmessern $\sigma_B = 4.5\,\mu$m und $\sigma_S = 2.8\,\mu$m) durch Gravitation auf eine Wasser-Luft-Grenzfläche gedrückt. Damit steht ein fast ideales zweidimensionales System zur Verfügung, in dem die thermische Bewegung senkrecht zur Grenzfläche nur wenige Promille des Teilchendurchmessers beträgt und es keinerlei laterale Wechselwirkung mit der Grenzfläche gibt. Durch das Anlegen eines externen Magnetfeldes kann die dipolare Wechselwirkung zwischen den Teilchen *in situ* geändert werden, was einer effektiven Temperaturänderung gleichkommt. Gleichzeitig ist die Wechselwirkungsenergie zwischen den Teilchen genaustens bekannt. Um das System für mehrere Monate in einem metastabilen Zustand zu halten, wird der Versuchsaufbaus durch ein komplexes Computerprogramm automatisiert gesteuert. So werden Videomikroskopiemessungen von 10^6 Sekunden (fast 12 Tage) möglich, in denen über 2000 Teilchen ununterbrochen verfolgt werden können.
Mit dem Ziel einer erhöhten Langzeitstabilität wurden komplementäre Experimente auf festen Substraten durchgeführt, um so umfangreichere Messungen auch in der flüssigen Phase durchführen zu können. Um Pinning zu minimieren und chemische Homogenität zu gewährleisten, wurden die Substrate mit PMMA beschichtet. Oxidation der Teilchen durch UV-Kleber wurde durch eine zweilagige Versiegelung der Messzellen verhindert.

Es ist allgemein akzeptiert, dass Glasbildner in zwei und drei Dimensionen die gleiche Phänomenologie besitzen. Trotzdem sind Einflüsse bisher nicht diskutierter Eigenschaften von Monolagen denkbar. Ein Beispiel hierfür sind Mermin-Wagner-Fluktuationen. Ergebnisse der vorliegenden Arbeit beleuchten den intrinsischen Einfluß des Substrates, der das Verhalten des Systems in einigen Fällen dramatisch verändert.

In beiden untersuchten Fällen (festes Substrat und Wasser-Luft-Grenzfläche) zeigte das System eine Verlangsamung der Dynamik bei steigendem Plasmaparameter, sichtbar z.B. im mittleren Verschiebungsquadrat (MSD). Die Ausbildung eines Plateaus markiert hier den glastypischen dynamischen Arrest. Gleichzeitig wurde die amorphe Struktur der Flüssigkeit konserviert.

Es wurden Daten bei verschiedenen Temperaturen gesammelt, um die Verfestigung

beim Eintritt in den glasartigen Zustand zu studieren. Durch die Definition und anschließende Analyse des von thermischen Vibrationen erzeugten Verschiebungsfeldes im Fourierraum wurden die Dispersionsrelationen von akustischen Phononen gewonnen. Die damit einhergehende implizite Näherung als ebene Welle sollte im langwelligen Limes Bestand haben, wenn die lokale Unordnung des Systems vernachlässigbar wird. Die Isotropie des (zweidimensionalen) Raumes wurde zur Verbesserung der Statistik genutzt, was in deutlich geglätteten Kurven resultierte. Damit konnte eine präzise Extrapolation der Dispersionsrelationen in den langwelligen Limes $q \to 0$ erfolgen, was laut Elastizitätstheorie die makroskopischen elastischen Module liefert. Die hohe Stabilität der Probe, d.h. bemerkenswert niedrige kollektive Teilchenbewegungen wie etwa Drift, ermöglichten eine genaue Ermittlung der Glasübergangstemperatur zu $\Gamma_G = 197 \pm 5$, die durch ein plötzliches Anwachsen des temperaturabhängigen Schermodules gekennzeichnet ist. Der enge Bereich dieses Anwachsens deutet auf ein diskontinuierliches Übergangsszenario hin, welches in jüngst veröffentlichten Arbeiten ebenso von Simulationen gefunden und von theoretischen Überlegungen gefordert wird.
Um die Zuverlässigkeit der hier verwendeten Methode zu überprüfen, wurde der Einfluß endlicher Zeitskalen untersucht. Es wurde eine bemerkenswerte Stabilität des Schermodules gefunden. Das beobachtete Plateau besteht auch in der alpha-Relaxation, d.h. zu Zeiten, in denen strukturelle Relaxation oder Mermin-Wagner-Fluktuationen einsetzen. Dies wird in der verhältnismäßig großen Amplitude von transversalen Scherwellen begründet, so dass die betreffenden Wellenfronten weniger drastisch durch lokale Unordnung deformiert werden. Sowohl Scher- als auch Kompressionsmodul zeigten außerdem ein von der Theorie bisher unbeschriebenes algebraisches Wachstum bei hohen Frequenzen (d.h. im Kurzzeitlimes).

Vibratorische Anregungen wurden darüber hinaus mit der Prinzipalkomponentenanalyse (PCA) studiert. Durch die Berechnung der Kovarianzmatrix aus dem Verschiebungsfeld einzelner Teilchen ergeben sich die einzelnen Schwingungsmoden aus dem Spektrum der Eigenwerte. Messungen mit hohem statistischen Inhalt ($38 \cdot 10^4$ Konfigurationen) ergaben so eine Zustandsdichte mit zwei Maxima, die auf Van Hove-Singularitäten zurückgeführt wurden. Bei abnehmender Wechselwirkungsstärke (steigende Temperatur) verschwand der zweite Peak, was das Zusammenbrechen der Scherstabilität widerspiegelt. Die üblicherweise in atomaren und molekularen Gläsern bei niedrigen Temperaturen gefundene Häufung von niederfrequenten Moden in der Zustandsdichte konnte hier nicht beobachtet werden, obwohl dieser sogenannte “Boson Peak” zuletzt auch in kolloidalen Gläsern identifiziert wurde.
Durch die Analyse der Eigenvektorstruktur der Kovarianzmatrix kann die Modenstruktur visualisiert werden. Aus den Prinzipalkomponenten wurde eine hoch korrelierte Verteilung von Auslenkungen bei langen Wellenlängen deutlich, welche das Verhalten von ebenen Wellen im langwelligen Limes widerspiegelt. Diese Resultate bedeuten auch eine Bestätigung des Fourier-Ansatzes zur Elastizitätsbestimmung im letzten Abschnitt, was das Bild vibratorischer, elastischer Anregungen abrundet.

Weiterer Aufwand wurde betrieben, um die Dispersionsdaten mit dem (inversen) Eigenspektrum der Kovarianzmatrix in Verbindung zu bringen. Die resultierende Verteilung wird in beiden Fällen von zwei Van Hove-Singularitäten dominiert, die durch die verschwindenden Schallgeschwindigkeiten am Brillouinzonenrand verursacht werden. Es zeigte sich, dass die kumulative Zustandsdichte eine gute Übereinstimmung der beiden Ansätze im niederfrequenten Teil des Spektrums ergibt. Beide Kurven reproduzieren das Debye-Modell sehr gut. Dies kehrt abermals den kontinuierlichen Charakter dieses weichen, dipolaren Systems hervor.

Ein weiterer Aspekt dieser Arbeit war die Untersuchung von dynamischen Heterogenitäten. Die Berechnung eines Überlappparameters $Q_4(t)$ und der verwandten Vierpunkt-Dichtekorrelationssuszeptibilität $\chi_4(t)$ deutete auf eine Zeitskala von räumlichen Korrelationen hin, die grob zwischen $4 \cdot 10^3$ und $4 \cdot 10^5$ Sekunden liegt. In den Experimenten dieser Arbeit konnten Langzeitdaten zur Berechnung eines Root Mean Squares (RMS) vibratorischer Amplituden genutzt werden, welches raumzeitliche Fluktuationen auf Zeitskalen der Größenordnung $6.4 \cdot 10^4$ Sekunden zeigt. Dies passt hervorragend in den durch die $\chi_4(t)$-Daten vorausgesagten Rahmen. Extrapolation der RMS-Amplituden auf ein gleichmäßiges Gitter und die folgende Anwendung von Korrelationsmethoden aus der Lichtstreuung ergab die ungefähre Ausdehnung der fraktalen Regionen mit erhöhter dynamischer Aktivität. Die gefundene Temperaturabhängigkeit auf der Glasseite deutete ein Anwachsen der entsprechenden Längenskala in der Nähe der Glasübergangstemperatur an, wobei aber keine Hinweise auf kritisches Verhalten auftraten.

Schließlich wurden noch Versuche, den Glasübergang auf festen Substraten mit einer Pinningstärke von etwa 1 % zu untersuchen, unternommen. Durch die Fourier-Analyse des Verschiebungsfeldes konnte die Übergangtemperatur nicht eindeutig festgelegt werden. Innerhalb der vorhandenen Auflösung ist ein Sprung des Schermodules nicht festzustellen. Eine Analyse der Modenstruktur mit PCA machte deutlich, dass ebene Wellen sogar im langwelligen Limes nicht propagieren. Dies wird als eine Folge des Substrates vermutet, welches z.B. durch Pinning die Lokalisierung von Moden fördert. Dieser Umstand könnte auch die Diskrepanz mit der in anderen Gruppen gefundenen Zustandsdichte erklären. Im Rückschluss liefert dies Hinweise auf eine Nicht-Universalität der oft diskutierten niederfrequenten Überflussmoden und motiviert einmal mehr den immensen experimentellen Aufwand, der betrieben wird, um eine lateral wechselwirkungsfreie Wasser-Luft-Grenzfläche herzustellen. Damit ist die hier beschriebene kolloidale Monolage weltweit konkurenzlos und die beste Realisierung eines quasi-zweidimensionalen Systems.

A. Fourier transformation

A function $f(x)$ can be expanded into a Fourier series:

$$f(x) = \sum_q \psi_q(x) f(q)\,.$$

From this starting point the Fourier transformation equations can be derived. With the same conventions as in [Cha95], they read in two dimensions:

$$\begin{aligned} f(\mathbf{r}) &= AV \int \frac{\mathrm{d}^2 q}{(2\pi)^2} e^{i\mathbf{q}\mathbf{r}} f(\mathbf{q}) \overset{AV=1}{\to} \int \frac{\mathrm{d}^2 q}{(2\pi)^2} e^{i\mathbf{q}\mathbf{r}} f(\mathbf{q}) && \text{(A.1)} \\ f(\mathbf{q}) &= \frac{1}{AV} \int \mathrm{d}^2 r\, e^{-i\mathbf{q}\mathbf{r}} f(\mathbf{r}) \overset{AV=1}{\to} \int \mathrm{d}^2 r\, e^{-i\mathbf{q}\mathbf{r}} f(\mathbf{r})\,, && \text{(A.2)} \end{aligned}$$

where V is the two dimensional volume (area) and A an arbitrary normalization constant of the function $\psi_q(r) = Ae^{iqr}$, which is chosen to be $A = V^{-1}$. For a function $f(\mathbf{r})$ given only on a finite interval $[0, \mathbf{L}]$, the q-values reduce to a discrete set: $q_x = 2\pi/L_x$, $q_y = 2\pi/L_y$. Hence, the integral in reciprocal space transforms into a sum:

$$\int_{V_\mathbf{q}} \frac{\mathrm{d}^2 q}{(2\pi)^2} \to \frac{1}{V} \sum_\mathbf{q}\,.$$

Additionally, for a function $f(\mathbf{R})$ defined only at points on a regular lattice consisting of N points, the integral in real space also transforms into a sum:

$$\frac{1}{V} \int_V \mathrm{d}^2 r \to \frac{1}{N} \sum_\mathbf{R}\,.$$

Swapping the integrals in A.1 and A.2 with the sums, one obtains discrete Fourier transformation equations

$$\begin{aligned} f(\mathbf{R}) &= \frac{1}{V} \sum_\mathbf{q} e^{i\mathbf{q}\mathbf{R}} f(\mathbf{q}) && \text{(A.3)} \\ f(\mathbf{q}) &= v_0 \sum_\mathbf{R} e^{-i\mathbf{q}\mathbf{R}} f(\mathbf{R})\,, && \text{(A.4)} \end{aligned}$$

where $v_0 = V/N$ is the unit volume in real space.
The orthogonality and completeness conditions further deliver two very handy identities:

$$\begin{aligned}
\frac{1}{N}\sum_{\mathbf{R}} e^{i(\mathbf{q}-\mathbf{q}')\mathbf{R}} &= \delta_{\mathbf{q},\mathbf{q}'} \\
\frac{1}{N}\sum_{\mathbf{q}} e^{-i\mathbf{q}(\mathbf{R}-\mathbf{R}')} &= \delta_{\mathbf{R},\mathbf{R}'} \,.
\end{aligned}$$

B. Error calculation

The extrapolation $\mathbf{q} \to 0$ of the dispersion relation results in a statistical error σ. The finite resolution of particle positions, on the other hand, leads to uncertainty δ in the displacement field and therefore in the dispersion relation itself. Consequently, the resulting error in the extrapolated moduli is a composition of both parts and taken into account as follows:

$$\frac{\delta\mu_s}{|\mu_s|} = \sqrt{\left(\frac{\sigma_s}{|\mu_s|}\right)^2 + \left(\frac{\delta\lambda_s}{|\lambda_s|}\right)^2} ,$$

where the index s discriminates between bulk and shear modulus, such that μ_s is the respective moduli and $\delta\lambda_s$ the corresponding systematic error in the dispersion relation.

$\delta\lambda_s/|\lambda_s|$ is determined by simple error progression calculations. First, it is assumed that

$$\frac{\delta\lambda_s}{|\lambda_s|} = \frac{\delta\left\langle|\mathbf{u}(\mathbf{q})|^2\right\rangle}{\langle|\mathbf{u}(\mathbf{q})|^2\rangle} = \frac{\delta|\mathbf{u}(\mathbf{q})|^2}{|\mathbf{u}(\mathbf{q})|^2} .$$

$\langle\ldots\rangle$ denotes the ensemble average (here, in practical terms, the time average). Since the time average results in a statistical error which is accounted for in the extrapolation process, it is neglected here. The absolute value of the complex Fourier transformed displacement field is dependent on two not precisely know quantities, the displacement field $\mathbf{u}(\mathbf{R})$ and the equilibrium position ('lattice site') $\mathbf{R}$. Thus,

$$\delta|\mathbf{u}(\mathbf{q})|^2 = \sqrt{\left(\frac{\partial|\mathbf{u}(\mathbf{q})|^2}{\partial\mathbf{R}}\delta\mathbf{R}\right)^2 + \left(\frac{\partial|\mathbf{u}(\mathbf{q})|^2}{\partial\mathbf{u}(\mathbf{R})}\delta\mathbf{u}(\mathbf{R})\right)^2} .$$

To evaluate this equation, the expression $|\mathbf{u}(\mathbf{R})|^2$ can be separated into real and imaginary part $|\mathbf{u}(\mathbf{q})|^2 = |\frac{1}{\sqrt{N}}\sum\mathbf{u}(\mathbf{R})\exp\{-i\mathbf{q}\mathbf{R}\}|^2 = \mathrm{Re}\{\mathbf{u}(\mathbf{q})\}^2 + \mathrm{Im}\{\mathbf{u}(\mathbf{q})\}^2$ with $\mathrm{Re}\{\mathbf{u}(\mathbf{q})\} = \frac{1}{\sqrt{N}}\sum\mathbf{u}(\mathbf{R})\cos(\mathbf{q}\mathbf{R})$ and $\mathrm{Im}\{\mathbf{u}(\mathbf{q})\} = -\frac{1}{\sqrt{N}}\sum\mathbf{u}(\mathbf{R})\sin(\mathbf{q}\mathbf{R})$. Now, calculating the derivatives is easy:

$$\begin{aligned}
\frac{\partial|\mathbf{u}(\mathbf{q})|^2}{\partial\mathbf{R}} &= 2\,\mathrm{Re}\{\mathbf{u}(\mathbf{q})\}\cdot\left(-\frac{\mathbf{q}}{\sqrt{N}}\sum\mathbf{u}(\mathbf{R})\sin(\mathbf{q}\mathbf{R})\right) \\
&\quad + 2\,\mathrm{Im}\{\mathbf{u}(\mathbf{q})\}\cdot\left(-\frac{\mathbf{q}}{\sqrt{N}}\sum\mathbf{u}(\mathbf{R})\cos(\mathbf{q}\mathbf{R})\right) \\
&= 2\,\mathbf{q}\,\mathrm{Re}\{\mathbf{u}(\mathbf{q})\}\cdot\mathrm{Im}\{\mathbf{u}(\mathbf{q})\} - 2\,\mathbf{q}\,\mathrm{Im}\{\mathbf{u}(\mathbf{q})\}\cdot\mathrm{Re}\{\mathbf{u}(\mathbf{q})\} \\
&= 0
\end{aligned}$$

and

$$\frac{\partial|\mathbf{u}(\mathbf{q})|^2}{\partial\mathbf{u}(\mathbf{R})} = 2\,\mathrm{Re}\{\mathbf{u}(\mathbf{q})\}\cdot\left(\frac{1}{\sqrt{N}}\sum\cos(\mathbf{qR})\right) + 2\,\mathrm{Im}\{\mathbf{u}(\mathbf{q})\}\cdot\left(\frac{1}{\sqrt{N}}\sum\sin(\mathbf{qR})\right).$$

Defining the error of the displacement field as $\delta\mathbf{u}(\mathbf{R}) = \sqrt{(\delta\mathbf{r}(t))^2 + (\delta\mathbf{R})^2} = \sqrt{2}\,\delta\mathbf{R}$, the equation to estimate the systematic error in the dispersion relations reads

$$\begin{aligned}\delta\lambda_s &= \frac{|\lambda_s|^2}{|\mu_s|^2}\sqrt{\left(\frac{\partial|\mathbf{u}(\mathbf{q})|^2}{\partial\mathbf{u}(\mathbf{R})}\delta\mathbf{u}(\mathbf{R})\right)^2} \\ &= \sqrt{8}\left[\mathrm{Re}\{\mathbf{u}(\mathbf{q})\}\cdot\left(\frac{1}{\sqrt{N}}\sum\cos(\mathbf{qR})\right) + \mathrm{Im}\{\mathbf{u}(\mathbf{q})\}\cdot\left(\frac{1}{\sqrt{N}}\sum\sin(\mathbf{qR})\right)\right]\delta\mathbf{R}\,.\end{aligned}$$

To take into account that only an interval $qa_0 \in [0.8, 2.0]$ is evaluated in the extrapolation $\mathbf{q} \to 0$, the uncertainty in the dispersion relation is averaged over in this region.

C. Application of the Wiener-Khinchin-theorem

The Wiener-Khinchin-theorem states that the expected value $E\left[x(t)x^{\star}(t+\tau)\right]$ of a stationary time series $x(t)$ may be given in terms of its power spectrum [Wie30, Khi34]. To prove that an autocorrelation function may be expressed by two consecutive Fourier transformations $\mathcal{F}$, the former is defined as

$$C(\tau) := \int x^{\star}(t)x(t+\tau)\mathrm{d}t\,,$$

while the latter transformation from the freqency domain $x(\nu)$ into the time domain $x(t)$ is conducted as

$$x(t) = \int x(\omega)\mathrm{e}^{-i\omega t}\mathrm{d}\omega\,,$$

where $2\pi\nu = \omega$ was already used. Replacing $x(t)$ in the upper definition yields

$$\begin{aligned}
C(\tau) &= \int\int x^{\star}(\omega)\mathrm{e}^{i\omega t}\mathrm{d}\omega \int x(\omega')\mathrm{e}^{-i\omega'(t+\tau)}\mathrm{d}\omega'\mathrm{d}t \\
&= \int\int\int x^{\star}(\omega)x(\omega')\mathrm{e}^{-i(\omega'-\omega)t}\mathrm{e}^{-i\omega'\tau}\mathrm{d}t\mathrm{d}\omega\mathrm{d}\omega' \\
&= \int\int x^{\star}(\omega)x(\omega')\delta(\omega'-\omega)\mathrm{e}^{-i\omega' t}\mathrm{d}\omega\mathrm{d}\omega' \\
&= \int x^{\star}(\omega)x(\omega)\mathrm{e}^{-i\omega t}\mathrm{d}\omega \\
&= \mathcal{F}^{-1}\left(|x(\omega)|^2\right) \\
&= \mathcal{F}^{-1}\left(|\mathcal{F}(x(t))|^2\right)\,,
\end{aligned}$$

where $\delta(\omega' - \omega)$ is the delta function.

Bibliography

[Abr70] M. Abramowitz and I. A. Stegun. *Handbook of Mathematical Functions with Formulas, Graphs, and Mathematical Tables.* Dover Publications, New York (1970).

[Ada65] G. Adam and J. H. Gibbs. *On the Temperature Dependence of Cooperative Relaxation Properties in Glass-Forming Liquids.* Journal of Chemical Physics **43**, 139 (1965).

[Aki78] H. Akima. *A Method of Bivariate Interpolation and Smooth Surface Fitting for Irregularly Distributed Data Points.* ACM Transactions on Mathematical Software **4**, 148 (1978).

[All99] P. B. Allen, J. L. Feldman, J. Fabian, and F. Wooten. *Diffusions, Locons, Propagons: Character of Atomic Vibrations in Amorphous Si.* Philosophical Magazine Part B **79**, 1715 (1999).

[And95] P. W. Anderson. *Through the glass lightly.* Science **267**, 1615 (1995).

[Ang95] C. A. Angell. *Formation of Glasses from Liquids and Biopolymers.* Science **267**, 1924 (1995).

[Ang00a] C. A. Angell. *Glass Formation and the Nature of the Glass Transition.* In *Insulating and Semiconducting Glasses*, vol. 17 of *Series on Directions in Condensed Matter Physics*, pp. 1–51. World Scientific, Singapore (2000).

[Ang00b] C. A. Angell, K. L. Ngai, G. B. McKenna, P. F. McMillan, and S. W. Martin. *Relaxation in glassforming liquids and amorphous solids.* Journal of Applied Physics **88**, 3113 (2000).

[Ara99] M. Arai, Y. Inamura, and T. Otomo. *Novel dynamics of vitreous silica and metallic glass.* Philosophical Magazine Part B **79**, 1733 (1999).

[Arm89] A. J. Armstrong, R. C. Mockler, and W. J. O'Sullivan. *Isothermal-expansion melting of two-dimensional colloidal monolayers on the surface of water.* Journal of Physics: Condensed Matter **1**, 1707 (1989).

[Ash09a] N. W. Ashcroft and N. D. Mermin. *Solid State Phsysics.* Oldenburg Wissenschaftsverlag GmbH, München (2009).

[Ash09b] D. J. Ashton and J. P. Garrahan. *Relationship between vibrations and dynamical heterogeneity in a model glass former: Extended soft modes but local relaxation.* European Physical Journal E **30**, 303 (2009).

[Bar88] J.-L. Barrat, J.-N. Roux, J.-P. Hansen, and M. L. Klein. *Elastic Response of a Simple Amorpous Binary Alloy near the Glass Transition.* Europhysics Letters **7**, 707 (1988).

[Bar89] J. L. Barrat, W. Götze, and A. Latz. *The liquid-glass transition of the hard sphere system.* Journal of Physics: Condensed Matter **1**, 71637170 (1989).

[Bar94] E. Bartsch, V. Frenz, and H. Sillescu. *The glass transition of colloidal polystyrene micronetwork spheres: a dynamic light scattering study.* Journal of Non-Crystalline Solids **172**, 88 (1994).

[Bay07] M. Bayer, J. M. Brader, F. Ebert, M. Fuchs, E. Lange, G. Maret, R. Schilling, M. Sperl, and J. P. Wittmer. *Dynamic glass transition in two dimensions.* Physical Review E **76**, 011508 (2007).

[Ben84] U. Bengtzelius, W. Götze, and A. Sjolander. *Dynamics of supercooled liquids and the glass transition.* Journal of Physics C: Solid State Physics **17**, 5915 (1984).

[Bre61] H. Brenner. *The slow motion of a sphere through a viscous fluid towards a plan surface.* Chemical Engineering Science **16**, 242 (1961).

[Bri10] C. Brito, O. Dauchot, G. Birolid, and J.-P. Bouchaud. *Elementary excitation modes in a granular glass above jamming.* Soft Matter **6**, 3013 (2010).

[Bro28] R. Brown. *A brief account of microscopical observations made in the months of June, July and August, 1827, on the particles contained in the pollen of plants; and on the general existence of active molecules in organic and inorganic bodies.* Philosophical Magazine **4**, 161 (1828).

[Bub98] R. Bubeck, S. Neser, C. Bechinger, and P. Leiderer. *Structure and dynamics of two-dimensional colloidal crystals in confined geometry.* Progress in Colloids and Polymer Science **110**, 41 (1998).

[Buc86] U. Buchenau, M. Prager, N. Nücker, A. J. Dianoux, N. Ahmad, and W. A. Phillips. *Low-frequency modes in vitreous silica.* Physical Review B **34**, 5665 (1986).

[Cam12] C. Cammarota and G. Biroli. *Ideal glass transitions by random pinning.* Proceedings of the National Academy of Sciences of the United States of America **109**, 8850 (2012).

[Cha95] P. M. Chaikin and T. C. Lubensky. *Principles of condensed matter physics.* Cambridge University Press, Cambridge (1995).

[Che02] Z. Cheng, J. Zhu, P. M. Chaikin, S.-E. Phan, and W. B. Russel. *Nature of the divergence in low shear viscosity of colloidal hard-sphere dispersions.* Physical Review E **65**, 041405 (2002).

[Che10] K. Chen, W. G. Ellenbroek, Z. Zhang, D. T. N. Chen, P. J. Yunker, S. Henkes, C. Brito, O. Dauchot, W. van Saarloos, A. J. Liu, and A. G. Yodh. *Low-Frequency Vibrations of Soft Colloidal Glasses.* Physical Review Letters **105**, 025501 (2010).

[Che11] K. Chen, M. L. Manning, P. J. Yunker, W. G. Ellenbroek, Z. Zhang, A. J. Liu, and A. G. Yodh. *Measurement of Correlations between Low-Frequency Vibrational Modes and Particle Rearrangements in Quasi-Two-Dimensional Colloidal Glasses.* Physical Review Letters **107**, 108301 (2011).

[Coh59] M. H. Cohen and D. Turnbull. *Molecular Transport in Liquids and Glasses.* The Journal of Chemical Physics **31**, 1164 (1959).

[Coh79] M. H. Cohen and G. S. Grest. *Liquid-glass transition, a free-volume approach.* Phys. Rev. B **20**, 1077 (1979).

[Cos10] R. Costi, A. E. Saunders, and U. Banin. *Colloidal Hybrid Nanostructures: A New Type of Functional Materials.* Angewandte Chemie International Edition **49**, 4878 (2010).

[Cou03] E. Courtens, M. Foret, B. Hehlen, B. Rufflé, and R. Vacher. *The crossover from propagating to strongly scattered acoustic modes of glasses observed in densified silica.* Journal of Phsics: Condensed Matter **15**, 1279 (2003).

[Cro96] J. C. Crocker and D. G. Grier. *Methods of Digital Video Microscopy for Colloidal Studies.* Journal of Colloid and Interface Science **179**, 298 (1996).

[Cur02] J. E. Curtis, B. A. Koss, and D. G. Grier. *Dynamic holographic optical tweezers.* Optics Communications **207**, 169 (2002).

[Das91] C. Dasgupta, A. V. Indrani, S. Ramaswamy, and M. K. Phani. *Is there a growing correlation length near the glass transition?* Europhysics Letters **15**, 307 (1991).

[Deb23] P. Debye and E. Hückel. *The theory of electrolytes.* Physikalische Zeitschrift **24**, 185 (1923).

[Deb01] P. G. Debenedetti and F. H. Stillinger. *Supercooled liquids and the glass transition.* Nature **410**, 259 (2001).

[Der41] B. Derjaguin and L. Landau. *Theory of the stability of strongly charged lyophobic sols and of the adhesion of strongly charged particles in solutions of electrolytes.* Acta Physico chemica URSS **14**, 633 (1941).

[Deu13a] S. Deutschländer, K. Franzrahe, B. Heinze, P. Henseler, P. Keim, N. Schwierz, U. Siems, P. Virnau, D. Wilms, K. Binder, G. Maret, and P. Nielaba. *Effects of boundaries on structure formation in low-dimensional colloid model systems near the liquid-solid-transition in equilibrium and in external fields and under shear.* European Physical Journal Special Topics **222**, 2973 (2013).

[Deu13b] S. Deutschländer, T. Horn, H. Löwen, G. Maret, and P. Keim. *Two-Dimensional Melting under Quenched Disorder.* Physical Review Letters **111**, 098301 (2013).

[Dho96] J. Dhont. *An Introduction to Dynamics of Colloids.* Elsevier, Amsterdam (1996).

[Dil08] P. Dillmann, G. Maret, and P. Keim. *Polycrystalline solidification in a quenched 2D colloidal system.* Journal of Physics: Condensed Matter **20**, 404216 (2008).

[Dil11] P. Dillmann. *Nichtgleichgewichts-Phasenübergang eines 2d Kolloidsystems.* Ph.D. thesis, University of Konstanz (2011).

[Dil12] P. Dillmann, G. Maret, and P. Keim. *Comparison of 2D melting criteria in a colloidal system.* Journal of Physics: Condensed Matter **24**, 464118 (2012).

[Don02] C. Donati, S. Franz, S. C. Glotzer, and G. Parisi. *Theory of non-linear susceptibility and correlation length in glasses and liquids.* Journal of Non-Crystalline Solids **307**, 215 (2002).

[Dou72] R. W. Douglas. *A history of glassmaking.* G. T. Foulis & Co Ldt., Henley-on-Thames (1972).

[Dov97] M. T. Dove, M. J. Harris, A. C. Hannon, J. M. Parker, I. P. Swainson, and M. Gambhir. *Floppy Modes in Crystalline and Amorphous Silicates.* Physical Review Letters **78**, 1070 (1997).

[Duf98] E. R. Dufresne and D. G. Grier. *Optical tweezer arrays and optical substrates created with diffractive optics.* Review of Scientific Instruments **69**, 1974 (1998).

[Dun89] G. H. Dunteman. *Principal Component Analysis.* Sage Publications, Thousand Oaks (1989).

[Duv03] E. Duval, L. Saviot, L. David, S. Etienne, and J. F. Jal. *Effect of physical aging on the low-frequency vibrational density of states of a glassy polymer.* Europhysics Letters **63**, 778 (2003).

[Duv04] E. Duval, A. Mermet, R. L. Parc, and B. Champagnon. *About the origin of the boson peak in vitreous silica.* Philosophical Magazine **84**, 1433 (2004).

[Ebe08a] F. Ebert. *Dynamics and structure of a colloidal glass former in two dimensions.* Ph.D. thesis, University of Konstanz (2008).

[Ebe08b] F. Ebert, P. Keim, and G. Maret. *Local crystalline order in a 2D colloidal glass former.* European Physical Journal E **26**, 161 (2008).

[Ebe09a] F. Ebert, P. Dillmann, G. Maret, and P. Keim. *The experimental realization of a two-dimensional colloidal model system.* Review of Scientific Instruments **80**, 083902 (2009).

[Ebe09b] F. Ebert, G. Maret, and P. Keim. *Partial clustering prevents global crystallization in a binary 2D colloidal glass former.* European Physical Journal E **29**, 311 (2009).

[Edi96] M. D. Ediger, C. A. Angell, and S. R. Nagel. *Supercooled Liquids and Glasses.* The Journal of Chemical Physics **100**, 13200 (1996).

[Ein05] A. Einstein. *Über die von der molekularkinetischen Theorie der Wärme geforderte Bewegung von in ruhenden Flüssigkeiten suspendierten Teilchen.* Annalen der Physik **322**, 549 (1905).

[Ell01] M. S. Elliot and W. C. K. Poon. *Conventional optical microscopy of colloidal suspensions.* Advances in Colloid and Interface Science **92**, 133 (2001).

[Far57] M. Faraday. *The Bakerian Lecture: Experimental Relations of Gold (and Other Metals) to Light.* Philosophical Transactions of the Royal Society London **147**, 145 (1857).

[For08] J. Fornleitner, F. Lo Verso, G. Kahl, and C. N. Likos. *Genetic algorithms predict formation of exotic ordered configurations for two-component dipolar monolayers.* Soft Matter **4**, 480 (2008).

[Fra99] S. Franz, C. Donati, G. Parisi, and S. C. Glotzer. *On dynamical correlations in supercooled liquids.* Philosophical Magazine Part B **79**, 1827 (1999).

[Gar02] J. P. Garrahan and D. Chandler. *Geometrical Explanation and Scaling of Dynamical Heterogeneities in Glass Forming Systems.* Physical Review Letters **89**, 035704 (2002).

[Gho10] A. Ghosh, V. K. Chikkadi, P. Schall, J. Kurchan, and D. Bonn. *Density of states of colloidal glasses.* Physcal Review Letters **104**, 248305 (2010).

[Gho11] A. Ghosh, R. Mari, V. K. Chikkadi, P. Schall, A. C. Maggs, and D. Bonn. *Low-energy modes and Debye behavior in a colloidal crystal.* Physica A **390**, 3061 (2011).

[Gib58] J. H. Gibbs and E. A. DiMarzio. *Nature of the Glass Transition and the Glassy State.* The Journal of Chemical Physics **28**, 373 (1958).

[Glo00] S. C. Glotzer, V. N. Novikov, and T. B. Schroder. *Time-dependent, four-point density correlation function description of dynamical heterogeneity and decoupling in supercooled liquids.* The Journal of Chemical Physics **112**, 509 (2000).

[Gol67] A. J. Goldmann, R. G. Cox, and H. Brenner. *Slow viscous motion of a sphere parallel to a plane wall.* Chemical Engineering Science **22**, 637 (1967).

[Gom03] G. Gompper, J. K. G. Dhont, and D. Richter. *Komplexe Materialien auf mesoskopischer Skala: Was ist Weiche Materie?* Physik in unserer Zeit **34**, 12 (2003).

[Gra61] T. Graham. *Liquid Diffusion applied to Analysis.* Philosophical Transactions of the Royal Society London **151**, 183 (1861).

[Gre06] N. Greinert, T. Wood, and P. Bartlett. *Measurement of Effective Temperatures in an Aging Colloidal Glass.* Physical Review Letters **97**, 265702 (2006).

[Gre11] N. L. Green, D. Kaya, C. E. Maloney, and M. F. Islam. *Density invariant vibrational modes in disordered colloidal crystals.* Physical Review E **83** (2011).

[Göt85] W. Götze. *Properties of the Glass Instability Treated within a Mode Coupling Theory.* Zeitschrift für Physik B **60**, 195 (1985).

[Göt09] W. Götze. *Complex Dynamics of Glass-Forming Liquids: A Mode-Coupling Theory.* Oxford University Press, Oxford (2009).

[Haf83] J. Hafner. *Dispersion of collective excitations in a metallic glass.* Journal of Physics C: Solid State Physics **16**, 5773 (1983).

[Hal78] B. I. Halperin and D. R. Nelson. *Theory of Two-Dimensional Melting.* Phys. Rev. Lett. **41**, 121 (1978).

[Han06] J.-P. Hansen and I. R. McDonald. *Theory of simple liquids.* Academic Press, Amsterdam (2006).

[Hed09] L. O. Hedges, R. L. Jack, J. P. Garrahan, and D. Chandler. *Dynamic Order-Disorder in Atomistic Models of Structural Glass Formers.* Science **6**, 1309 (2009).

[Hen89] A. Henglein. *Small-particle research: physicochemical properties of extremely small colloidal metal and semiconductor particles.* Chemical Reviews **89**, 1861 (1989).

[Hen12] S. Henkes, C. Brito, and O. Dauchot. *Extracting vibrational modes from fluctuations: a pedagogical discussion.* Soft Matter **8**, 6092 (2012).

[Hoh67] P. C. Hohenberg. *Existence of Long-Range Order in One and Two Dimensions.* Physical Review Letters **158**, 383 (1967).

[Hov53] L. V. Hove. *The Occurrence of Singularities in the Elastic Frequency Distribution of a Crystal.* Physical Review **89**, 1189 (1953).

[Hul82] H. C. V. D. Hulst. *Light Scattering by Small Particles.* Dover Publications, New York (1982).

[Hur85] A. J. Hurd. *The electrostatic interaction between interfacial colloidal particles.* Journal of Phsics A: Mathematical and General **18**, 1055 (1985).

[Jac96] C. L. Jackson and G. B. McKenna. *Vitrification and Crystallization of Organic Liquids Confined to Nanoscale Pores.* Chemistry of Materials **8**, no. 8, 2128 (1996).

[Jäc86] J. Jäckle. *Models of the glass transition.* Reports on Progress in Physics **49**, no. 2, 171 (1986).

[Jeo87] Y. H. Jeong. *Frequency-dependent shear modulus of glycerol near the glass transition.* Physical Review A **36**, 766 (1987).

[Joh96] W. L. Johnson. *Fundamental Aspects of Bulk Metallic Glass Formation in Multicomponent Alloys.* Materials Science Forum **225**, 35 (1996).

[Joh99] W. L. Johnson. *Bulk Glass-Forming Metallic Alloys: Science and Technology.* MRS Bulletin **24**, 42 (1999).

[Jon98] K. Jonason, E. Vincent, J. Hammann, J. P. Bouchaud, and P. Nordblad. *Memory and Chaos Effects in Spin Glasses.* Physical Review Letters **81**, 3243 (1998).

[Kau48] W. Kauzmann. *The Nature of the Glassy State and the Behavior of Liquids at Low Temperatures.* Chemical Reviews **43**, 219 (1948).

[Kay10] D. Kaya, N. L. Green, C. E. Maloney, and M. F. Islam. *Normal Modes and Density of States of Disordered Colloidal Solids.* Science **329**, 656 (2010).

[Keg00] W. Kegel and A. van Blaaderen. *Direct observation of dynamical heterogeneities in colloidal hardsphere suspensions.* Science **287**, 290 (2000).

[Kei04] P. Keim, G. Maret, U. Herz, and H. H. von Grünberg. *Harmonic Lattice Behavior of Two-Dimensional Colloidal Crystals.* Physical Review Letters **92**, 215504 (2004).

[Kei05] P. Keim. *Schmelzen und Erstarren in zwei Dimensionen.* Ph.D. thesis, University of Konstanz (2005).

[Khi34] A. Khintchine. *Korellationstheorie der stationären stochastischen Prozesse.* Mathematische Annalen **109**, 604 (1934).

[Kli12] C. L. Klix, F. Ebert, F. Weysser, M. Fuchs, G. Maret, and P. Keim. *Glass Elasticity from Particle Trajectories.* Physical Review Letters **109**, 178301 (2012).

[Kön03] H. König. *Mikroskopische Prozesse am Glasübergang einer binären paramagnetischen 2D Kolloidsuspension: Lokal-dichteoptimierte Kristallit-Cluster.* Ph.D. thesis, University of Konstanz (2003).

[Kön05] H. König, R. Hund, K. Zahn, and G. Maret. *Experimental realization of a model glass former in 2D.* The European Physical Journal E **18**, 287 (2005).

[Kob97] W. Kob, C. Donati, S. J. Plimpton, P. H. Poole, and S. C. Glotzer. *Dynamical heterogeneities in a supercooled Lennard-Jones liquid.* Physical Review Letters **79**, 2827 (1997).

[Kob13] W. Kob and L. Berthier. *Probing a Liquid to Glass Transition in Equilibrium.* Physical Review Letters **110**, 245702 (2013).

[Koh00] S. C. Kohn. *The dissolution mechanisms of water in silicate melts; a synthesis of recent data.* Mineralogical Magazine **64**, 389 (2000).

[Kri53] R. S. Krishnan. *The scattering of light in fused quartz and its Raman spectrum.* Proceedings of the Indian Academy of Sciences - Section A **37**, 377 (1953).

[Lac02] N. Lacevic, F. W. Starr, T. B. Schrøder, V. N. Novikov, and S. C. Glotzer. *Growing correlation length on cooling below the onset of caging in a simulated glass-forming liquid.* Physical Review E **66**, 030101 (2002).

[Lac03] N. Lacevic, F. W. Starr, T. B. Schroder, and S. C. Glotzer. *Spatially heterogenous dynamics investigated via a time-dependent two-point density correlation function.* The Journal of Chemical Physics **119**, 7372 (2003).

[Lan95] L. D. Landau and E. M. Lifshitz. *Theory of Elasticity.* Butterworth-Heinemann, Oxford (1995).

[Lem12] C. A. Lemarchand, A. C. Maggs, and M. Schindler. *Elastic fluctuations as observed in a confocal slice.* Europhysics Letters **97**, 48007 (2012).

[Leu84] E. Leutheusser. *Dynamical model of the liquid-glass transition.* Physical Review A **29**, 2765 (1984).

[Léo06] F. Léonforte, A. Tanguy, J. P. Wittmer, and J.-L. Barrat. *Inhomogeneous Elastic Response of Silica Glass.* Physical Review Letters **97**, 055501 (2006).

[Léo11a] F. Léonforte. *Dynamic and elastic heterogeneities in a 2D model glass.* Europhysics Letters **94**, 66002 (2011).

[Léo11b] F. Léonforte. *Vibrational states and disorder in continuously compressed model glasses.* Journal of Non-Crystalline Solids **357**, 552 (2011).

[Mal86] V. K. Malinovsky and A. P. Sokolov. *The nature of boson peak in Raman scattering glasses.* Solid State Communications **57**, 757 (1986).

[Maz09] S. Mazoyer, F. Ebert, G. Maret, and P. Keim. *Dynamics of particles and cages in an experimental 2D glass former.* Europhysics Letters **88**, 66004 (2009).

[Maz11] S. Mazoyer, F. Ebert, G. Maret, and P. Keim. *Correlation between dynamical heterogeneities, structure and potential-energy distribution in a 2D amorphous solid.* European Physical Journal E **34**, 101 (2011).

[Mer66] N. Mermin and H. Wagner. *Absence of ferromagnetism or antiferromagnetism in one- or two-dimensional isotropic heisenberg models.* Phsyical Review Letters **17**, 1133 (1966).

[Mer68] N. D. Mermin. *Crystalline Order in Two Dimensions.* Physical Review Letters **176**, 250 (1968).

[Miy88] H. Miyagawa, Y. Hiwatari, B. Bernu, and J. P. Hansen. *Molecular dynamics study of binary soft-sphere mixtures: jump motions of atoms in the glassy state.* Journal of Chemical Physics **88**, 3879 (1988).

[Mur90] C. A. Murray, W. O. Sprenger, and R. A. Wenk. *Comparison of melting in three and two dimensions: Microscopy of colloidal spheres.* Physical Review B **42**, 688 (1990).

[Nag93] K. Nagayama. *Fabrication of two-dimensional colloidal arrays.* Phase Transitions **45**, 185 (1993).

[O'H03] C. S. O'Hern, L. E. Silbert, A. J. Liu, and S. R. Nagel. *Jamming at zero temperature and zero applied stress: The epitome of disorder.* Physical Review E **68**, 011306 (2003).

[Ono85] G. Y. Onoda. *Direct Observation of Two-Dimensional, Dynamical Clustering and Ordering with Colloids.* Physical Review Letters **55**, 226 (1985).

[Opp72] W. Oppelt. *Kleines Handbuch thechnischer Regelvorgänge.* Verlag Chemie, Weinheim (1972).

[Pea01] K. Pearson. *On lines and planes of closest fit to systems of points in space.* Philosophical Magazine **2**, 559 (1901).

[Per99] D. N. Perera and P. Harrowell. *Stability and structure of a supercooled liquid mixture in two dimensions.* Physical Review E **59**, 5721 (1999).

[Pha02] K. N. Pham, A. M. Puertas, J. Bergenholtz, S. U. Egelhaaf, A. Moussaid, P. N. Pusey, A. B. Schofield, M. E. Cates, M. Fuchs, and W. C. K. Poon. *Multiple Glassy States in a Simple Model System.* Science **296**, 104 (2002).

[Phi81] W. A. Phillips, editor. *Amorphous Solids: Low-Temperature Properties.* Springer, Berlin (1981).

[Pie80] P. Pieranski. *Two-Dimensional Interfacial Colloidal Crystals.* Physical Review Letters **45**, 569 (1980).

[Pol14] D. Polster. *Wechselwirkung zwischen Gitterdefekten in zweidimensionalen kolloiden Systemen.* Ph.D. thesis, University of Konstanz (2014).

[Pra07] V. Prasad, D. Semwogerere, and E. R. Weeks. *Confocal microscopy of colloids.* Journal of Physics: Condensed Matter **19**, no. 11, 113102 (2007).

[Pri87] D. C. Prieve, F. Luo, and F. Lanni. *Brownian Motion of a Hydrosol Particle in a Colloidal Force Field.* Faraday Discussions of the Chemical Society **83**, 297 (1987).

[Pri90a] D. C. Prieve, S. G. Bike, and N. A. Frej. *Brownian Motion of a Single Microscopic Sphere in a Colloidal Force Field.* Faraday Discussions of the Chemical Society **90**, 209 (1990).

[Pri90b] D. C. Prieve and N. A. Frej. *Total Internal Reflection Microscopy: A Quantitative Tool for the Measurement of Colloidal Forces.* Langmuir **6**, 396 (1990).

[Pus86] P. N. Pusey and W. van Megen. *Phase behaviou of concentrated suspensions of nearly hard colloidal spheres.* Nature **320**, 340 (1986).

[Pus87] P. N. Pusey and W. van Megen. *Observation of a Glass Transition in Suspensions of Spherical Colloidal Particles.* Physical Review Letters **59**, 2083 (1987).

[Pus89] P. N. Pusey, W. van Megen, P. Bartlett, B. J. Ackerson, J. G. Rarity, and S. M. Underwood. *Structure of crystals of hard colloidal spheres.* Physical Review Letters **63**, 2753 (1989).

[Ram05] L. Ramos and L. Cipelletti. *Intrinsic Aging and Effective Viscosity in the Slow Dynamics of a Soft Glass with Tunable Elasticity.* Physical Review Letters **94**, 158301 (2005).

[Reh05] T. Rehren and E. B. Pusch. *Late Bronze Age Glass Production at Quantir-Priamesses, Egypt.* Science **17**, 1750 (2005).

[Roy06] C. P. Royall, M. E. Leunissen, A.-P. Hynninen, M. Dijkstra, and A. van Blaaderen. *Re-entrant melting and freezing in a model system of charged colloids.* The Journal of Chemical Physics **124**, 244706 (2006).

[Ruf03] B. Rufflé, M. Foret, E. Courtens, R. Vacher, and G. Monaco. *Observation of the Onset of Strong Scattering on High Frequency Acoustic Phonons in Densified Silica Glass.* Physical Review Letters **90**, 095502 (2003).

[Ruf06] B. Rufflé, G. Guimbretière, E. Courtens, R. Vacher, and G. Monaco. *Glass-Specific Behavior in the Damping of Acousticlike Vibrations.* Physical Review Letters **96**, 045502 (2006).

[Ruf08] B. Rufflé, D. A. Parshin, E. Courtens, and R. Vacher. *Boson peak and its relation to acoustic attenuation in glasses.* Phyiscal Review Letters **100**, 015501 (2008).

[Sas05] M. Sasaki, P. E. Jönsson, H. Takayama, and H. Mamiya. *Aging and memory effects in superparamagnets and superspin glasses.* Physical Review B **71**, 104405 (2005).

[Sch04] P. Scheidler, W. Kob, and K. Binder. *The Relaxation Dynamics of a Supercooled Liquid Confined by Rough Walls.* The Journal of Physical Chemistry B **108**, no. 21, 6673 (2004).

[Sco06] T. Scopigno, J.-B. Suck, R. Angelini, F. Albergamo, and G. Ruocco. *High-frequency dynamics in metallic glasses.* Physical Review Letters **96**, 135501 (2006).

[Shi08] H. Shintani and H. Tanaka. *Universal link between the boson peak and transverse phonons in glass.* Nature Materials **7**, 870 (2008).

[Shl09] J. Shlens. *A Tutorial on Principal Component Analysis.* Tech. rep., Center for Neural Science, New York University (2009).

[Sie43] A. Siegert. *On the fluctuations in signals returned by many independently moving scatterers.* Tech. rep., MIT (1943).

[Sil99] Silvio, Franza, C. Donatibc, G. Parisic, and S. C. Glotzer. *On dynamical correlations in supercooled liquids.* Philosophical Magazine Part B **79**, 1827 (1999).

[Sok95] A. P. Sokolov, U. Buchenau, W. Steffen, B. Frick, and A. Wischnewski. *Comparison of Raman- and neutron-scattering data for glass-forming systems.* Physical Review B: Condensed Matter **14**, 9815 (1995).

[SR91] K. Schmidt-Rohr and H. W. Spiess. *Nature of nonexponential loss of correlation above the glass transition investigated by multidimensional NMR.* Physical Review Letters **66**, 3020 (1991).

[Sti14] T. Still, C. P. Goodrich, K. Chen, P. J. Yunker, S. Schoenholz, A. J. Liu, and A. G. Yodh. *Phonon dispersion and elastic moduli of two-dimensional disordered colloidal packings of soft particles with frictional interactions.* Physical Review E **89**, 012301 (2014).

[Sza11] G. Szamel and E. Flenner. *Emergence of Long-Range Correlations and Rigidity at the Dynamic Glass Transition.* Physical Review Letters **107**, 105505 (2011).

[Tam33] G. Tammann. *Der Glaszustand.* L. Voss, Leipzig (1933).

[Tan12a] P. Tan, N. Xu, A. B. Schofield, and L. Xu. *Understanding the Low-Frequency Quasilocalized Modes in Disordered Colloidal Systems.* Physical Review Letters **108**, 095501 (2012).

[Tan12b] H. Tanaka. *Bond orientational order in liquids: Towards a unified description of water-like anomalies, liquid-liquid transition, glass transition and crystallization.* The European Physical Journal E **35**, 113 (2012).

[Tho84] O. W. Thorpe, S. E. Warren, and J. G. Nandris. *The distribution and provenance of archaeological obsidian in Central and Eastern Europe.* Journal of Archaeological Science **11**, 183 (1984).

[Ver48] E. J. W. Verwey and J. T. G. Overbeek. *Theory of the stability of lyophobic colloids.* Elsevier, Amsterdam (1948).

[vG01] H. H. von Grünberg, L. Helden, P. Leiderer, and C. Bechinger. *Measurement of surface charge densities on Brownian particles using total internal reflection microscopy.* The Journal of Chemical Physics **114**, no. 22, 10094 (2001).

[vG04] H. H. von Grünberg, P. Keim, K. Zahn, and G. Maret. *Elastic Behavior of a Two-Dimensional Crystal Near Melting.* Physical Review Letters **93**, 255703 (2004).

[vM05] W. van Megen, T. C. Mortensen, and G. Bryant. *Change in relaxation scenario at the order-disorder transition of a colloidal fluid of hard spheres seen from the Gaussian limit of the self-intermediate scattering function.* Physical Review E **72**, 031402 (2005).

[Wee00] E. R. Weeks, J. C. Crocker, A. C. Levitt, A. Schofield, and D. A. Weitz. *Three-dimensional direct imaging of structural relaxation near the colloidal glass transition.* Science **287**, 627 (2000).

[Wie30] N. Wiener. *Generalized harmonic analysis.* Acta Mathematica **55**, 117 (1930).

[Wil02] A. Wille, F. Valmont, K. Zahn, and G. Maret. *Shear modulus of two-dimensional colloidal crystals.* Europhysics Letters **57**, no. 2, 219 (2002).

[Wil12] D. Wilms, S. Deutschlander, U. Siems, K. Franzrahe, P. Henseler, P. Keim, N. Schwierz, P. Virnau, K. Binder, G. Maret, and P. Nielaba. *Effects of confinement and external fields on structure and transport in colloidal dispersions in reduced dimensionality.* Journal of Physics: Condensed Matter **24**, 464119 (2012).

[Win75] G. Winterling. *Very-low-frequency Raman scattering in vitreous silica.* Physical Review B **12**, 2432 (1975).

[Wöl13] D. Wöll, C. Kölbl, B. Stempfle, and A. Karrenbauer. *A novel method for automatic single molecule tracking of blinking molecules at low intensities.* Physical Chemistry Chemical Physics (Incorporating Faraday Transactions) **15**, 6196 (2013).

[Wol08] P. G. Wolynes. *Spatiotemporal structures in aging and rejuvenating glasses.* Proceedings of the National Academy of Sciences of the United States of America **106**, 1353 (2008).

[Xia00] Y. Xia, B. Gates, Y. Yin, and Y. Lu. *Monodispersed colloidal spheres: old materials with new applications.* Advanced Materials **12**, 693 (2000).

[Yos10] H. Yoshino and M. Mézard. *Emergence of Rigidity at the Structural Glass Transition: A First-Principles Computation.* Physical Review Letters **105**, 015504 (2010).

[Yos12] H. Yoshino. *Replica theory of the rigidity of structural glasses.* The Journal of Chemical Physics **136**, 214108 (2012).

[Zah97] K. Zahn, J. M. Méndez-Alcaraz, and G. Maret. *Hydrodynamic Interactions May Enhance the Self-diffusion of Colloidal Particles.* Physcal Review Letters **79**, 175 (1997).

Danksagung

Knappe fünf Jahre habe ich an dieser Dissertation gearbeitet, das ist eine ganze Weile! Glücklicherweise war es eine schöne Zeit, und das liegt natürlich zuallererst an all den Leuten, die mich auf dem Weg zum Titel begleitet haben, sowohl privat als auch akademisch. In einigen Fällen hat sich das dann auch vermischt. Danke dafür!

Im Einzelnen sind das

- Dr. Peter Keim, der mir die Möglichkeit gegeben hat, an kolloidalen Gläsern zu forschen und mit seiner praktischen Veranlagung und Erfahrung viel dazu beitrug, das Experiment weiterzuentwickeln und dann am Laufen zu halten. Ebenso weiß ich seine Bemühungen zu schätzen, für eine durchgehend gute Finanzierung zu sorgen. Neben dem vielen Input, den ich von ihm erhalten habe und seiner Begeisterung für meine Experimente und Ergebnisse, die durchaus ansteckend wirkt, ist er auch ein prima Kumpel, um Abends mal der anderen Seite des Lebens zu fröhnen. Dadurch wurden auch die Konferenzen, zu deren Teilnahme er mich ermuntert hat, nicht nur von akademischer Seite aus interessant. Egal ob Rom, Wien, Barcelona, Cargèse oder Bonn. Das extrem gute Verhältnis zu ihm hat sicherlich den größten Anteil an dem erfolgreichen Abschluss meiner Promotion.

- Prof. Dr. Georg Maret, dem ich nicht nur für die Aufnahme an seinem Lehrstuhl danke, sondern auch für die “frühe Weichenstellung”. Im sechsten Semester bekam ich durch ihn die Möglichkeit, im Labor von Hajime Tanaka unter der Anleitung von Paddy Royall erste Gehversuche an dreidimensionalen kolloidalen Gläsern durchzuführen. Seitdem hat mich die Glasphysik gepackt. Seine Expertise auf vielen Spezialgebieten half oft, die eigene Arbeit in neuem Licht zu sehen.

- meine Bürokollegen David, Sven und Herbert, denen ich wichtige Impulse zu verdanken habe. Ohne ihre Sicht der Dinge wäre diese Arbeit um das eine oder andere Kapitel ärmer. Von ihrer Hilfsbereitschaft und Diskussionsfreude habe ich sehr profitiert. Und an der Stelle auch noch ein Sorry für das dauernde “Ich versteh’s nicht!”

- der Rest des Lehrstuhls Maret, der den Forschungsalltag aufgelockert hat. Dazu kommen noch die diversen Lehrstuhlausflüge und Exkursionen in die Konstanzer

Biergärten oder Kneipen. Das alles hat viel Spaß gemacht. Und den einen oder anderen hat man ja auch mal des Nachts auf einer Party getroffen.

- meine Freunde aus Schule und Studium, die mich in meiner Freizeit auf neue Gedanken gebracht haben. Auch wenn sie über ganz Deutschland verteilt und die Treffen (zu) rar sind, wirken moderne Kommunikationsmittel Wunder. Von dieser Seite kam dauernde Unterstützung, die mich über etwaige Tiefs ("Tropfen mal wieder runtergefallen, das wird niemals klappen!") hinweggehoben hat. Interessant außerdem, zu hören, das es außer Physik auch noch etwas anderes gibt!
- meine Familie, die mich ständig aufs Neue motivieren kann und mir den nötigen Rückhalt und Zuspruch gibt. Und bewiesen hat, dass SMS nachts um drei nicht nur vom Experiment verschickt werden - und mich damit ein paar mal an den Rande eines Herzinfarktes gebracht hat, obwohl es sich dann doch nur als ein "Ey komm' mal nach Tü, hier geile Party man! Hot!" oder "Bin im Tanzhaus West, geht voll ab!" herausstellte.
- Anja, welche die Vorzüge eines Physikers erkannt hat. Oder hat sie bemerkt, dass Physiker auch normale Menschen sein können? Zugegeben, Menschen mit vielen Interessen. In meinem Fall jedenfalls.

Radolfzell, im Januar 2015